
FAKULTÄT FÜR
ELEKTROTECHNIK UND
INFORMATIONSTECHNIK

# Prospective motion correction for high resolution gradient recalled echo-based magnetic resonance imaging at ultra-high field

**Dissertation**

zur Erlangung des akademische Grades

**Doktoringenieur**

**(Dr.-Ing.)**

von M.Sc. Hendrik Mattern
geb. am 21.06.1989 in Magdeburg, Deutschland
genehmigt durch die Fakultät für Elektrotechnik und Informationstechnik
der Otto-von-Guericke-Universität Magdeburg

**Gutachter:**

Prof. Dr. rer. nat. Georg Rose (Otto-von-Guericke-Universität Magdeburg)
Prof. Dr. rer. nat. habil. Oliver Speck (Otto-von-Guericke-Universität Magdeburg)
Prof. Dr. rer. nat. Nikolaus Weiskopf (Max-Planck-Institut für Kognitions- und Neurowissenschaften in Leipzig)

Promotionskolloquium am 19.12.2019

## Schriftliche Erklärung

Ich erkläre hiermit, dass ich die vorliegende Arbeit ohne unzulässige Hilfe Dritter und ohne Benutzung anderer als der angegebenen Hilfsmittel angefertigt habe; die aus fremden Quellen direkt oder indirekt übernommenen Gedanken sind als solche kenntlich gemacht.

Insbesondere habe ich nicht die Hilfe einer kommerziellen Promotionsberatung in Anspruch genommen. Dritte haben von mir weder unmittelbar noch mittelbar geldwerte Leistungen für Arbeiten erhalten, die im Zusammenhang mit dem Inhalt der vorgelegten Dissertation stehen.

Die Arbeit wurde bisher weder im Inland noch im Ausland in gleicher oder ähnlicher Form als Dissertation eingereicht und ist als Ganzes auch noch nicht veröffentlicht.

Magdeburg, 21.08.2019

(Signature)

## Abstract

With Magnetic Resonance Imaging (MRI) the human anatomy and vasculature can be depicted non-invasively with superb soft-matter contrast. High resolution MRI could enable delineation of small anatomical structures, however, the resulting smaller voxel sizes reduce the signal-to-noise ratio (SNR). To overcome this, ultra-high field (UHF) MRI ($B_0 \geq 7T$) has been developed because the available SNR scales with the static magnetic field. Besides the boost in SNR, the Gradient Recalled Echo (GRE)-based contrasts Quantitative Susceptibility Mapping (QSM) and Time-of-Flight (ToF) angiography benefit from enhanced contrast mechanisms at UHF. This enabled the non-invasive depiction of small, highly relevant structures for the first time, such as the substantia nigra nigrosome 1 with QSM and lenticulostriate arteries with ToF angiography.

Although, UHF provides higher nominal resolution the effective resolution can be decreased due to subject motion and its induced image artifacts. Even healthy subjects move unintentionally due to breathing and muscle relaxation. For high resolutions, the amplitude of these motions is in the order of the voxel size and the long acquisition times render subject motion more likely. As a result high resolution imaging is limited by the subjects' ability to remain motionless — the so-called biological resolution limit.

In this thesis, Prospective Motion Correction (PMC) was applied to overcome this resolution limit. To that end, two dedicated studies for high resolution, motion-corrected QSM and ToF angiography have been performed at UHF. Furthermore, challenges such as phase singularities and increased Specific Absorption Rate (SAR) constraints have been addressed. Both studies showed qualitatively and quantitatively that inevitable, small-scale motion reduces the reliable detection of small image features and reproducibility of quantitative estimates. With PMC this degradation could be prevented and imaging beyond the biological resolution limit was possible. QSM at 330 µm and ToF angiograpyh at 150 µm isotropic voxel size was acquired, representing some of the highest resolution MRI data published to date. In conclusion, PMC unleashed the full potential of high resolution, GRE-based MRI at UHF.

# Zusammenfassung

Mit der Magnetresonanztomographie (MRT) kann die Anatomie und das Gefäßsystem des Menschen nicht-invasiv mit einem hervorragenden Weichteilkontrast dargestellt werden. Die hochauflösende MRT könnte die Abgrenzung kleiner anatomischer Strukturen ermöglichen, allerdings sinkt das Signal-Rausch-Verhältnis (SNR) für kleine Voxelgrößen. Um das SNR zu erhöhen wird die Ultrahochfeld (UHF) MRT ($B_0 \geq 7T$) verwendet, da sich das verfügbare SNR proportional zum statischen Magnetfeld verhält. Neben höherem SNR profitieren die Gradient Recalled Echo (GRE)-basierte Kontraste Quantitative Susceptibility Mapping (QSM) und Time-of-Flight (ToF) Angiographie von verbesserten Kontrastmechanismen am UHF. Dies ermöglichte erstmals die nicht-invasive Darstellung kleiner, hochrelevanter Strukturen, wie z.B. des Substantia-Nigra-Nigrosoms 1 mit QSM und der lentikulostriäre Arterien mit ToF Angiographie.

Obwohl UHF eine höhere Nominalauflösung bietet, kann die effektive Auflösung durch die Bewegung des Probanden und dadurch hervorgerufene Bildartefakte reduziert werden. Selbst gesunde Probanden bewegen sich aufgrund von Atmung und Muskelentspannung unbeabsichtigt. Bei hohen Auflösungen liegt die Amplitude dieser Bewegungen in der Größenordnung der Voxelgröße. Desweiteren sind Bewegungen des Probanden während der langen Aufnahmezeiten sehr wahrscheinlich. Infolgedessen ist die hochauflösende Bildgebung durch die Fähigkeit der Probanden bewegungslos zu bleiben begrenzt — die so genannte biologische Auflösungsgrenze.

In dieser Arbeit wurde prospektive Bewegungkorrektur (PMC) verwendet um diese Auflösungsgrenze zu überwinden. Zu diesem Zweck wurden zwei UHF-Studien für hochaufgelöste, bewegungskorrigierte QSM und ToF Angiographie durchgeführt. Darüber hinaus wurden Methoden verwendet um Herausforderungen wie Phasensignularitäten und erhöhte spezifische Absorptionsraten (SAR) zu überwinden. Beide Studien zeigten qualitativ und quantitativ, dass unvermeidbare, kleinste Bewegungen die zuverlässige Erkennung kleiner Bilddetails und die Reproduzierbarkeit quantitativer Werte reduzieren. Mit PMC konnte dieses verhindert werden und Bilder über die biologische Auflösungsgrenze hinaus wurden aufgenommen: QSM mit 330 µm und ToF Angiographie mit 150 µm isotroper Voxelgrößen. Dies sind einige der am höchaufgelösten MRT-Daten jemals. Zusammenfassend lässt sich sagen, dass mit PMC das volle Potenzial der hochauflösenden, GRE-basierten UHF-MRT genutzt werden kann.

# Contents

## List of Acronyms

**ACA** anterior cerebral arteries

**ADC** analog-to-digital converter

**AES** Average Edge Strength

**$B_0$** static magnetic field $B_0$

**CAIPIRINHA** Controlled Aliasing in Parallel Imaging Results in Higher Acceleration

**CNR** contrast-to-noise ratio

**CS** Compressed Sensing

**CSF** cerebrospinal fluid

**CT** Computed Tomography

**DOF** degrees of freedom

**DSA** Digital Subtraction Angiography

**FatNavs** fat navigators

**FID** free induction decay

**fMRI** functional Magnetic Resonance Imaging

**FOV** Field of View

**GM** gray matter

**GRAPPA** GeneRalized Autocalibrating Partial Parallel Acquisition

**GRE** Gradient Recalled Echo

**HARPERELLA** HARmonic (background) PhasE REmovaL using the LAplacian operator

**IDEA** Integrated Development Environment for (MR) Applications

**ISMRM** International Society for Magnetic Resonance in Medicine

**KS** Kolmogorov-Smirnov

**LSA** lenticulostriate arteries

**MEDI** morphology-enabled dipole inversion

**MERIT** model error reduction through iterative tuning

**MIP** Maximum Intensity Projection

**MPRAGE** Magnetization-Prepared Rapid Gradient-Echo

**MP2RAGE** Magnetization-Prepared 2 Rapid Acquisition Gradient Echoes

**MPT** Moiré Phase Tracking

**MOTSA** multiple overlapping thin 3D slab acquisition

**MT** magnetization transfer

**MRA** Magnetic Resonance Angiography

**MRI** Magnetic Resonance Imaging

**nMEDI** non-linear, morphology-enabled, dipole inversion

**NMR** Nuclear Magnetic Resonance

**PMC** Prospective Motion Correction

**PROPELLER** Periodically Rotated Overlapping ParallEL Lines with Enhanced Reconstruction

**QSM** Quantitative Susceptibility Mapping

**RF** radio frequency

**ROI** Region of Interest

**SAR** Specific Absorption Rate

**SHARP** Sophisticated Harmonic Artifact Reduction for Phase

**SMV** Spherical Mean Value

**SNR** signal-to-noise ratio

**sSAT** sparse Saturation

**SWI** Susceptibility Weighted Imaging

**$T_1$** longitudinal relaxation

**$T_2$** transversal relaxation

**TA** acquisition time

**TE** echo time

**ToF** Time-of-Flight

**TONE** Tilt-Optimized Nonsaturated Excitation

**TR** repetition time

**UHF** ultra-high field

**UDP** User Datagram Protocol

**VERSE** Variable-Rate Selective Excitation

**VSHARP** Variable-radius Sophisticated Harmonic Artifact Reduction for Phase

**WM** white matter

# List of Figures

# List of Tables

# 1 Introduction

*"It's just an engineering problem."*

— every physicist

Modern medicine and research rely on imaging of the human body. In 2001, a survey among 225 physicians voted Magnetic Resonance Imaging (MRI) together with Computed Tomography (CT) scanning to be the most important innovation of the last 25 years [1]. MRI provides non-invasively information about the human anatomy by utilizing electromagnetic fields for signal generation and encoding.

The spatial resolution of acquired images is one of the main factors determining whether an anatomical structure is depicted or not. Increasing the spatial resolution, thus acquiring images with smaller voxel sizes, can improve depiction of fine anatomical details and therefore improve the outcome of clinical and research studies [2]. However, with decreasing voxel size the available signal-to-noise ratio (SNR) decreases as well. If SNR is too low, the images are impaired by noise, potentially obscuring the depiction of anatomical details. Since SNR in MRI scales with the strength of the static magnetic field $B_0$, MR scanners with stronger magnetic fields have been built over the past decades to enable high resolution MRI [3]. To date, ultra-high field (UHF) MR scanners ($B_0 \geq 7$T) achieve voxel sizes beyond 1×1×1 mm in neuroimaging [3, 4].

Two promising applications for neuroimaging with UHF MRI are Time-of-Flight (ToF) angiography and Quantitative Susceptibility Mapping (QSM). Besides increased SNR, ultra-high magnetic field strengths improve the contrast of QSM and ToF angiography, rendering them as prime candidates for UHF MRI [2, 3, 5]. For signal generation and encoding, both utilize a Gradient Recalled Echo (GRE) sequence. While ToF imaging is used to depict the arterial vasculature, QSM is sensitive to the venous vasculature and allows to map local changes in tissue susceptibility. Recent literature has shown the potential of high resolution for both contrasts: With 7T MRI, high resolution ToF angiography imaged reliably small perforating arteries such as the lenticulostriate arteries (LSA) for the first time [6, 7] and QSM identified substructures of brain regions usually only depicted with ex-vivo histology and not visible in other MRI contrasts [8]. Both applications could have significant impact for diagnosis since changes in microvasculature as well as local susceptibilities are linked to diseases such as multiple sclerosis, Alzheimer's, and Parkinson's disease [9, 10].

This potential of high resolution MRI is limited by subject motion due to two reasons. First, subject motion during scanning causes misalignment of the imaged object to the imaging volume. Hence, the image encoding is corrupted and artifacts such as blurring or ghosting appear. With increasing resolution, MRI is more sensitive to subject motion because the ratio

of motion amplitude to voxel size increases, rendering misalignments more likely. Thus, even involuntary, physiological motion such as muscle relaxations or breathing can induce motion artifacts [11, 12]. Second, very high resolution MRI requires between several tens of minutes and several hours of scanning despite the increased SNR and contrast-to-noise ratio (CNR) at UHF. During this time any subject motion can introduce image artifacts which can conceal anatomical details. Thus, small-scale motion can decrease the level of detail in high resolution MRI, presenting a so-called *biological resolution limit* [12].

Prospective Motion Correction (PMC) can overcome this biological resolution limit. By tracking the subject and using this data to update the image volume's position and orientation accordingly, PMC prevents any misalignments during acquisition. Thus, images free of motion-induced artifacts can be reconstructed.

Recent studies have shown the potential of PMC for high resolution MRI [12–14], but no comprehensive investigation of using PMC to acquire ToF and QSM beyond the biological resolution limit have been presented. In this thesis the potentials and challenges of combining GRE at ultra-high field with motion correction to achieve high resolution ToF angiography and QSM free of motion artifacts are investigated. To that end, PMC was implemented and evaluated for ToF angiography and QSM respectively, resulting in the acquisition of some of the highest resolution human in vivo data to date.

Before focusing on the performed experiments, the background of all applied techniques is given in chapter 2. First, the Nuclear Magnetic Resonance (NMR) signal and MRI principles as well as advantages and challenges of UHF are shortly explained. Subsequently, the GRE sequence and its derived contrasts, i.e. QSM and ToF angiography, are introduced. The principles and implementation of PMC conclude the background section. Chapters 3 and 4 focus on the performed and published studies for motion-corrected QSM and ToF angiography, respectively. In the last chapter, the outcome of both studies is discussed jointly and future objectives are identified.

# 2 Background

> *"Magnetic resonance is based upon the interaction between an applied magnetic field and a nucleus that possesses spin."*
>
> — Brown et al. *MRI: Basic principles and applications [15], p.1*

This chapter introduces the theoretical concepts used in this thesis, beginning with the basics of the Nuclear Magnetic Resonance (NMR) signal. Then, the echo generation and spatial encoding in MRI are explained using the GRE sequence as an example. For a more comprehensive explanation of the NMR signal and MRI sequences in general the reader is referred to [15–18]. Subsequently, the GRE-derived contrasts Quantitative Susceptibility Mapping (QSM) and Time-of-Flight (ToF) angiography are introduced, followed by a brief review of potentials and challenges of UHF MRI. The chapter concludes with an overview of Prospective Motion Correction (PMC) and a short summary of the introduced techniques.

## 2.1 The Nuclear Magnetic Resonance signal

The nucleus of any atom consists of neutrons and protons. These elementary particles have an intrinsic property the so-called nuclear spin angular momentum, or short *spin*. If a nucleus has an uneven number of particles, it possesses a non-zero spin. Although for most elements at least one isotope with non-zero spin exists, hydrogen is most commonly used in MRI due to is high abundance in the human body. In the following the NMR phenomena will be introduced with respect to hydrogen, or more precise, its nucleus — a single proton. Nevertheless, the introduced concepts are valid for any nuclei with non-zero spin.

The proton spin can be thought of as a rotation of the nucleus about its own axis. Since the proton is positively charged and rotating, it can be imagined as a circulating electric current with an associated magnetic moment [17]. Due to this magnetic moment, induced by the spin of the nucleus, the proton has its own magnetic field and, thus, can interact with external electro-magnetic fields. Spin $\mathbf{I}$ and magnetic moment $\mu$ are related by an element-specific proportionality constant $\gamma$:

$$\mu = \gamma \mathbf{I} \tag{2.1}$$

This constant $\gamma$ is the so-called *gyromagnetic ratio* and for the proton it is $\gamma = 2\pi \times 42.58$ MHz/T

If the proton is placed in an external magnetic field it will tend to align to this field, analogous to a compass needle [17]. However, due to its moment it experiences a torque causing the proton to precess, similar to a gyroscope in the gravitational field. The precession frequency is given by:

$$\omega_0 = \gamma B_0 \tag{2.2}$$

with $\omega$ as the so-called *Larmor* frequency and $B_0$ the external magnetic field.

Note that quantum mechanically protons align to an external magnetic field in two quantized states: parallel (spin-up) or anti-parallel (spin-down). The ratio of spin-up to spin-down for a large number of protons is described by a Boltzmann distribution. As the spin-down state requires less energy, more spins align parallel to the field. From a macroscopic perspective, this uneven distribution of spins can be summarized into a single effective magnetization vector aligned parallel to the magnetic field, the so-called *net magnetization*. Abstracting a large ensemble of spins as a single magnetization allows to describe NMR with classical mechanics. A quantum mechanical explanation of the NMR phenomena is provided in [19].

The net magnetization $M_0$ is proportional to the external magnetic field $B_0$. Their dependency can be approximated with [15, 20]:

$$M_0 \approx \chi \frac{B_0}{\mu_0} \tag{2.3}$$

with $\mu_0$ as the magnetic permeability in free space. The proportional constant $\chi$ is the so-called *magnetic susceptibility*. In short, susceptibility is a tissue-specific material property and describes the degree of magnetization a material generates when places in an external magnetic field [21]. The susceptibility value can be positive or negative. For materials with positive $\chi$ values, the magnetization aligns with the field, also called *paramagnetism*. *Diamagnetic* materials have negative $\chi$ values and the magnetization opposes with the field [20]. Note that this property does not describe the response of a individual spin, but rather the average field generated by many spins [21].

In brief, by placing tissue within an external magnetic field $B_0$, the tissue's protons will start to precess around $B_0$ and align themselves parallel or anti-parallel to the $B_0$field. As more spin are aligned parallel to $B_0$, this imbalance generates, from a macroscopic perspective, an effective net magnetization $M_0$ along the external field (conventionally aligned along the z-axis). This is the so-called *equilibrium*, in which the magnetization $M_0 = M_z$, thus, the magnetization is purely *longitudinal*. By flipping the magnetization into the x-y-plane *transversal magnetization* $M_{xy}$ is generated. This transversal magnetization will precess around $B_0$ inducing a current in coils placed near the excited tissue. To excite the magnetization RF-pulses (with a frequency of $w_0$) are applied. In a *rotating frame of reference*, which rotates at $w_0$ parallel to $B_0$, a RF-pulse is equivalent to a stationary $\mathbf{B_1}$ field and the magnetization is rotated around $\mathbf{B_1}$ by an angle $\alpha$:

$$\alpha = \gamma |\mathbf{B_1}| \tau \tag{2.4}$$

with $|\mathbf{B_1}|$ as the amplitude of applied field and $\tau$ the pulse duration. At equilibrium, a *flip angle* of 90° rotates the magnetization into the transversal plane, while a flip angle of 180° inverts the magnetization. After excitation, the magnetization recovers back to equilibrium. This process is called *relaxation* and can be separated into longitudinal relaxation ($T_1$) and transversal relaxation ($T_2$).

Immediately after a 90°-pulse, all spins precess coherently at the Larmor frequency in the

x-y-plane. Due to spin-spin interactions field fluctuation occur. Imagining two protons moving close to each other, their magnetic moments will superimpose with each other and the external field, creating temporally a change in the effective field. This causes the protons to spin at a different resonance frequency of a short instance of time and, after returning to Larmor frequency, a phase offset is accumulated. On a macroscopic scale, these spin-spin interactions cause the magnetization to dephase. Thus, after the excitation the transversal magnetization is maximal and decays over time until all proton precess incoherently and no transversal magnetization is detectable. This is the so-called *free induction decay (FID)* and, within a rotating frame of reference, can be described over time as:

$$M_{xy}(t) = M_{xy}(0)e^{-t/\mathrm{T}_2} \tag{2.5}$$

with the transversal relaxation time $\mathrm{T}_2$. This tissue-specific time constant characterizes the time unit the transverse magnetization decays to $M_{xy}(\mathrm{T}_2) = 0.37M_0$.

Besides field fluctuation caused by spin-spin interaction, magnetic field inhomogeneities originating from hardware imperfections and susceptibility-induced field distortions cause dephasing. Therefore, the magnetization is effectively decaying faster at:

$$\frac{1}{\mathrm{T}_2^*} = \frac{1}{\mathrm{T}_2} + \frac{1}{\mathrm{T}_2'} \tag{2.6}$$

with $\mathrm{T}_2'$ as the field inhomogeneity-induced decay in transversal magnetization.

Spin-spin interaction causes dephasing, thus reduce the transverse magnetization. By exchanging thermal energy with the lattice protons recover back into their thermal equilibrium, thus the spins align along $B_0$ and, eventually, the longitudinal magnetization recovers back to $M_0$:

$$M_z(t) = M_z(0)e^{-t/\mathrm{T}_1} + M_0(1 - e^{-t/\mathrm{T}_1}) \tag{2.7}$$

with the longitudinal relaxation time $\mathrm{T}_1$. This tissue-specific time constant characterizes the time unit the longitudinal magnetization recovers to $M_z(\mathrm{T}_1) = 0.63M_0$ (given $M_z(0) = 0$). For biological tissues, longitudinal relaxation times are considerably longer than transversal relaxation times [18]. Hence, the detectable transversal magnetization is decayed before the longitudinal magnetization recovered back to equilibrium. Illustratively, the temporal evolution of $\mathrm{T}_1$, $\mathrm{T}_2$, and $\mathrm{T}_2^*$ relaxation are plotted in Fig. 2.1.

## 2.2 GRE-based Magnetic Resonance Imaging (MRI)

If tissue is placed in an external magnetic field and excited by a RF-pulse the resulting FID can be detected by coils placed near the excited tissue, but no signal localization or manipulation is possible. In this section echo formulation and spatial encoding are introduced. Although echoes and encoding are explained using the GRE sequence, the concepts are valid for MRI in general and can be adapted to any other imaging sequences. Subsequently, GRE-derived

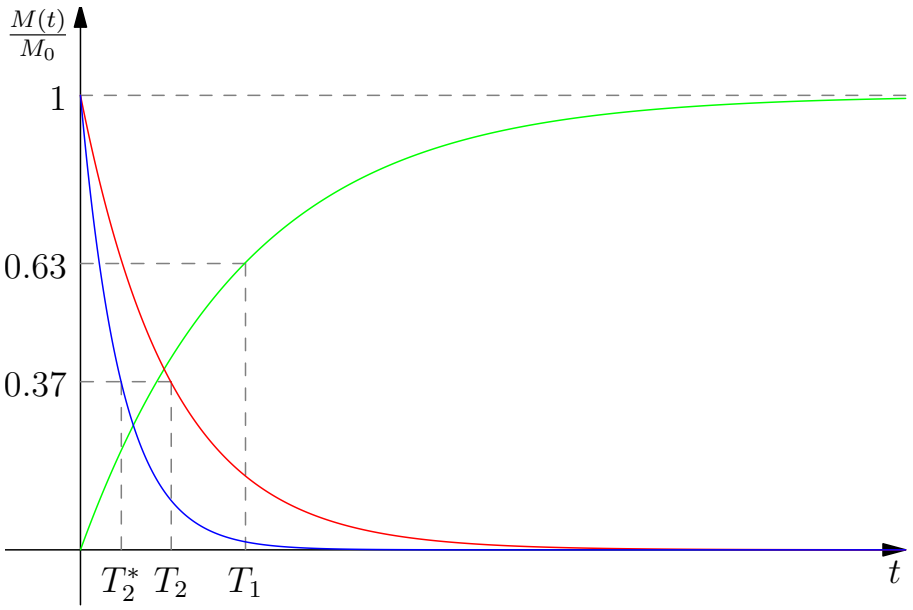


Figure 2.1: Exemplary $T_1$, $T_2$, and $T_2^*$ relaxation processes. Note that $M(t)$ reflects the longitudinal magnetization $M_z(t)$ for $T_1$ and transversal magnetization $M_{xy}(t)$ for $T_2$ and $T_2^*$ relaxation

contrast — QSM and ToF angiography — are introduced.

### 2.2.1 Spatial encoding and echo generation

To spatially encode spin ensembles and generate echoes of the FID, additional magnetic fields are required. These spatially linearly varying fields are called *gradient fields* and are created by three dedicated coils in x, y, and z direction. Gradient fields superimpose with the static magnetic field and cause the effective field to be spatially varying, hence, the precession frequency becomes spatially encoded:

$$\omega(x,y,z) = \gamma(B_0 + \frac{\partial B_0}{\partial x}x + \frac{\partial B_0}{\partial y}y + \frac{\partial B_0}{\partial z}z) = \gamma(B_0 + G_x x + G_y y + G_z z) \tag{2.8}$$

Thus, in MRI data is encoded and sampled in the frequency domain, the so-called *k-space*. Within the k-space data is organized as follows [18]:

$$k = \frac{\gamma}{2\pi}\int G(t)dt \tag{2.9}$$

with $G(t)$ as the applied gradient.

Although the concept of k-space and gradients allows to encode the signal location into the signal, a single measurement would detect the superimposed sum of all excited spins, each with a phase increment depending on its location in $x$, $y$, and $z$:

$$\phi(x,y,z) = k_x x + k_y y + k_z z \tag{2.10}$$

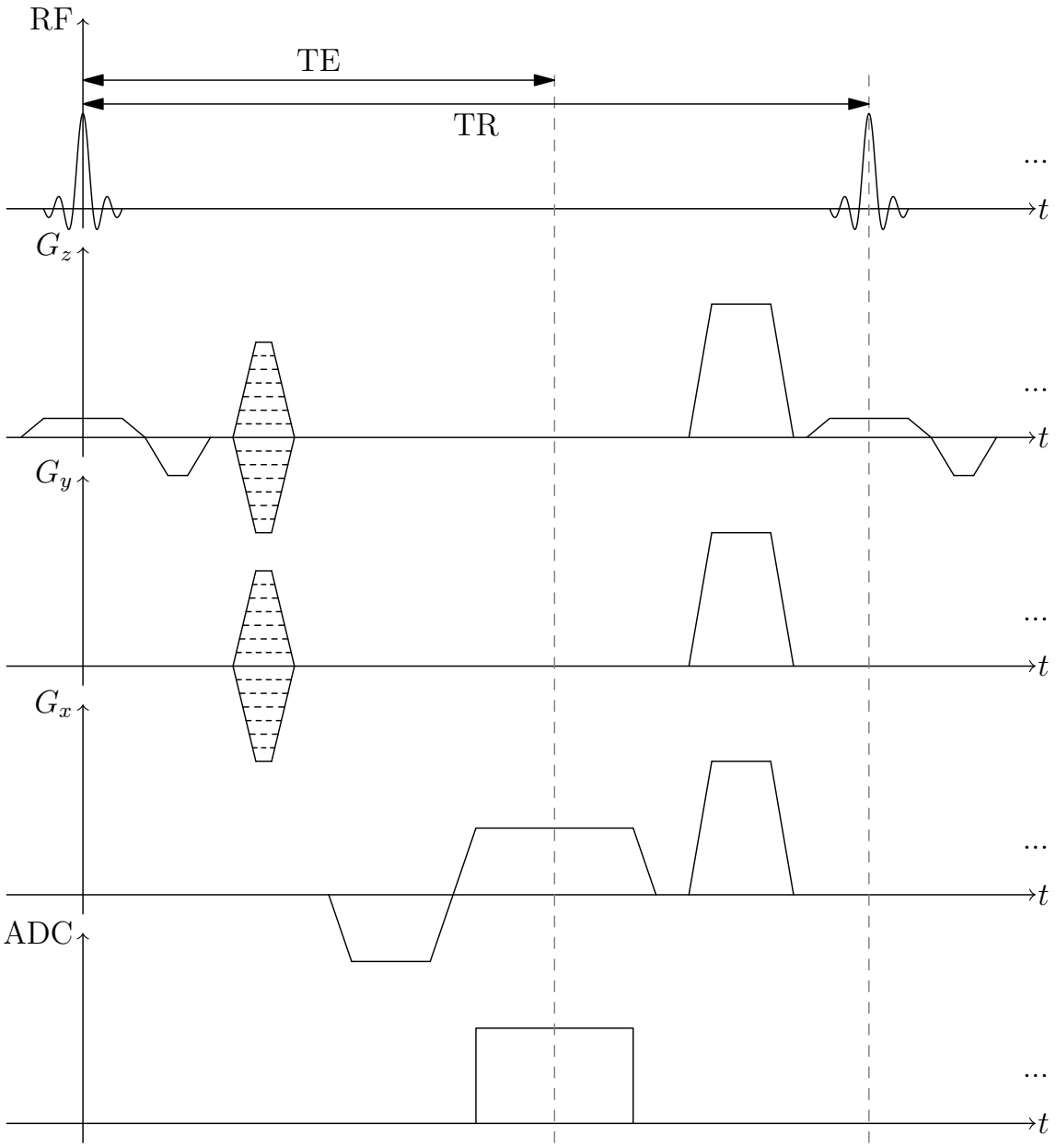


Figure 2.2: Sequence diagram for a slab-selective, 3D encoded, GRE sequence with spoiling. TR and TE are indicated by arrows.
Gradient Recalled Echo (GRE); echo time (TE); echo time (TE).

By repeating the measurement with a varying gradient encoding the entire k-space can be filled (see next sections). For an object **I** the detected signal **S** is given by its Fourier transform [18]:

$$\mathbf{S}(k_x, k_y, k_z) = \iiint \mathbf{I}(x, y, z) e^{i2\pi(xk_x + yk_y + zk_z)} dx\, dy\, dz \tag{2.11}$$

Hence, by applying the inverse Fourier transform to the measured k-space the image can be recovered [18]:

$$\mathbf{I}(x, y, z) = \iiint \mathbf{S}(k_x, k_y, k_z) e^{-i2\pi(xk_x + yk_y + zk_z)} dk_x\, dk_y\, dk_z \tag{2.12}$$

The reconstructed image is complex, ergo, has a real and imaginary part. Commonly, the absolute of the complex values is used to compute magnitude images while the angle provides the phase information of the object. Within k-space, the center stores low spatial frequencies, thus, contains information about the contrast. The k-space periphery corresponds to edge information and small structures. Furthermore, the maximum gradient encoding strength $k_{max}$ determines the voxel size:

$$\Delta x = \frac{1}{2k_{max}} = \frac{\mathrm{FOV}_x}{N_x} \tag{2.13}$$

with $\Delta x$ being the voxel size, $\mathrm{FOV}_x$ the Field of View, and $N_x$ the number of encoding steps in x-direction (equation can be applied in y- and z-direction equivalently). Therefore, higher resolutions require stronger gradient encoding strengths and more encoding steps, hence, longer acquisition times.

So far a single coil is assumed for signal detection. In practice, coil arrays with several elements are used to improve SNR and enable imaging acceleration. The introduced single coil reconstruction can be extended to multi-coil setups by performing inverse Fourier transforms for each coil individually and combining the images using for example the root sum-of-squares method.

The acquisition of k-space is implemented by sequentially switching gradients and RF-pulses, the so-called *sequence*. In Fig. 2.2 the switching for a 3D GRE sequence is shown. Note that gradient fields cannot be turned on and off instantaneously, but require a certain time to ramp up and down. In the following spatial encoding and echo formulation are explained with the shown GRE sequence as an example.

### Selection excitation

To excite selectively a certain volume a gradient is applied to change the local resonance frequency along one direction, commonly the z-axis. By tuning the frequency of a RF-pulse to the local resonance frequency of the volume of interest, only protons within this volume will be excited. The selective excitation is the first encoding step in the sequence shown in Fig. 2.2.

Besides the change in resonance frequency the gradient also dephases the magnetization. To compensate for this a *rewinder* gradient is turned on immediately after the excitation.

The gradient moment of the rewinder is half of the gradient moment of the volume selection gradient and has an inverted polarity.

### Phase encoding

After the selective excitation, the transversal magnetization is *phase encoded*. By switching on a gradient the resonance frequency varies spatially. Depending on its position, protons will precess faster or slower. After switching of the gradient all protons will return to the global resonance frequency, but a position-dependent phase offset remains. For the shown 3D GRE sequence in Fig. 2.2 phase encoding is performed in y- and z-direction. As indicated by the dotted lines, this phase encoding process is repeated with different gradient strengths to fill the entire k-space. Consequently, the acquisition time (TA) for a 3D-encoded sequences is:

$$\mathrm{TA} = N_y N_z \mathrm{TR} \tag{2.14}$$

with the repetition time (TR) being the time between two consecutive excitations and $N_{y/z}$ the required number of phase encoding steps.

### Frequency encoding

After two of three directions are phase encoded, the remaining x-direction is *frequency encoded*. Simultaneously, the signal is measured as indicated by the analog-to-digital converter (ADC) block in Fig. 2.2. This event is the so-called *read-out*. During the read-out, a gradient is switch on to spatially encode the resonance frequency of the spins while acquiring the signal to fill a single line in k-space. Alternatively, frequency encoding can be seen as acquiring a projection of the object perpendicular to the gradient direction. Perpendicular to the x-axis the field strength is identical, thus all spins precess with the same frequency and will superimpose in the measured signal. By changing the phase encoding the accumulated phase of the spins prior to the read-out differs and, therefore, the spins will be wrapped differently in the projection. Hence, this type of imaging is also called *spin warp*.

### The gradient echo

Prior to the read-out, a prewinder gradient is applied which causes dephasing of the magnetization. The prewinder gradient moment is half the read-out gradient moment with inverted polarity. The subsequent read-out gradient will revert this dephasing and create a so-called *gradient echo* by rephasing all spins at the echo time (TE). At the echo time, the following condition is valid:

$$\int G(t)dt = 0 \tag{2.15}$$

Although at TE all spins have coherent phase, the transversal magnetization has decayed with $\mathrm{T}_2^*$ since its excitation:

$$M_{xy}(\mathrm{TE}) = M_{xy}(0)e^{-\mathrm{TE}/\mathrm{T}_2^*} \tag{2.16}$$

By applying an additional 180°-pulse before the read-out signal decay due to hardware imperfection can be rephased to create a so-called *spin echo* with pure $T_2$ decay, but applying these additional pulses can be non-trivial. Spin echo sequences were not used in this thesis and the interested reader is referred to [15–18] further details on spin echo imaging.

#### Spoiling

As shown in Fig. 2.2, after the read-out and prior to the next excitation strong gradients in all three directions are applied. These gradients dephase the remaining transversal magnetization and are therefore called *spoilers*. Alternatively, the transversal magnetization could be fully rephased to re-use it in consecutive excitations and, eventually, increasing the available SNR as done in the so-called balanced steady state free precession sequence [22]. However, these balanced sequences suffer from banding artifacts due to off-resonance effects. These artifacts are reduced by spoilers at the cost of lower SNR compared to the balanced scenario [22]. To further reduce the potential impact of residual transverse magnetization, the phase of the RF-pulses it altered for each excitation. If the combination of RF and gradient spoiling is used in a gradient echo sequence it is also called GRE sequence.

#### Steady state signal

In a GRE sequences with short TR and low flip angle $\alpha$ the detected signal $S(TE)$ reaches a steady state after multiple RF excitations [16, 17]:

$$S(\mathrm{TE}) = M_0 \sin\alpha \, \frac{1 - e^{-\mathrm{TR}/\mathrm{T_1}}}{1 - \cos\alpha \; e^{-\mathrm{TR}/\mathrm{T_1}}} e^{-\mathrm{TE}/\mathrm{T_2^*}} \tag{2.17}$$

The signal is a function of tissue parameters ($T_1$, $T_2^*$), sequence parameters ($\alpha$, TR, TE), and the magnetization in equilibrium $M_0$. The flip angle $\alpha_E$ which maximizes the signal is the so-called *Ernst angle* [16, 17]:

$$\alpha_E = \arccos(e^{-\mathrm{TR}/\mathrm{T_1}}) \tag{2.18}$$

Depending on the sequence parameters used, GRE can be sensitive to a large variety of tissue properties such as longitudinal relaxation times and spin density. In this thesis the GRE-based contrast QSM and ToF angiography are used and explained in the following sections.

### 2.2.2 Quantitative Susceptibility Mapping (QSM)

Quantitative Susceptibility Mapping (QSM) is a post-processing technique for GRE-based data. In contrast to most GRE-based image contrasts, QSM utilizes the phase information to compute the bulk tissue susceptibility per voxel. Susceptibility of biological tissue ranges from paramagnetic (due to the properties of most transition metals and metalloids) to diamagnetic (due to inorganic compounds and myelin lipids). Furthermore, venous blood is paramagnetic due to the iron in deoxyhemoglobin. Following Eq. 2.3, the magnetization depends on the local

magnetic susceptibility, hence, QSM can be used as a proxy for myelin and iron or can be used for venography [20].

In the following, the basic concepts of the contrast origin (forward model) and required QSM processing steps (backward model) are explained. For a detailed mathematical description the interested reader is referred to [21, 23–25].

### From susceptibility to phase

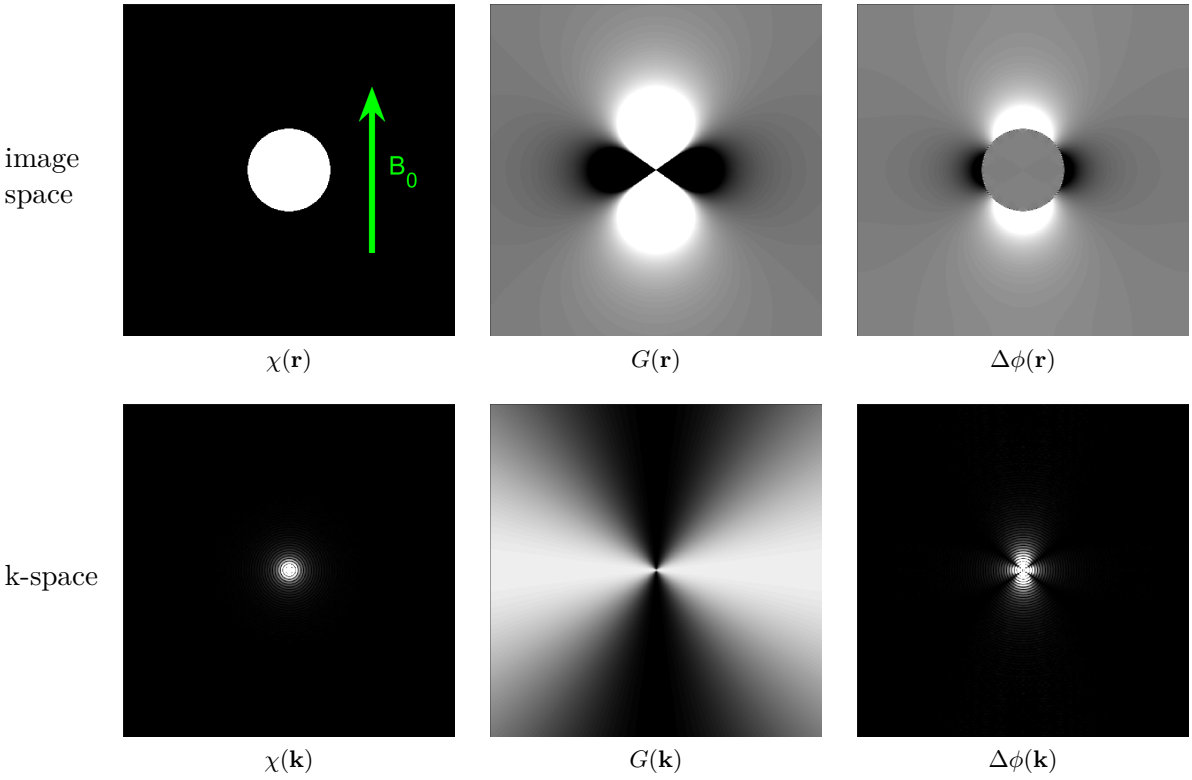


Figure 2.3: A homogeneous, spherical susceptibility distribution $\chi(\mathbf{r})$ is placed in $B_0$. In image space, the dipole kernel $G(\mathbf{r})$ is convoluted with $\chi(\mathbf{r})$ resulting in the spatially varying phase changes $\Delta\phi(\mathbf{r})$. The equivalent phase in k-space $\Delta\phi(\mathbf{k})$ is computed by voxel-wise multiplication of the dipole kernel $G(\mathbf{k})$ and the susceptibility $\chi(\mathbf{k})$.

The difference in bulk susceptibility between different tissues induces local field changes, hence, cause locally varying resonance frequencies. This susceptibility induced dephasing $\Delta\phi$ for a certain TE at the given object location $\mathbf{r}$ is [21, 23]:

$$\Delta\phi(\mathbf{r}, \mathrm{TE}) = \phi_0(\mathbf{r}) + \gamma \Delta B_z(\mathbf{r}) \mathrm{TE} \quad \text{for } B_0 || z \tag{2.19}$$

with $\phi_0(\mathbf{r})$ as the coil sensitivity-dependent phase offset and $\Delta B_z(\mathbf{r})$ as the local field variation. This field variation is related to the source magnetization $M_z(\mathbf{r})$ convoluted with the Green's

function (also called point-dipole response or dipole kernel) [21, 23]:

$$\Delta B_z(\mathbf{r}) = \mu_0 M_z(\mathbf{r}) * G(\mathbf{r}) \tag{2.20}$$

with $\mu_0$ as the magnetic permeability of free space. Green's function $G(\mathbf{r})$ is defined as [21, 23]:

$$G(\mathbf{r}) = \frac{1}{4\pi}\frac{3\cos^2\theta}{|\mathbf{r}|^3} \tag{2.21}$$

with $\theta$ as the angle between the z-direction and $\mathbf{r}$. In k-space with the corresponding coordinate vector $\mathbf{k}$ the dipole kernel is defined as [23]:

$$G(\mathbf{k}) \begin{cases} \frac{1}{3} - \frac{k_z^2}{|\mathbf{k}|^2}, & \text{for } \mathbf{k} \neq 0 \\ 0, & \text{for } \mathbf{k} = 0 \end{cases} \tag{2.22}$$

Under the condition $\chi \ll 1$, the magnetic field variation induced by the susceptibility source distribution $\chi(\mathbf{r})$ can be written as $\mu_0 M_z(\mathbf{r}) \approx B_0 \chi(\mathbf{r})$ (compare Eq. 2.3). Therefore, the change in local field variation depends on the susceptibility distribution and dipole kernel. This dependency is expressed in the forward model [23]:

$$\Delta B_z(\mathbf{r}) = B_0 \mathcal{F}^{-1}\{\chi(\mathbf{k})G(\mathbf{k})\} \tag{2.23}$$

with $\mathcal{F}^{-1}$ as the inverse Fourier transform of the voxel-wise multiplication of the dipole kernel and tissue susceptibility in k-space.

By substituting $\Delta B_z$ with Eq. 2.23 in Eq. 2.19 the phase change $\Delta\phi$ can be summarized in a single equation:

$$\Delta\phi(\mathbf{r}, \mathrm{TE}) = \phi_0(\mathbf{r}) + \gamma B_0 \mathrm{TE} \mathcal{F}^{-1}\{\chi(\mathbf{k})G(\mathbf{k})\} \tag{2.24}$$

Eq. 2.24 is illustrated in Fig. 2.3 for a spherical susceptibility distribution. The discontinuities in the induced phase changes are located on a cone with the *magic angle* of approximately 54.7° (see Green's function $G$ in Eq. 2.21 and Eq. 2.22).

MRI can only estimate $\Delta\phi$. Therefore, computing the underlying susceptibility distribution requires to isolate the susceptibility induced phase change from the background field $\phi_0(\mathbf{r})$ and invert the forward model, also called *backwards model* or *dipole inversion*. Solving this backwards model is non-trivial and will be explained along with the other required QSM processing steps in the next section.

### From phase to QSM

In the first step, the raw GRE phase images are *unwrapped*. This unwrapping is necessary because phase values are stored within a $2\pi$ range and if the measured phase exceeds this range, aliasing in form of $2\pi$ jumps will appear [21, 23]. The true phase is estimated by locally adding multiples of $2\pi$ to compensate for these wraps [21]. This phase information is

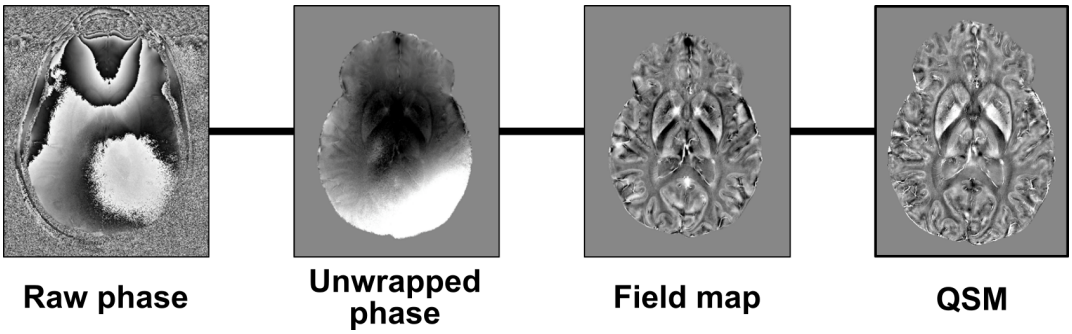


Figure 2.4: Generic QSM pipeline: Raw phase images are unwrapped and field maps are generated by removing background field contribution. In the last step, susceptibility maps are computed by dipole inversion
Quantitative Susceptibility Mapping (QSM).

a superposition of the background field and local magnetic field perturbations due to tissue susceptibility (see Eq. 2.23). By removing the background phase from the unwrapped phase, field changes from outside the ROI are eliminated [26] and a so-called *field map* is generated. Commonly, background field filtering is performed by utilizing Laplacian equations [27, 28]. In the last step, the forward model (see Eq. 2.23) is inverted to reconstruct the local susceptibility distribution. As seen from Eq. 2.22 there are points of discontinuity and, therefore, the system is ill-posed [21] requiring either multiple GRE measurements with different orientations of the object with respect to $B_0$ [29] or the use of regularization [30] to prevent artifacts in the QSM reconstruction [21]. An generic QSM pipeline is given in Fig. 2.4. Each processing steps is an active field of research. For example, background field removal is reviewed in [26] and dipole inversion algorithms are compared to each other in [31]. For an introduction into the algorithms used in this thesis, the interested reader is referred to A.3. Background field removal is based on the Spherical Mean Value (SMV) property (see A.3.1) and achieved with Sophisticated Harmonic Artifact Reduction for Phase (SHARP) and HARmonic (background) PhasE REmovaL using the LAplacian operator (HARPERELLA). For dipole inversion non-linear, morphology-enabled, dipole inversion (nMEDI) is used (see A.3.2).

In general, susceptibility is anisotropic and can be described as a tensor [32, 33], but tensor computation requires additional data acquired with different orientations. Therefore, it is commonly neglected and isotropic susceptibility is assumed.

### 2.2.3 Time-of-Flight (ToF) angiography

Time-of-Flight (ToF) angiography [34] is based on a modified GRE sequence and is applied routinely at clinical field strengths to detect arterial pathologies, such as intracranial stenosis [35, 36] or unruptured aneurysms [37–39]. Although, ToF angiography allows to detect non-invasively small vessel pathologies such as dural arteriovenous fistulas, arteriovenous malformations, and arterial feeders of intracranial tumors, Digital Subtraction Angiography (DSA) remains the gold standard in clinical routine due to its superior spatial resolution and image

quality [40–43]. Compared to ToF angiography, DSA has considerable drawbacks: radiation exposure for staff and patients, use of iodinated contrast agent, and artery puncture for catheter placement, resulting in a low but significant risks of neurological complications or idiosyncratic reactions [37, 44–46]. By increasing spatial resolution, ToF angiography could become a valuable alternative to DSA.

The following sections briefly introduce the ToF contrast mechanism and address the modifications required to derive a ToF sequence from a plain GRE sequence. More comprehensive review of ToF angiography is given in [16, 17, 47].

### In-flow enhancement

The steady state signal in ToF angiography follows the GRE signal Eq. 2.17. As indicated by Eq. 2.18, the Ernst angle $\alpha_E$ maximizes the steady state signal. Thus, if a flip angle $\alpha > \alpha_E$ is applied, the steady state signal of the static tissue is saturated. Blood flowing into the imaging volume however is fully relaxed creating hyperintense arteries. This effect the the so-called *in-flow enhancement*. For a blood vessel oriented perpendicular to an axial imaging volume full in-flow replacement is achieved if the blood velocity $v$ is [16, 17]:

$$v \geq \frac{N_z \Delta z}{\mathrm{TR}} \tag{2.25}$$

with slab thickness $N_z \Delta z$ defined as the product of encoding steps and the slice thickness. If incomplete in-flow replacement is achieved, e.g. due to oblique vessel orientation with respect to the imaging slab, the blood signal will decay with each applied excitation, reducing the vessel-to-background ratio. In conclusion, ToF vessel-to-background ratio depends on the in-flow enhancement which decreases with:

- decreasing blood velocity,
- increasing number of excitations applied to blood within the imaging slab due to vessel path through slab, TR, and slab thickness,
- decreasing flip angle,
- decreasing $\mathrm{T}_1$ relaxation of the static tissue.

Blood velocity decreases with decreases with vessel size [47]. Hence, vessel-to-background ratio should be optimized with respect to a target vessel size. In the following section, techniques to increase the CNR of arteries by adapting the ToF acquisition will be introduced.

### Contrast optimization

Following Eq. 2.25, the in-flow enhancement scales reciprocally with the imaging volume thickness. Therefore, distal vessels in whole brain 3D ToF acquisitions are prone to low vessel-background-ratios despite the SNR advantage 3D encoding provides [47]. Acquiring multiple 2D slices would overcome this problem, however the potential of image acceleration techniques, arbitrary small slice thickness, and available SNR are limited [47]. By using MOTSA [48, 49]

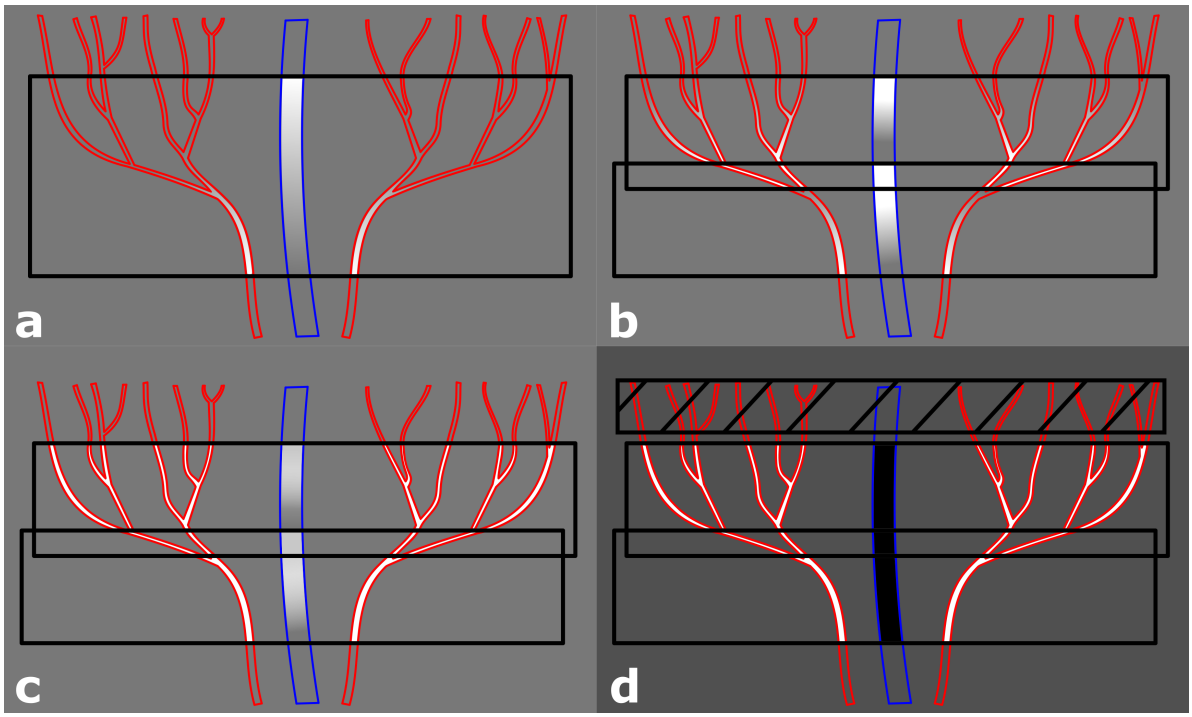


Figure 2.5: ToF contrast optimization: Arteries and veins are outlined in red and blue, respectively. The vessels' signal within the imaging volume(s) (indicated by black rectangles) is brightness encoded while the signal of the static background tissue is represented in solid gray. (a) As the arterial (venous) blood flows upwards (downwards) through the 3D imaging slab, its signal is saturated until the in-flow enhancement is fully suppressed and vessel-to-background ratios converge to zero. (b) To improve vessel enhancement, multiple overlapping thin 3D slab acquisition (MOTSA) is used. Although MOTSA enables to track more distal vessels, the vessel signal will decrease as a function of experienced RF pulses, ergo, the vessels' signal decays along its flow direction. (c) By increasing the flip angle along the primary, arterial flow direction (i.e. upwards flow) with TONE, homogeneous vessel intensity profiles are achieved. (d) To suppress the static background tissue additional magnetization transfer (MT) pulses are used. Furthermore, the venous signal is suppressed by placing an additional saturation slab above the imaging volume (indicated by striped rectangle).
magnetization transfer (MT), Time-of-Flight (ToF), Tilt-Optimized Nonsaturated Excitation (TONE)

the advantages of 2D and 3D can be combined to improve vessel-to-background ratios while maintaining high SNR [47] (see Fig.2.5 (a) and (b)).

With MOTSA, full inflow replacement is commonly not achieved and blood flowing through the imaging slab gets saturated the further distally it flows. Therefore, the vessel-to-background ratio will decrease in distal slices compared to slices with fully relaxed blood. To improve contrast a Tilt-Optimized Nonsaturated Excitation (TONE) pulse is used instead of a uniform RF-excitation [50]. These ramped pulses have a spatially varying profile and the flip angle increases in the primary direction of flow to create more uniform vessel contrast across the slab [47] (see Fig.2.5 (b) and (c)).

To further improve vessel-to-background ratios additional magnetization transfer (MT) RF-pulses are applied [51–53]. These off-resonant pulses saturate the magnetization of large molecules while having minimal effect of the free water molecules. Due to exchange between free water and saturated macromolecule pools the signal of static tissue is suppressed while blood remains unaffected [47].

Commonly, an additional RF-pulse is applied to saturate venous blood. The corresponding venous saturation slab is positioned above the imaging slab and 90°-pulses are used to suppress venous signal. Therefore, ToF angiograms produced by Maximum Intensity Projections (MIPs) are not contaminated by veins. The effect of MT and saturation pulses is shown in Fig.2.5 (d).

## 2.3 Ultra-high field (UHF) MRI

In MRI, the available SNR scales with the static magnetic field $B_0$ (see equation 2.3). Thus, over the past decades major efforts to increase the static magnetic field have been made. To date, UHF MRI ($B_0 \geq 7T$) utilizes this boost in SNR to increase imaging resolution, reduce acquisition time, or a combination of both. Besides increased SNR, going to UHF creates several advantages, but also challenges. In the following, factors relevant to the subject of this thesis will be introduced. Comprehensive reviews of potentials and challenges of UHF MRI can be found elsewhere [3, 4, 54, 55].

### SNR and CNR at UHF

Eq. 2.3 suggests that the magnetization in equilibrium and therefore the available SNR scales linearly with $B_0$. Recent empirical studies however observed a supralinear increase [56]. Regardless of the exact scaling factor, the boost in SNR at UHF can be used to acquire higher imaging resolution [3]. By increasing the imaging resolution, hence reducing the voxel size, the *partial volume effect* is reduced. In general, the partial volume effect stems from the fact that the signal within a voxel is the weighted sum of all structures inside of it. If the signal fraction of a small structure within a voxel is not sufficiently high, the reconstructed voxel's gray value will be dominated by the surrounding tissue and the small structure is not depicted. The reduced partial volume effect of sub-millimeter MRI at UHF has been used to reliably visualize anatomical features previously not detectable or only with limited level of detail

such as the Line of Gennari [57, 58] and substantia nigra nigrosome 1 [59]. Furthermore, in functional Magnetic Resonance Imaging (fMRI) higher spatial resolution enabled delineation of the functional response across the cortex, given rise to the field of *laminar* and *layer-specific* fMRI [60–62]. The ultimate goal of high resolution is to close the currently exciting resolution gap between invasive microscopy studies and in vivo MRI.

#### SAR at UHF

RF-pulses can not be applied unlimitedly as their electric field can induce heating of (electrically conducting) tissue [3]. To quantify and constrain the RF-power deposition, the Specific Absorption Rate (SAR) is defined as the absorbed power per unit mass (measured in W/kg). At UHF, SAR constraints are reached with lower flip angle due to the quadratic scaling of SAR with the $B_0$ field [55]. Furthermore, the shortened wavelength at UHF (see Eq. 2.2) increases the likelihood of local, RF-induced heating foci [3]. As a consequence to increased SAR, imaging is done with fewer slices, smaller flip angles, prolonged RF-pulses, or longer TR [3, 55]. Spin echo sequences are more SAR expensive due to the additional required refocusing pulse, hence, gradient echo based imaging becomes an attractive alternative at UHF [55].

#### Susceptibility at UHF

Phase changes induced by susceptibility depend on the applied field strength and echo time (see Eq. 2.24) and, therefore, these changes increase at UHF [3, 55].

Increased sensitivity to susceptibility can be problematic or beneficial depending on the application [55]. On the one hand, signal drop-outs at air-tissue boundaries increase at UHF compared to lower field strengths. On the other hand, phase-based contrasts such as QSM benefit due to increased phase shifts and faster dephasing, enabling shorter TE, hence, shorter TR and TA [3].

#### Relaxation times at UHF

Relaxation times are a function of the $B_0$ field strength. While $T_1$ relaxation times increase, $T_2^*$ relaxation times decrease [3, 55]. Depending on the imaging contrast and application, these changes are either advantageous or challenging.

#### Implications for QSM and ToF angiography

QSM and ToF angiography benefit not only from increased SNR at UHF, but also from an enhanced contrast mechanism [3].

The susceptibility induced phase differences scale linearly with the $B_0$ field. At UHF, the resulting increase in SNR and CNR enable high resolution QSM to study anatomical structures commonly not detected at clinical field strengths.

Besides the increased SNR at UHF, longer tissue $T_1$ relaxation enhance background suppression, therefore, CNR in ToF angiography allowing for higher imaging resolution. At these resolutions, ToF angiography could detect perforating vessels.

Besides their potential at UHF, both contrasts face new challenges at higher $B_0$ strengths. In the next sectionm these challenges and strategies to overcome them are presented along with applications of high resolution QSM and ToF imaging.

### 2.3.1 QSM at UHF

QSM has been used successfully at UHF and clinical field strengths to depict the human brain anatomy and venous vasculature with superb detail [8, 63]. Its quantitative information enables predictions about tissue composition [64, 65] and its strong potential for characterizing glioblastomas [66], imaging intracerebral hemorrhages [67], and for detecting cerebral microbleeds after traumatic brain injury [68] has been shown. Furthermore, QSM is applied to investigate aging [69–74], multiple sclerosis [75, 76], Alzheimer's disease [77, 78], Parkinson's disease [79, 80], Huntigton's disease [81], motor neuron disease [82], alcohol use disorder [83], and to monitor therapeutic intervention in neurodegenerative diseases [84]. By acquiring time-resolved QSM, brain function can be probed [85–88]. More comprehensive reviews of the vast applications of QSM can be found elsewhere [3, 21, 23–25].

Compared to clinical field strengths, improved SNR and CNR at UHF enable high resolution QSM which provides more accurate susceptibility estimates [89]. Furthermore, higher imaging resolutions enable to study reliably brain structures often indiscernible at clinical field strengths such as the substantia nigra nigrosome 1 [59] and layer-specific variation of iron content in cerebral cortex [90].

Going to higher field strengths and resolutions however leads to challenges. Combining wrapped phase data from multiple coils can cause open-ended fringelines, also called *phase singularities* [21, 23, 91]. If the individual coil phase offsets are not considered (see Eq. 2.24), signal cancellation can occur resulting in phase singularities which cause artifacts in the reconstructed susceptibility maps. In general, the phase offset for each coil needs to be estimated and removed prior to coil combination to prevent phase singularities. At lower field strengths, the body coil is used as a reference to estimate coil offsets and improve coil combination, but at UHF body coils are usually not available requiring more sophisticated solutions. Potential implementations to overcome this challenge are reviewed in [21, 23, 91].

An unsolved challenge in QSM is subject motion [21]. Head motion can cause spurious phase fluctuations and image shifts. The dipole inversion assumes a fixed orientation of the object to the $B_0$ field (see Eq.2.22) and that field perturbations originate purely from the underlying susceptibility distributions. Subject motion violates these assumptions and motion-induced inconsistencies could amplify errors and streaking artifacts impairing QSM reconstruction quality.

### 2.3.2 ToF angiography at UHF

At clinical field strengths, ToF angiography is established to detect pathologies of the large intracranial arteries [35–39], however, invasive DSA remains the gold standard for diagnosis of small vessels. At UHF, increased SNR and improved background suppression (due to prolonged $T_1$ relaxation) enable high resolution ToF angiography which potentially could match the spatial detail provided by DSA. As a result of higher resolutions and higher $B_0$ fields, studies reported more than 80% increase in CNR, improved depiction of higher order branches, and visualization of smaller vessels compared to 3T [92–94]. Furthermore, perforating arteries could be depicted for the first time non-invasively such as the LSAs which supply the large parts of the basal ganglia [6, 7]. Imaging the perforating and micro-vasculature could enhance our knowledge about lacunar infarcts, small vessel diseases [95, 96], and the vascular component of neurodegenerative diseases [9, 10, 92, 94]. Furthermore, aging causes the vascularization in subcortical structures to decline [97]. Initial clinical applications of 7T ToF angiography have been reported for ischemic stroke [98] and ventricular microaneurysms in Moyamoya angiopathy [99]. The SNR potential at UHF enabled time-resolved ToF acquisition to investigate functional angiography [100].

Regardless of the potential of these applications, going to higher fields and higher resolutions gives rise to two challenges: increased SAR constraints and subject motion-induced blurring of vessels. At UHF, increased SAR values prohibit to apply directly venous suppression and MT pulses which are used commonly to enhance vessel-to-background ratios at lower field strengths. To overcome these SAR constraints, several approaches have been presented. Modifying the RF-pulses can reduce the applied peak voltage, hence, reduce power deposition. To this end, Variable-Rate Selective Excitation (VERSE) [101] is commonly applied to reduce the peak voltage of excitation and saturation pulses in 7T ToF angiography [102–105](see section A.1 for further details on VERSE). Additionally sparse Saturation (sSAT) can be utilized. Instead of applying the saturation each TR it is only used in a subset of all repetitions. Depending on the saturation type the sparse scheme needs to be adjusted. MT reduces the signal of the static background. Since this contrast information is encoded in the k-space center, applying MT only during the acquisition of the central k-space lines provides a good trade-off between contrast enhancement and SAR constraints [102, 105]. Due to the long $T_1$ relaxation time of venous blood ($\geq$ 2,000 ms [106]), applying venous saturation only every $N^{th}$ repetition ($\leq$ 50 ms) reduces venous contamination effectively while operating within SAR limits [102]. Alternatively venous suppression can be applied every TR if the flip angle of the saturation if reduced [103, 104].

While several strategies to manage SAR constraints at UHF have been reported, the impact of subject motion of high resolution ToF remains undetermined. High resolution ToF angiography of a single subject at 7T showed subject motion degraded small vessel depiction [12]. At lower resolutions, a significant decrease in vessel depiction due to head motion was found in 1.5T ToF angiography [107].

## 2.4 Prospective Motion Correction (PMC)

Since its invention, motion has been an archenemy of MRI [3] because it causes image blurring, ghosting and signal drop-outs [108]. Subject motion and its induced artifacts reduce diagnostic confidence and rescans can be necessary causing substantial costs [109]. Traditional approaches to minimize motion are restraints which are only partially effective and uncomfortable and sedation or anaesthesia which are unsafe and expensive [108].

Therefore, motion correction is an essential strategy to improve image quality and reduce cost. Over the past decades, a manifold of partial solutions have been presented, but so far no universal approach has been reported [110]. Motion correction techniques are usually tailored for application in a defined anatomical region. For MRI of the brain, it is reasonable to approximate the head as a rigid body reducing the degrees of freedom (DOF) to three translational and three rotational components to fully describe subject motion. Motion can be further categorized by its pattern (periodic, quasi-periodic, continuous, or random), by its direction (in-plane or through-plane), and by its occurrence (inter-image, inter-scan, intra-scan) [111]. This thesis focuses on motion between consecutive excitations (inter-scan motion) regardless of its pattern and direction. Categorizing motion qualitatively by its amplitude is subject to study-wise definitions. Within this thesis, motion will be considered as small-scale if its amplitude is in the range of the imaging voxel size. If high resolutions ($\leq$0.5mm) are of interest, even unintentional motion due to small head drifts or breathing can induce image degradation eventually impairing delineation of small details [11, 12]. The resulting *biological resolution limit* [12] will be discussed in section 2.4.3.

To overcome the challenge of subject motion, several correction techniques have been proposed. They can be categorized into *retrospective* and *prospective* motion correction. Retrospective approaches correct motion after the data acquisition by altering the k-space data. Pure data-driven approaches minimize a cost function such as gradient entropy to estimate and correct subject motion [112]. Approaches such as PROPELLER [113] repeatedly sample the k-space center. The oversampled k-space is used as navigator information enabling retrospective motion estimates and correction. Regardless of the implementation details, retrospective approaches inherently cannot correct for *spin history effects* [108]. If excited tissue moves in or out of the imaging volume the signal detected will be a superposition of spins with different excitation history causing signal fluctuations [108]. By prospectively adjusting the imaging volume's position and orientation according to the subject motion, this challenge can be overcome. Prospective Motion Correction (PMC) approaches can be categorized by how they detect and correct motion [3]. Similar to PROPELLER, navigator information can be acquired by repeatedly sampling k-space. Subject motion is estimated during the scan within k-space [114] or by creating low resolution image volumes [115, 116]. Although these approaches require no additional hardware for motion tracking, acquiring repeatedly k-space can prolong scan times and alter the steady state signal. Alternatively, motion navigator information

can be acquired with external hardware. By attaching multiple small field probes to the subject motion can be corrected prospectively. Commonly, tracking these field probes requires additional short sequence snippets [117]. Recent approaches try to minimize this overhead by using gradient tones (sinusoidal gradient oscillations) [118] or using only sequence-native elements [119] to detect the field probes' position and orientation. Subject motion can be tracked fully independently of the MR scanner by using external optical camera systems. Over the past decade, these optical tracking systems have evolved from out-bore, multi-camera, multi-marker setups [120] to in-bore, single camera, single marker systems [121] or even markerless tracking approaches [122]. Although external systems are fully independent of the scanner, they operate in a different coordinate system [120]. Hence, the tracking information needs to be transformed from the tracking into the scanner coordinate system [108]. This process of finding the camera position with respect to the scanner's isocenter is called *cross-calibration* [120, 123] In the following the principles of PMC are explained followed by a breif review of Moiré Phase Tracking (MPT), XPACE, and motion correction for high resolution MRI. For more information about PMC in general the interested reader is referred to [108, 110, 111].

### 2.4.1 Principles of PMC

The goal of PMC is to maintain a constant relationship between imaging volume and imaged object [108]. Assuming the head to be rigid, motion is fully described by six DOF. In MRI data is acquired in the k-space, thus, the frequency domain, while the subject moves in the image domain. Rotations around the coordinate origin are equivalent in image and k-space [112, 124]. If the subject rotates its head, the imaging volume needs to be rotated accordingly. Rotation of the imaging volume can be realized by superimposing gradients produced by the three physical gradient coils in x-, y-, and z-direction [108]. Correction of translational motion is realized by changing the RF transmit frequency and receive phase [108]. Through-plane translation requires to update the frequency of the transmit pulse because spins are excited only if transmit and local precession frequency match. Analogous to the *Fourier Shift Theorem*, in-plane translation causes multiplication of the motion corrupted k-space line with a linear phase ramp and can be corrected by setting the phase of the receiver accordingly [108, 112, 124].

### 2.4.2 Moiré Phase Tracking system and XPACE

To enable PMC an external, optical tracking system is used in this thesis. This marker-based Moiré Phase Tracking (MPT) system (Metria Innovation, Milwaukee, Wisconsin, USA) consists of:

- a single marker ($15 \times 15\text{mm}^2$) attached rigidly to the subject's teeth via individually made mouthpiece (based on dental impression) as shown in Fig. 2.6;
- a single, in-bore camera positioned above the subject's head in the scanner, operating at 80 frames per second (see Fig. 2.7);

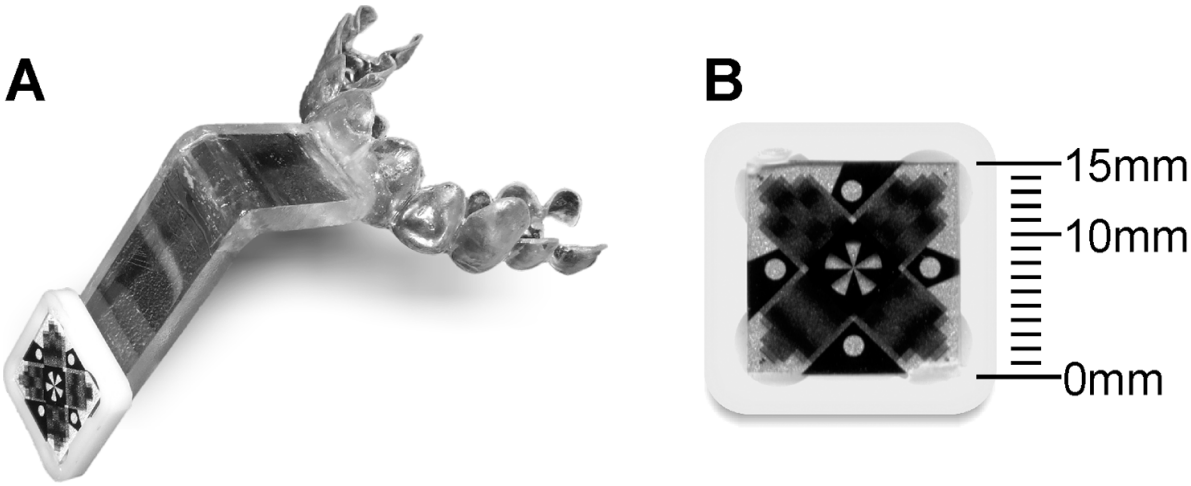


Figure 2.6: (A) individually made mouth piece wih the MPT marker attached. (B) close-up of the MPT maker.
Moiré Phase Tracking (MPT).
Reproduced without changes from [12] (published under the CC BY 4.0 license creativecommons.org/licenses/by/4.0/)

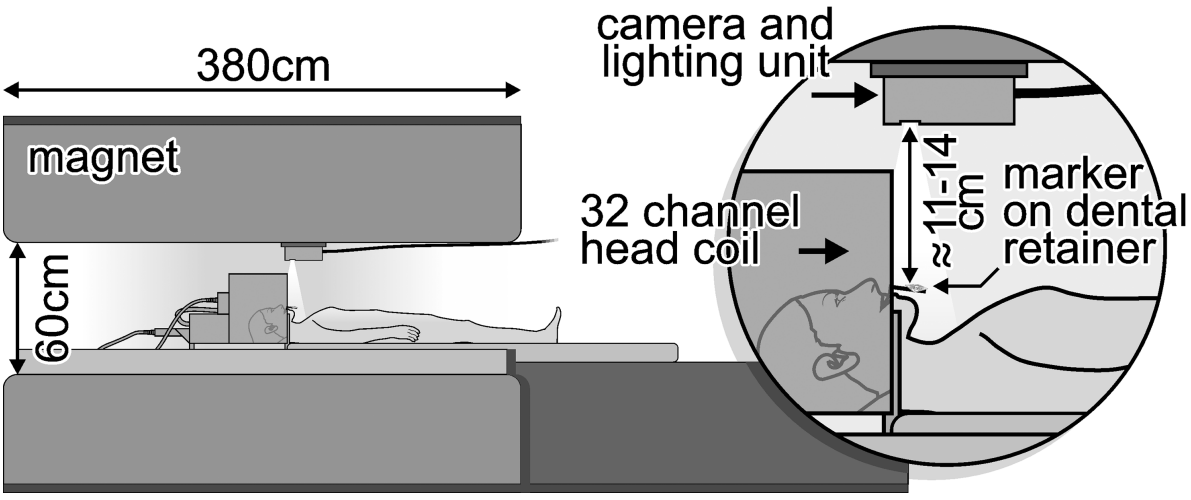


Figure 2.7: MPT set up showing the camera installed above the subject and the MPT marker attached via mouthpiece (dental retainer) to the subject
Moiré Phase Tracking (MPT).
Reproduced without changes from [12] (published under the CC BY 4.0 license creativecommons.org/licenses/by/4.0/)

- and a tracking computer to estimate the marker's, hence, subject's position and orientation in six DOF with 0.01 mm and 0.01° precision [121].

Pose estimates in six DOF with a single marker – single camera setup are possible due to the MPT marker's Moiré patterns which are created lithographically and change under though-plane rotation. Hence, rotations can be estimated by fitting sinusoidal functions to the grey values of the pixels along these patterns and the remaining four DOF can be estimated using standard photogrammetric techniques [12, 121].

The tracking process stores the motion estimates in log files and sends them to the scanner network as UDP packages. These packages are then used to update the imaging volume every TR to keep a constant relationship between head and imaging volume. PMC has to be implemented in the sequence source code to enable quasi real-time updates. To that end, IDEA (Siemens' environment for sequence programming) can be used to implement motion correction with XPACE. XPACE is a library developed by *Zaitsev et al.* [120] and provides the functionality to automatically grab the most recent tracking information from a *last in - first out* buffer, applying the cross-calibration transform, compute the offset with respect to the initial pose, and update the imaging volume's position and orientation. Therefore, the sequence developer has to implement the motion correction scheme within the dedicated sequence, but is not required to write an entire PMC back-end.

In Fig. 2.8 a summary of the PMC workflow with an external tracking is given:

1. The subject lies in the scanner. A sinlge MPT marker is attached rigidly to the subject via a custom built mouth piece to enable motion detection.
2. A single in-bore camera captures the marker with 80 frames per second and transmits the stream to a dedicated tracking PC
3. Motion estimates are computed for each frame and distributed to the scanner network via UDP packages.
4. The cross-calibration transform is applied to the tracking data to provide the motion estimates within the scanner's coordinate system. The cross-calibration transform itself needs to be estimate prior to scan [120, 123].
5. Relative changes in position and orientation of the current to the initial head pose are computed.
6. The position and orientation of the imaging volume are updated prior to every excitation according to the estimated relative change.
7. A motion-corrected k-space line is acquired.

This process is repeated until data acquisition in completed.

### 2.4.3 Motion correction for high resolution MRI

At clinically available field strengths, motion correction is applied to improve diagnostic confidence. To that end, motion correction approaches are commonly evaluated in presence of deliberate, large-scale motion [107, 112, 120]. In this thesis, the focus is on correcting

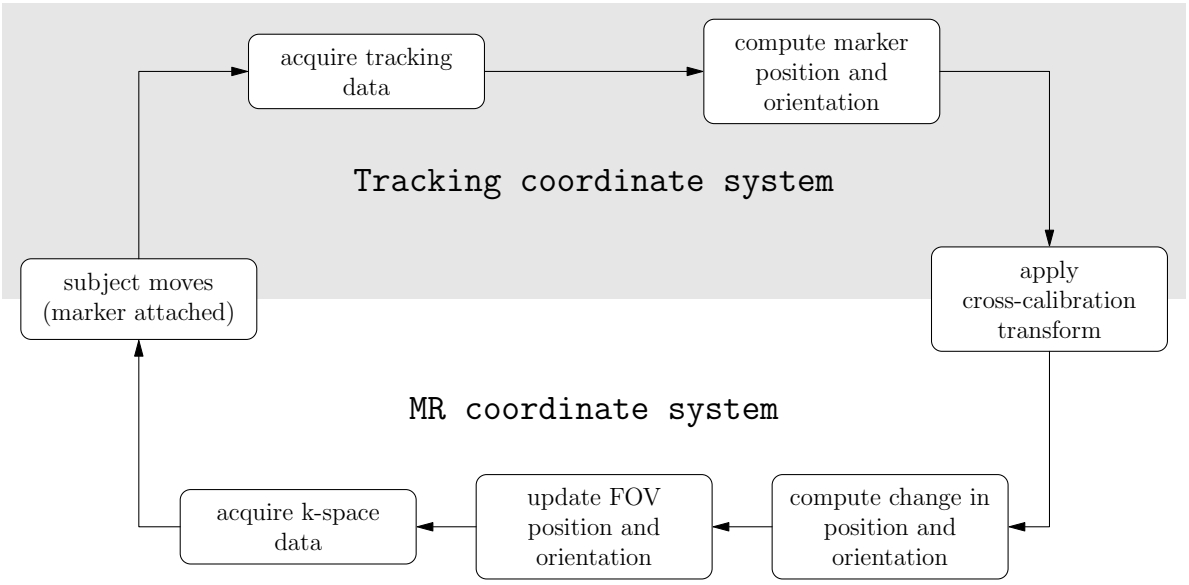


Figure 2.8: Flowchart for PMC with an external tracking system
Field of View (FOV); Prospective Motion Correction (PMC).

unintentional motion in the sub-millimeter/degree regime to improve high resolution MRI. With UHF and its high resolution capacities, MRI attempts to close the gap between in vivo imaging and invasive microscopy [3]. Although UHF provides increased SNR, high resolution imaging requires long acquisition times, hence, increasing the sensitivity to motion artifacts because subject motion during long scans is more likely and, with smaller voxel sizes, MRI is more susceptible to subject motion [3]. At voxel sizes $\leq (0.5\text{mm})^3$ even breathing and slow head drifts can induce image artifacts creating a so-called *biological resolution limit* [11, 12]. Therefore, increasing the nominal resolution will not necessarily improve perceived level of detail as motion-induced artifacts reduce the effective image resolution.

MPT is an excellent candidate for motion correction at high resolutions and has been used to overcome the biological resolution limt [12]. It enabled the highest resolution human in vivo brain scan to date: a 250 µm isotropic MPRAGE acquired by our group in 8 sessions with a total of seven hours of scanning [13, 14]. Furthermore, MPT is commonly considered as the gold standard due to its high tracking precision (0.01 mm and 0.01° [121]). A comparison to field probe-based correction showed good agreement of motion estimates but image quality for MP2RAGE measurements was superior with MPT [125]. Retrospective motion correction with fat navigators (FatNavs) [126] have been successfully applied to acquire high resolution MRI with isotropic voxel sizes of up to 380 µm for turbo spin echo as well as GRE and 350 µm for MP2RAGE [127]. Thus, FatNavs and MPT are the only tracking modalities used to correct subject motion in very high resolution MRI to date.

### Comparison of MPT and FatNavs

In a recent study — jointly authored by Frédéric Gretsch and the author of this thesis — MPT and FatNavs were compared [128]. FatNavs are short fat-selective navigators inserted into a host sequence to estimate the subject's head position and orientation [126]. By acquiring repeatedly these navigators throughout the image acquisition, the FatNavs volumes can be reconstructed and co-registered to each other after the acquisition is completed. The resulting motion estimates are then used to correct subject motion in the host sequence's k-space retrospectively.

In the first experiment, the agreement between both tracking modalities was evaluated for different subject motion patterns. Therefore, the focus was solely on the computed motion trajectories and FatNavs were acquired back-to-back (no host sequence used), while the subject was simultaneously tracked with MPT. Overall, good agreement between motion estimates of both modalities was found, while for unintentional motion higher spatial resolution of the FatNavs was favourable. To improve fast motion tracking, the temporal resolution of the FatNavs should be increased at the expense of decreased spatial resolution.

In the second experiment, image quality after retrospective motion correction using motion estimates from FatNavs and MPT was investigated qualitatively and quantitatively. To that end, MP2RAGE scans with 500 µm isotropic voxel size and whole brain coverage were acquired in a cohort of nine compliant subject, which were asked not to move. Per subject, two MP2RAGE scans were acquired. For 33 out of 36 cases the reconstruction quality with MPT and FatNavs was at par, while compared to the uncorrected images, image quality improved independent of the tracking modality. In the remaining three cases, both modalities suffered from their respective shortcomings. For MPT, one subject with unreliable marker attachment resulted in unreliable motion estimates. For FatNavs, deep breathing motion patterns could not be detected due to the poor temporal resolution of the tracking modality.

Although, MPT requires additional hardware and cross-calibration, it is the more suitable tracking modality with respect to the goal of this thesis. Unlike MP2RAGE, the GRE protocols used here have no deadtime available and are set up to acquire only certain parts of the brain (no whole brain coverage, slab-selective excitation). Thus, inserting FatNavs into the acquisition would prolong the scan acquisition and potential spin-history effects, which are of relevance in slab selective sequences, cannot be addressed by retrospective motion correction. Furthermore, FatNavs can alter the magnetization's steady state and do not match the temporal resolution provided by MPT.

## 2.5 Potential of high resolution, motion-corrected, GRE-based MRI

Motion correction for high resolution QSM has not been investigated, even though motion-induced blurring is estimated to be a major limitation [21]. For ToF angiography, successful implementation of PMC has been reported at 1.5T [107] and for a single subject at 7T [12]

indicating the necessity of motion correction at low and high resolutions to increase the effective resolution of angiographic imaging. PMC for high resolution ToF angiography at 7T has not been investigated comprehensively and the single subject study at 7T was performed without venouse and MT saturation pulses.

Arguably, the full potential of high resolution QSM and ToF angiography is currently underutilized due to motion-induced image degradation. Although, both contrast mechanisms benefit from increased SNR and CNR at UHF and, therefore, considerably higher resolution should be possible, subject motion limits this potential. At high resolutions, both 3D encoded sequences with long acquisition times are very susceptible to subject motion. Due to the biological resolution limit even unintentional, small-scale motion can reduce the effective image resolution. Hence, acquiring nominal higher resolutions with prolonged scan times and increased susceptibility to motion artifacts is less favorable than acquiring data at lower resolutions with shorter TA.

To unleash the full resolution capabilities of both GRE-based sequences PMC should be applied. To that end, MPT-based prospective correction will be used. MPT has been applied successfully for up to 250 µm isotropic resolution [14] showing its potential for ultra-high resolution MRI. Furthermore, challenges due to UHF such as phase unwrapping for QSM and SAR constraints for ToF angiography need to be overcome to enable optimal practicability. In the following chapters, the implementation and evaluation of motion-corrected QSM and ToF angiography at previously unreceived resolutions are presented.

# 3 High resolution, motion-corrected QSM

This chapter is based on the previously published paper:

- H. Mattern, A. Sciarra, F. Lüsebrink, J. Acosta-Cabronero, and O. Speck, "Prospective motion correction improves high-resolution quantitative susceptibility mapping at 7T," *Magnetic Resonance in Medicine*, vol. 81, no. 3, pp. 1605–1619, 2019

Preliminary results of this study have been presented on conferences:

- H. Mattern, J. Acosta-Cabronero, A. Sciarra, and O. Speck, "Prospectively motioncorrected QSM at 7 Tesla," in *ESMRMB 2016, 33rd Annual Scientific Meeting, Vienna, AT, September 29 - October 1: Abstracts, Saturday*, 2016
- H. Mattern, J. Acosta-Cabronero, A. Sciarra, and O. Speck, "Prospective motion correction for high-resolution QSM," in *4th International Workshop on Quantitative Susceptibility Mapping*, 2016
- H. Mattern, J. Acosta-Cabronero, A. Sciarra, and O. Speck, "Prospectively motion corrected QSM-based venograms at 7 Tesla," in *7th Annual Scientific Symposium Ultrahigh Field Magnetic Resonance*, 2016

The high quality of the here presented, motion-corrected data was used so far in three further studies (two co-authored by the author of this thesis) for the development of new QSM reconstruction techniques:

- J. Acosta-Cabronero, C. Milovic, H. Mattern, C. Tejos, O. Speck, and M. F. Callaghan, "A robust multi-scale approach to quantitative susceptibility mapping," *NeuroImage*, 2018
- C. Milovic, J. Acosta-Cabronero, J. M. Pinto, H. Mattern, M. Andia, S. Uribe, and C. Tejos, "A new discrete dipole kernel for quantitative susceptibility mapping," *Magnetic resonance imaging*, 2018
- C. Milovic, B. Bilgic, B. Zhao, J. Acosta-Cabronero, and C. Tejos, "Fast nonlinear susceptibility inversion with variational regularization," *Magnetic resonance in medicine*, 2018

## 3.1 Objective

At UHF, QSM hold tremendous potential to depict the human anatomy and venous vasculature at high resolution (see section 2.3.1). However, subject motion limits this potential. With increasing resolution MRI becomes more susceptible to motion artifacts. At very high resolutions, unintentional, small-scale motions (e.g. breathing and slow head drifts) are of the same order as the imaging voxel size, resulting in the so-called biological resolution limit [12]. If not corrected, inevitable, physiological motion can degrade the effective image resolution and introduce spurious phase fluctuations. The resulting inconsistencies between the measured

field and the magnetoscatic principles governing the dipole inversion could amplify streaking artifacts and errors in susceptibility estimates. In this study, PMC is applied to high resolution QSM to overcome the biological resolution limit and reduce phase contamination due to subject motion. To that end, a GRE sequence with PMC functionality was combined with high resolution QSM reconstructions optimized for UHF. Motion-corrected and uncorrected data is compared qualitatively and quantitatively in different motion regimes. Susceptibility maps and venograms with up to 0.33 mm isotropic resolution are reconstructed to demonstrate the capabilities of motion-corrected QSM to depict anatomical and vascular features often indiscernible at lower (effective) resolution.

## 3.2 Methods

### 3.2.1 Subjects & imaging protocol

Four healthy subjects (30 ±4 years; one female) participated after given written consent in this study (approved by local ethics committee). Retrospectively, subjects were labeled from low (subject #1) to high (subject #4) based on the average rotational movement observed during the uncorrected scan (see Tab. 3.1).

Image acquisition was performed with a 7 T whole body MRI (Siemens Healthineers, Erlangen, Germany) equipped with a 32-channel head coil (Nova Medical, Wilmington, Massachusetts, USA). To increase reproducibility of subject positioning and minimize motion, pillows were placed in between the head and coil. Unless mentioned explicitly, subjects were instructed not to move during image acquisition. In this study, motion approximately on the order of the voxel size was classified as small.

A spoiled, fully flow-compensated, fully sampled, 3D GRE sequence with PMC functionality was used to scan all subjects using: TR/TE: 20/9.09 ms; 10°flip angle; 200×166×110 $mm^3$ FOV; 0.33×0.33×1.25 $mm^3$ voxel size; receiver bandwidth: 120 Hz/pixel; and acquisition time 17:30 min. For each coil element magnitude and phase images were saved individually. The TE was selected empirically to provide sufficient susceptibility weighting while enabling shorter TR, hence, enabling a shorter acquisition time.

For each individual subject, motion-corrected and uncorrected scans were performed back-to-back in randomized order. Subject motion trajectories were tracked and stored for all motion-corrected and uncorrected scans. With PMC enabled, the imaging volume's position and orientation were updated according to the performed motion prior to each excitation (prospective correction per k-space line).

To assess the effect of small versus large motion on QSM, motion-corrected and uncorrected scans of subject #3 were acquired in presence of unintentional as well as intentional motion. During scans with unintentional motion the subject remained as still as possible, while for scans with intentional motion the subject alternated between periods of transition into a new position and periods of rest. Hence, in total four datasets of subject #3 were acquired:

1.) with PMC during unintentional, small motion (On/UnMo)
2.) with PMC during intentional, large motion (On/InMo)
3.) without PMC during unintentional, small motion (Off/UnMo)
4.) without PMC during intentional, large motion (Off/InMo)

To investigate the potential of high resolution, motion-corrected QSM, data with 330 µm isotropic voxel size was acquired of subject #3. To that end, the previous protocol was modified as follows: 200×166×1480 $mm^3$ FOV; receiver bandwidth: 130 Hz/pixel; 6/8 partial Fourier in both phase encoding directions; two averages; acquisition time 1:25h. To provide sufficient SNR, the high resolution protocol was acquired twice on different days. In total the acquisition of both datasets (in total four averages) required approximately 3h scan time. QSM reconstructions were performed for each dataset individually and, subsequently, both susceptibility maps were co-registered using ANTs v2.1 [136] ('antsRegistrationSyN.sh' performing rigid, affine, and deformable SyN registration in a multi-resolution routine).

To resolve the underlying anatomy, a high resolution, motion-corrected 3D MPRAGE dataset of subject #3 was acquired: TR/inversion time/TE: 2820/1050/2.82 ms; 5°flip angle; 225×225×187.2 $mm^3$ FOV; 0.45 mm isotropic voxel size; receiver bandwidth: 170 Hz/pixel; GRAPPA factor 2 and 24 reference lines; 6/8 slice partial Fourier; acquisition time 12:11 min.

### 3.2.2 PMC for QSM

Head motion during QSM data acquisition was corrected prospectively as described in section 2.4. In brief, prior to every excitation the orientation and position of the imaging volume was adjusted to follow the subject's head motion. Subject motion was estimated using the MPT system by tracking a marker attached rigidly to the subject via a custom built mouthpiece with an in-bore camera.

### 3.2.3 QSM reconstruction

The pipeline design and parameters of the QSM reconstruction were optimized empirically to preserve small structures in the susceptibility maps and consisted of the following steps (summarized in Fig. 3.1):

1.) Combine magnitude images with root-sum-of squares and generate brain mask with BET2 (provided by FSL [137], fractional threshold set to 0.1).
2.) Process per channel the raw phase with HARPERELLA [138] (iterative method based on the superposition principle of phase Laplacians and derived from the SMV concept [64]) to obtain unwrapped, background filtered, offset normalized phase data (see A.3.1). To that end, the radius of the convolving sphere was set to 10 mm. This radius was used to calculate the Laplacian outside the FOV and also defined the thickness of the brain boundary region. Furthermore, the FOV was zero padded in all three dimension by 100, 100, and 50 voxels, respectively, to minimize aliasing errors and improve numerical accuracy. Subsequently, 200 iterations were computed to approximate the phase Laplacian

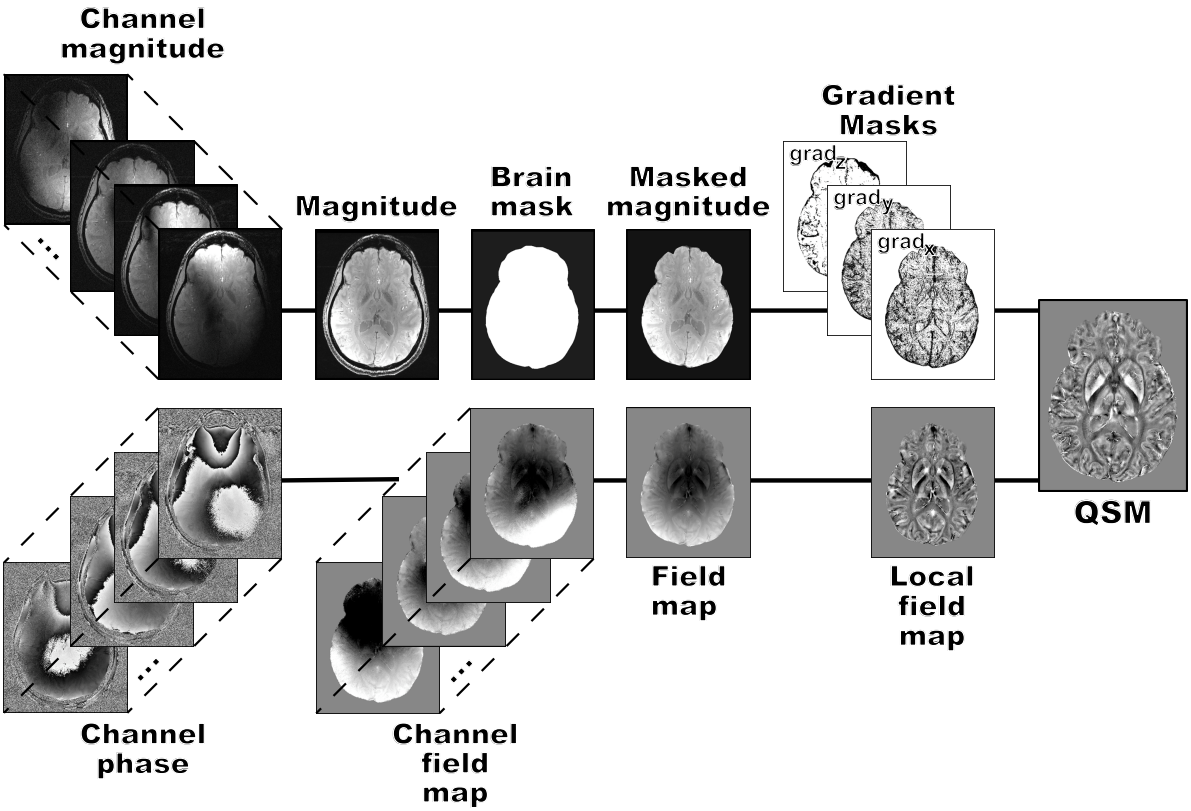


Figure 3.1: Proposed processing pipeline for QSM at ultra-high field. First, channel-wise magnitude images were combined with a standard root-sum-of-squares method to create a brain mask. Subsequently, the combined field map was inferred from magnitude-weighted, HARPERELLA-processed channel phases. Locally sourced inductions were subsequently revealed by SMV filtering with spatially varying spherical kernels. Finally, $l_1$-norm based regularized QSM inversions were performed using the nMEDI method.
HARmonic (background) PhasE REmovaL using the LAplacian operator (HARPERELLA); non-linear, morphology-enabled, dipole inversion (nMEDI); Quantitative Susceptibility Mapping (QSM); Spherical Mean Value (SMV).

outside the brain-boundary region.

3.) Use magnitude-weighted linear phase combination to compute a single field map from the channel-wise filtered phase data.

4.) Within the brain mask, apply SMV filtering with spatially varying spherical kernels [32] to further extract harmonic phases from the field map and, therefore, reveal locally-sourced inductions (see A.3.1). SMV kernel radius was set to 25 mm in the center of the brain and decreased to 1 mm at the boundary of the brain. No further deconvolution was applied.

5.) Reconstruct susceptibility maps using $l_1$-norm penalty-based, non-linear, morphology-enabled, dipole inversion (nMEDI) method with dynamic model error reduction through iterative tuning (MERIT) and Lagrange multiplier set empirically to 1,000 [30, 139]

(see A.3.2).

Of note, if not optimally implemented (e.g. single-threaded), channel-wise preprocessing of the raw phase data is time consuming. However, the presented method accurately normalized channel-specific phase offsets and, therefore, enabled magnitude-weighted linear phase combinations without phase singularity errors. These singularities occur when complex data with high resolution or low SNR are combined and can impair QSM reconstructions.

### 3.2.4 Venogram calculation

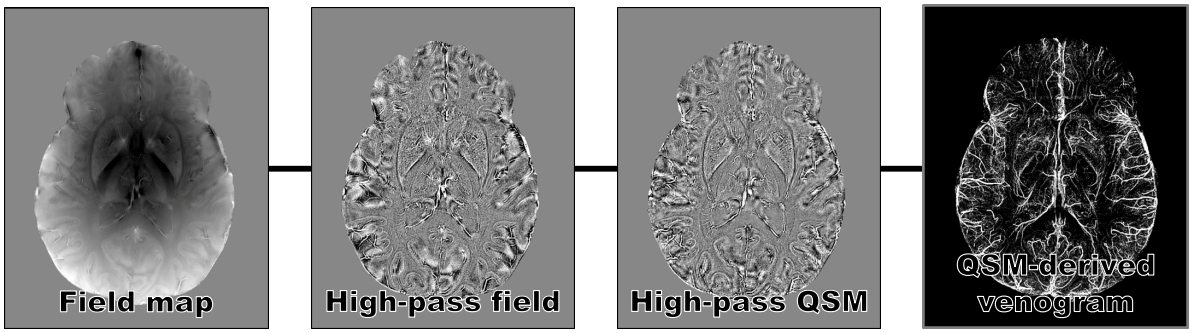


Figure 3.2: Illustration of the intermediate steps for QSM-based venogram estimation. The field map — computed as shown in Fig. 3.1 — was high-pass filtered to suppress low spatial frequencies, and was subsequently inverted with the nMEDI approach. After upsampling along the head-foot direction to improve vessel continuity, maximum QSM projections were computed, which revealed the hyperintense venous vasculature.
non-linear, morphology-enabled, dipole inversion (nMEDI); Quantitative Susceptibility Mapping (QSM).

The preprocessing for the reconstruction of venograms was identical to the QSM pipeline: First, a brain mask was generated. Subsequently, the channel-wise raw phase was processed with HARPERELLA to obtain unwrapped, background filtered, offset normalized phase data. Finally, a field map was generated by magnitude-weighted linear combination of the channel-wise phase information. In contrast to the QSM reconstruction, the field map was high-pass filtered with the variable SMV approach (starting radius of 3 mm instead of 25 mm) prior to the nMEDI processing (see Fig. 3.2). Small SMV radii suppress low spatial frequencies and, therefore, suppress large-scale image features. By suppressing low spatial frequencies, small-scale structures such as the vasculature are enhanced in the field map. After reconstructing high-passed susceptibility maps, these maps were up-sampled to isotropic voxel size of 330 µm by performing b-spline interpolation in slice direction to improve vessel continuity. QSM-based venograms were generated by computing maximum susceptibility projections over 60 slices (19.80 mm), since in QSM veins return high susceptibility values, unlike in Susceptibility Weighted Imaging (SWI). The order of interpolation and projection was chosen empirically. Interpolation followed by maximum intensity projection provided visually the best vessel

continuity compared to first performing projection and then interpolation, or performing no interpolation at all.

For generating venograms of the 330 µm dataset the up-sampling was omitted as the voxel size was already isotropic. Furthermore, MIPs were computed over 45 slices (14.85 mm).

### 3.2.5 Extraction of regional susceptibility values

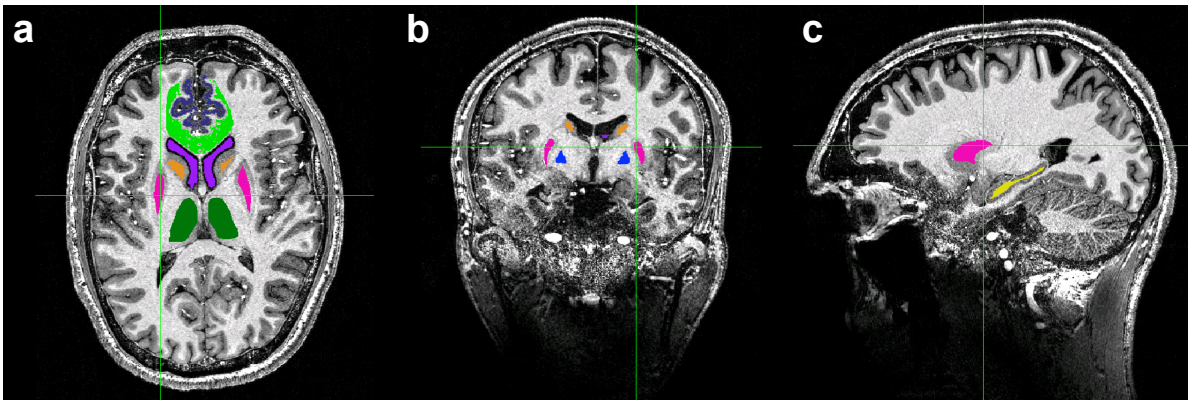


Figure 3.3: ROIs for regional susceptibility extraction overlaid onto an anatomical image: (a) axial, (b) coronal, and (c) sagittal views. ROIs: Globus pallidus (blue); caudate (orange); putamen (pink); thalamus (dark green); hippocampus (yellow); prefrontal gray matter (blue-gray); prefrontal white matter (light green); CSF (violet). cerebrospinal fluid (CSF); Region of Interest (ROI).

Regional susceptibility estimates were extracted bilaterally for all subjects in the following ROIs: globus pallidus, caudate nucleus, putamen, thalamus, hippocampus, prefrontal gray matter (GM), and prefrontal white matter (WM). Subsequently, regional susceptibility was quantified as mean ± standard deviation after merging all values from the bilaterally segmented ROIs. All susceptibility values were referenced to the mean susceptibility values of CSF in the frontal horns of the lateral ventricles.

ROI segmentation was performed on the bias field corrected (using SPM12 [140]) $T_1$-weighted MPRAGE dataset of subject #3. Subcortical ROIs were segmented automatically with FSL FIRST [141]. Segmentation of CSF, prefrontal GM, and prefrontal WM was performed semi-automatically by thresholding whole-brain CSF, GM, and WM segments provided by SPM12 at probability of 0.9, respectively. These binarized maps were then intersected separately with manually traced prefrontal ROI to generate regional tissue-specific masks. Finally, all masks were 3D-eroded by one voxel for GM and WM ROIs, by three voxels for caudate and CSF, and by five voxels for all other ROIs. Note that the erosion strength was optimized empirically to avoid edge effects. The final ROI masks were overlaid onto subject #3's MPRAGE image in Fig. 3.3

To provide the ROI masks in each individual subject space, several image registration steps were necessary. To that end, subject #3's anatomical MPRAGE data was co-registered to

the average GRE magnitude template of subject #3 using ANTs v2.1 [136] ('antsRegistrationSyN.sh' performing rigid, affine, and deformable SyN registration). This GRE magnitude template was constructed iteratively from the four GRE datasets acquired of subject #3 by applying the nonlinear 'antsMultivariateTemplateConstruction.sh' routine. Furthermore, GRE images of subject #1, #2, and #4 were co-registered individually to this template using 'antsRegistrationSyN.sh'. For each subject and ROI, the composition of inverse transformations was applied followed by nearest-neighbor interpolation to create masks in the individual subject space. Therefore, potential numerical bias due to spatial interpolation was avoided by performing susceptibility extraction in the respective, native QSM space directly.

### 3.2.6 Statistical analysis

For each scan, subject motion was summarized as mean ± standard deviation 3D translational and rotational movement, respectively. To assess significant differences in subject motion between motion-corrected and uncorrected scans non-parametric, two-sided, paired Wilcoxon signed-rank tests were performed for mean translational and rotational motion separately.

Differences in regional mean susceptibilities between motion-corrected and uncorrected scans were assessed with paired Wilcoxon signed-rank tests for each subject individually. To that end, the mean susceptibilities across all ROIs with and without PMC were compared by Wicoxon signed-rank test for each subject separately with the null hypothesis that the difference between PMC on and PMC off came from a distribution with zero median.

Non-parametric, two-sample Kolmogorov-Smirnov (KS) test statistics were used to investigate the effect of different motion amplitudes on QSM. In general, KS test statistics reflect differences between two cumulative distributions. If (uncorrected) motion affects susceptibility distributions, then measuring the same object with different motion trajectories will result in apparently different susceptibility distributions. This difference can be quantified by the KS test statistics.

To analyze the effect of motion on QSM KS tests were performed for subject #3. The following conditions were compared:

1.) PMC on: unintentional, small-scale motion versus intentional, large-scale motion (On/UnMo vs. On/InMo)
2.) PMC off: unintentional, small-scale motion versus intentional, large-scale motion (Off/UnMo vs. Off/InMo)

Thus, intra-subject, ROI-wise, KS tests were performed to assess if data from unintentional motion and data from intentional motion originate from the same distribution (null-hypothesis). It was hypothesized that, independent of the motion regime, motion-corrected distributions would appear as if drawn from the same distribution, whereas uncorrected distributions would differ, if acquired in different motion regimes. In addition to regional analysis, KS test were applied globally for whole-brain susceptibility distributions on both test conditions.

For all subjects, motion-corrected and uncorrected data were compared quantitative to

assess the impact of motion on QSM. In this inter-subject analysis, ROI-wise KS tests were performed under the null-hypothesis that susceptibility extraction acquired during unintentional motion with PMC on and PMC off originated from the same distribution. To correct for multiple-testing, the associated $P$-values for all KS tests were Bonferroni adjusted (n=42, six test conditions ×seven ROIs). Additionally, motion-corrected and uncorrected whole-brain susceptibility distributions were assessed subject-wise with KS-tests. All statistical analyses were performed with MATLAB2015b (The MathWorks, Natick, Massachusetts, USA)

## 3.3 Results

For each subject, motion estimates and regional susceptibility values are summarized in Tab. 3.1 and Tab. 3.2, respectively. To study the effect of motion amplitude on susceptibility mapping, subject #3 was scanned with and without intentional motion. To investigate the effect of unintentional motion on QSM, regional susceptibility estimates were extracted from motion-corrected and uncorrected scans for all four subjects.

Table 3.1: Summary of motion quantification across subjects and scan types. Total translation and rotation denoting observed 3D movement during the whole scan are reported as mean ± standard deviation.

| Subject | Intentional Motion | PMC | Total Translation in [mm] | Total Rotation in [°] |
|---|---|---|---|---|
| 1 | No | On | 0.49 ± 0.63 | 0.11 ± 0.18 |
| | | Off | 0.36 ± 0.26 | 0.12 ± 0.09 |
| 2 | No | On | 0.43 ± 0.12 | 0.21 ± 0.06 |
| | | Off | 1.19 ± 0.20 | 0.43 ± 0.08 |
| 3 | No | On | 2.19 ± 1.02 | 0.89 ± 0.42 |
| | | Off | 1.06 ± 0.22 | 0.45 ± 0.10 |
| 3 | Yes | On | 3.97 ± 2.03 | 1.31 ± 0.81 |
| | | Off | 1.93 ± 2.13 | 0.59 ± 0.83 |
| 4 | No | On | 1.47 ± 0.86 | 0.50 ± 0.29 |
| | | Off | 4.19 ± 1.59 | 0.68 ± 0.33 |

Prospective Motion Correction (PMC).

### 3.3.1 Intra-subject: Effect of motion amplitude on corrected and uncorrected QSM

Subject #3 was scanned under the following conditions:

1.) with motion correction during unintentional motion (On/UnMo)
2.) with correction during intentional motion (On/InMo)
3.) without correction during unintentional motion (Off/UnMo)
4.) without correction during intentional motion (Off/InMo)

Uncorrected subject motion introduced image artifacts like blurring, ringing, and signal dropout in all stages of the QSM pipeline, starting in the magnitude and phase images (see

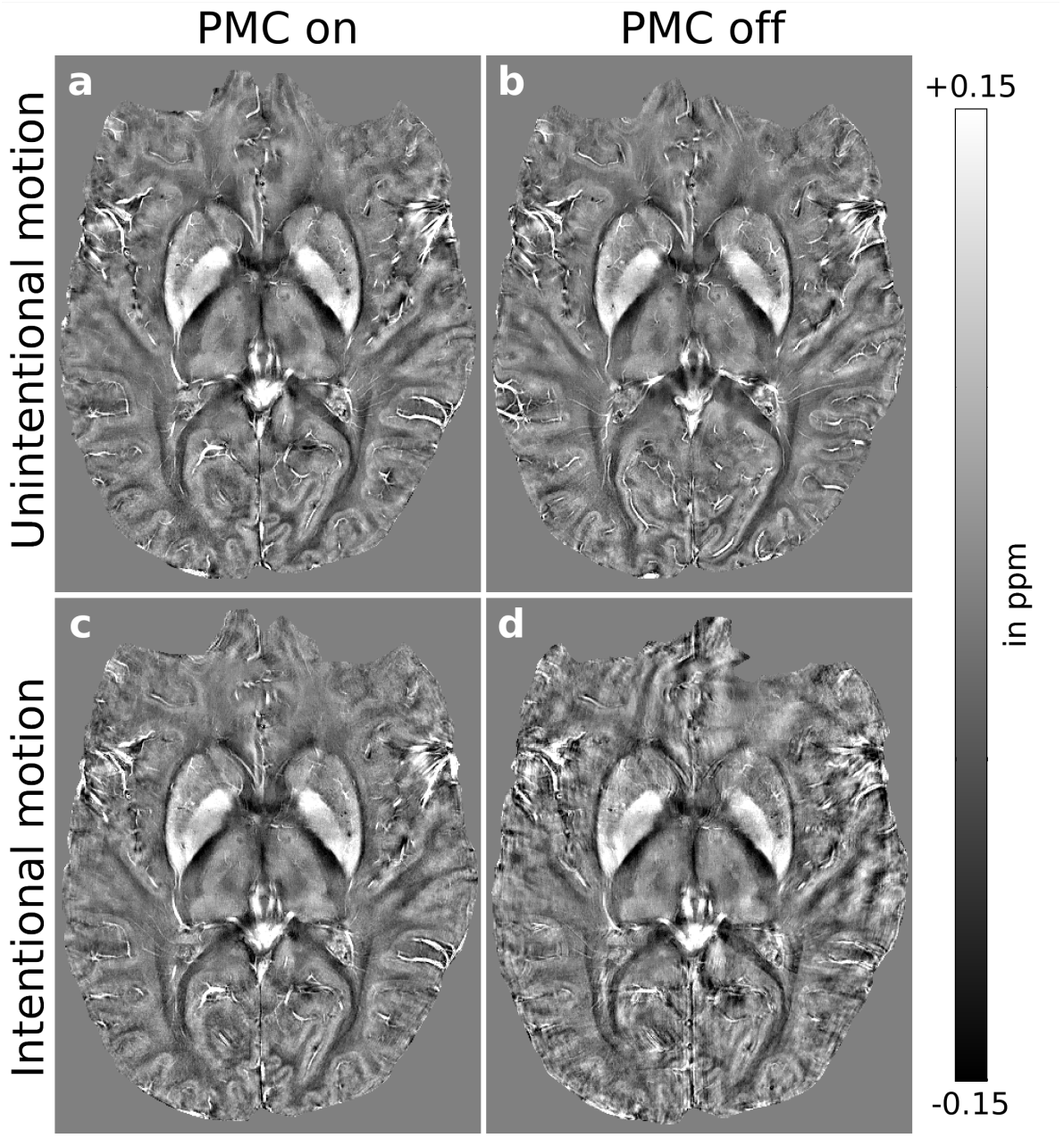


Figure 3.4: Intra-subject comparison (subject #3) of (a, c) motion-corrected and (b, d) uncorrected QSM, (a, b) without and (c, d) with intentional motion. For small-scale motion, corrected and uncorrected QSM showed no apparent motion artifacts. For large-scale motion, uncorrected maps were degraded; this effect was reduced with motion correction leading to minor residual artifacts.
Quantitative Susceptibility Mapping (QSM).

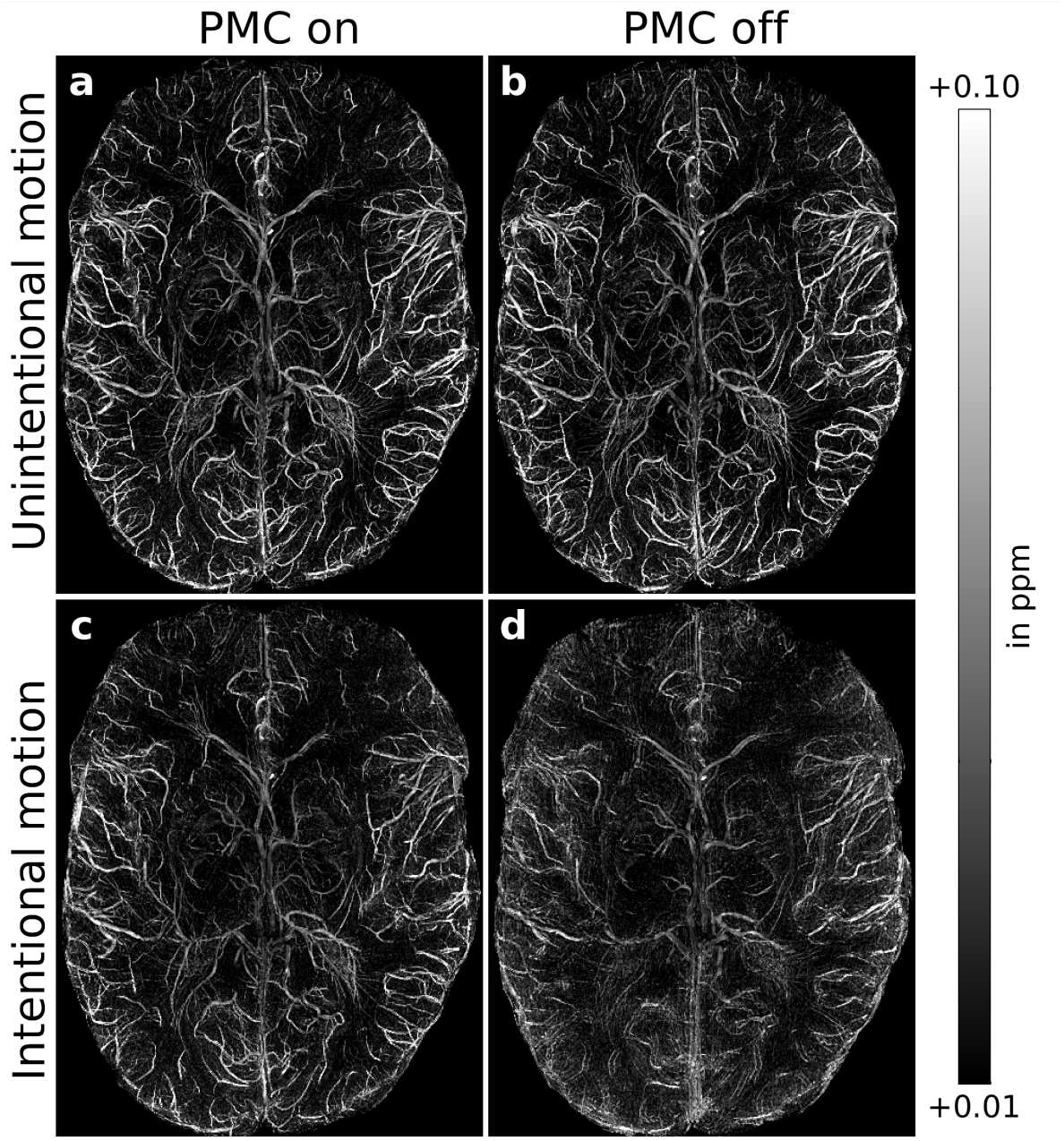


Figure 3.5: Intra-subject comparison (subject #3) of (a, c) motion-corrected and (b, d) uncorrected QSM-based venograms, (a, b) without and (c, d) with intentional motion. For small-scale motion, corrected and uncorrected QSM showed no apparent motion artifacts. Without correction, large-scale motion degraded vessel depiction considerably; this effect was largely prevented by motion correction leading to minor residual artifacts.
Quantitative Susceptibility Mapping (QSM).

Fig. B.1 and Fig. B.2), contaminating the local field maps (Fig. B.3), and degrading the final susceptibility maps and venograms (see Fig. 3.4 and Fig. 3.5). With PMC, these motion-induced artifacts could be prevented considerably.

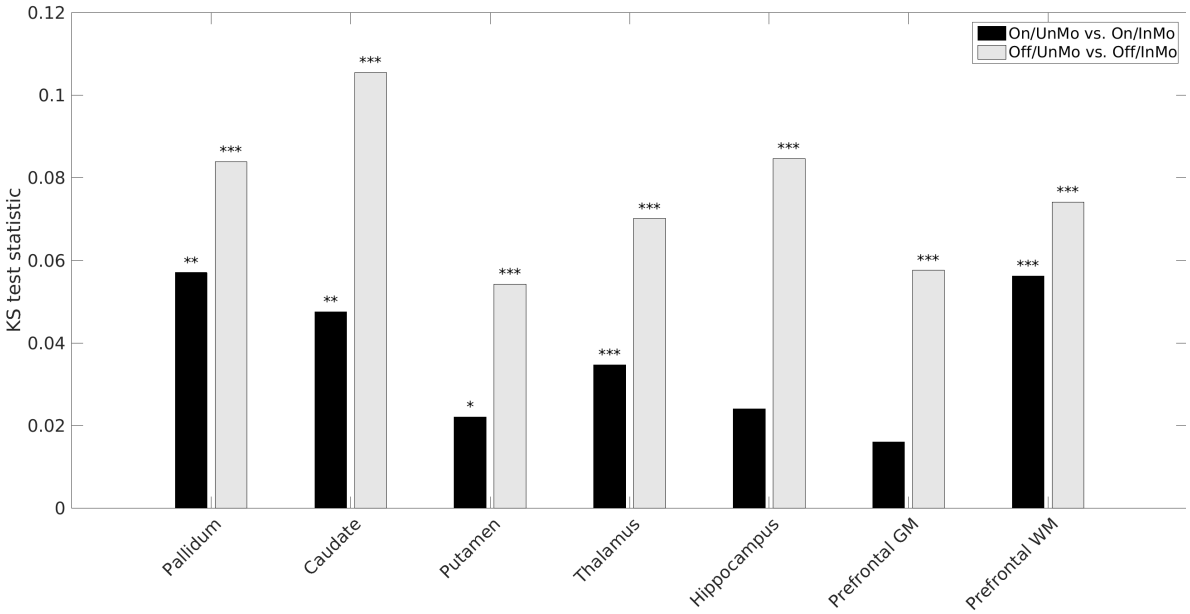


Figure 3.6: Intra-subject evaluation of regional QSM distributions using KS tests. Condition 1: PMC on, unintentional motion (On/UnMo) vs. PMC on, intentional motion (On/InMo); Condition 2: PMC off, unintentional motion (Off/UnMo) vs. PMC off, intentional motion (Off/InMo). Statistical significance denoted as * $P_{Bonferroni} < 0.01$, ** $P_{Bonferroni} < 1 \times 10^{-6}$, and *** $P_{Bonferroni} < 1 \times 10^{-12}$. Systematically lower KS test statistics were obtained for motion-corrected data. gray matter (GM); Kolmogorov-Smirnov (KS); Prospective Motion Correction (PMC); Quantitative Susceptibility Mapping (QSM); white matter (WM).

The effect of unintentional and intentional motion on local susceptibility estimates was investigated quantitatively for PMC on an off. No significant differences were detected by Wilcoxon signed-rank test between motion-corrected intentional and unintentional motion

Table 3.2: Regional susceptibility values for all subjects summarized as mean ± standard deviation.

| Subject | Intentional Motion | PMC | Pallidum | Caudate | Putamen | Thalamus | Hippocampus | Prefrontal GM | Prefrontal WM |
|---|---|---|---|---|---|---|---|---|---|
| 1 | No | On | 0.119 ± 0.051 | 0.053 ± 0.027 | 0.024 ± 0.050 | 0.030 ± 0.046 | 0.012 ± 0.033 | 0.016 ± 0.054 | 0.021 ± 0.049 |
| | | Off | 0.117 ± 0.050 | 0.053 ± 0.026 | 0.026 ± 0.049 | 0.030 ± 0.046 | 0.010 ± 0.031 | 0.017 ± 0.053 | 0.021 ± 0.048 |
| 2 | No | On | 0.107 ± 0.067 | 0.032 ± 0.044 | 0.008 ± 0.041 | 0.004 ± 0.039 | 0.004 ± 0.031 | -0.002 ± 0.043 | 0.003 ± 0.033 |
| | | Off | 0.105 ± 0.064 | 0.032 ± 0.041 | 0.010 ± 0.043 | -0.001 ± 0.041 | -0.002 ± 0.034 | -0.000 ± 0.044 | 0.001 ± 0.032 |
| 3 | No | On | 0.098 ± 0.045 | 0.026 ± 0.031 | 0.022 ± 0.045 | 0.005 ± 0.033 | -0.004 ± 0.044 | 0.002 ± 0.059 | -0.001 ± 0.035 |
| | | Off | 0.088 ± 0.043 | 0.024 ± 0.032 | 0.019 ± 0.047 | 0.004 ± 0.032 | -0.002 ± 0.043 | -0.001 ± 0.057 | 0.001 ± 0.034 |
| 3 | Yes | On | 0.093 ± 0.042 | 0.029 ± 0.031 | 0.022 ± 0.047 | 0.007 ± 0.033 | -0.004 ± 0.041 | 0.000 ± 0.056 | 0.002 ± 0.034 |
| | | Off | 0.094 ± 0.040 | 0.028 ± 0.035 | 0.016 ± 0.048 | 0.008 ± 0.035 | -0.000 ± 0.045 | -0.002 ± 0.064 | 0.001 ± 0.042 |
| 4 | No | On | 0.089 ± 0.043 | 0.030 ± 0.034 | 0.005 ± 0.041 | 0.005 ± 0.030 | 0.012 ± 0.028 | -0.002 ± 0.060 | 0.005 ± 0.035 |
| | | Off | 0.095 ± 0.054 | 0.038 ± 0.035 | 0.013 ± 0.042 | 0.012 ± 0.033 | 0.010 ± 0.028 | 0.006 ± 0.058 | 0.010 ± 0.039 |

gray matter (GM); Prospective Motion Correction (PMC); white matter (WM).

(On/UnMo vs. On/InMo, $P = 0.69$, signed-rank=11), as well as between uncorrected intentional and unintentional motion (Off/UnMo vs. Off/InMo, $P = 0.22$, signed-rank=6). Whole brain and ROI-bound susceptibility distributions were assessed with KS tests: Whole brain analysis revealed one order of magnitudes increased KS test statistics for PMC off (0.005 for On/UnMo vs. On/InMo, and 0.050 for Off/UnMo vs. Off/InMo). ROI-wise KS-tests results are shown in Fig. 3.6. Across all ROIs test statistics were systematically lower for On/UnMo vs. On/InMo than for Off/UnMo vs. Off/InMo and without motion correction all KS tests rejected the null hypothesis at $P_{Bonferroni} < 1 \times 10^{-12}$. In contrast, with motion correction enabled rejection at the same threshold level was observed only in two regions (prefrontal WM and thalamus). Further statistical differences were observed in the corpus striatum for PMC on, however at lower threshold levels than for PMC off. QSM distributions in the hippocampus and prefrontal GM were relatively unaffected by motion if PMC was applied.

### 3.3.2 Inter-subject: Comparison between motion-corrected and uncorrected QSM

Considerable motion was observed for all subjects during data acquisitions, although they were instructed not to move (see Tab. 3.1). Unintentional motion such as slow head drifts and breathing were the main source of movement. On average, 3D translational and rotational motion (1.42 mm and 0.42°, respectively) exceeded the voxel dimensions. Even though, motion estimates for corrected and uncorrected scans differed considerably for some subjects, paired Wilcoxon signed-rank tests indicated no significant differences in mean translation and rotation between motion-corrected and uncorrected scans across all subjects (P=0.88).

Table 3.3: Statistics for motion-corrected vs. uncorrected data (by subject).

| Subject | PMC On vs. Off (regional mean QSM) P-value | signed rank | PMC On vs. Off (whole-brain QSM distributions, KS test statistic) |
|---|---|---|---|
| 1 | 0.81 | 12 | 0.003 |
| 2 | 0.38 | 20 | 0.008 |
| 3 | 0.16 | 23 | 0.007 |
| 4 | 0.03 | 1 | 0.019 |

Kolmogorov-Smirnov (KS); Prospective Motion Correction (PMC); Quantitative Susceptibility Mapping (QSM).

Uncorrected motion degraded susceptibility maps (see Fig. 3.7) and venograms (see Fig. 3.8). Larger motion amplitudes induced visually traceable artifacts (see subject #4 in Fig. 3.7 and in Fig. 3.8), but also smaller motion amplitudes reduced the effective resolution. While the effect of small motion is visually less apparent for QSM, for imaging the highly paramagnetic venous vasculature small motion noticeably blurred the images (see subject #1 & #2 in Fig. 3.8). PMC could prevent this motion-induced image degradation in three out of four cases for venous depiction and in two out of four cases PMC for susceptibility mapping. For the remaining cases image quality was similar for corrected and uncorrected scans. Hence, PMC never degraded

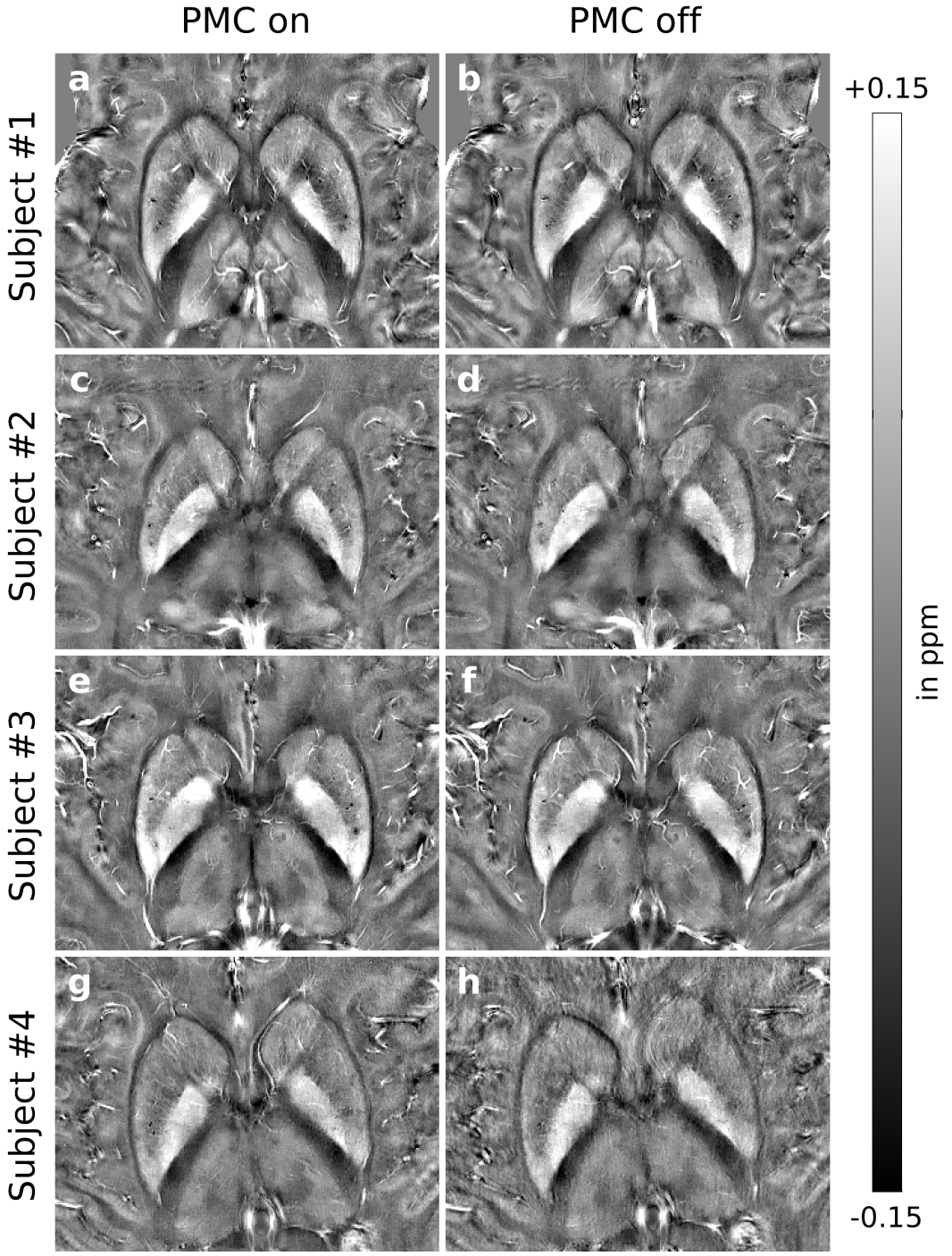


Figure 3.7: Inter-subject comparison of (a, c, e, g) motion-corrected and (b, d, f, h) uncorrected QSM. Smaller motion did not visibly degrade QSM reconstructions, whereas larger, uncorrected motion corrupted QSM. With motion correction, QSM degradation was successfully reduced in two of four subjects. For the remaining two subjects, image quality was similar with PMC on and PMC off.
Prospective Motion Correction (PMC); Quantitative Susceptibility Mapping (QSM).

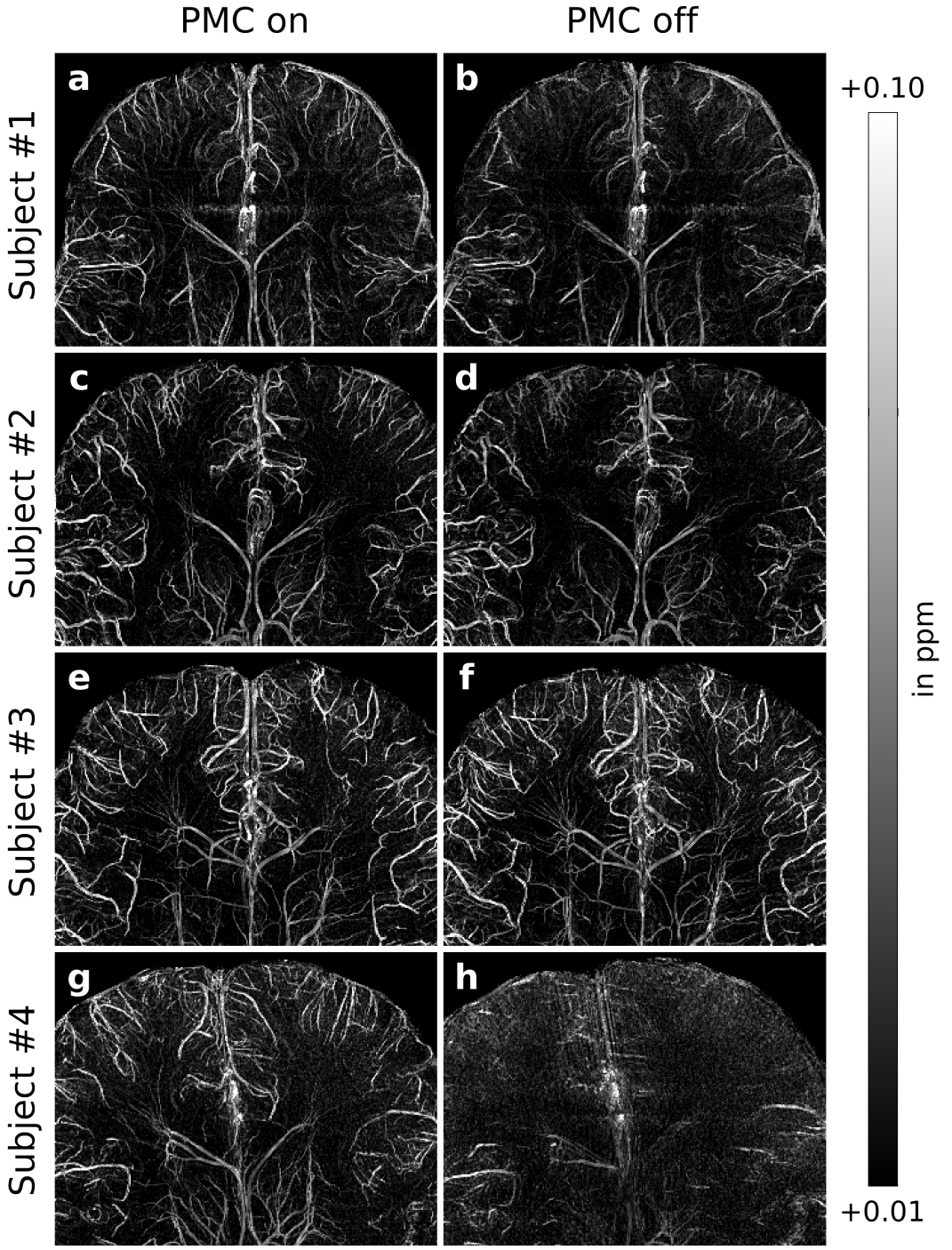


Figure 3.8: Inter-subject comparison of (a, c, e, g) motion-corrected and (b, d, f, h) uncorrected QSM-based venograms. Larger, uncorrected motion corrupted the venograms. Smaller motion (on the order of the voxel dimension) also blurred vessels — particularly across prefrontal areas (shown here). Sharper and more detailed venograms were obtained in both motion regimes with motion correction in three of four subjects. For subject #3, image quality was similar with PMC on and PMC off. Prospective Motion Correction (PMC); Quantitative Susceptibility Mapping (QSM).

reconstruction quality.

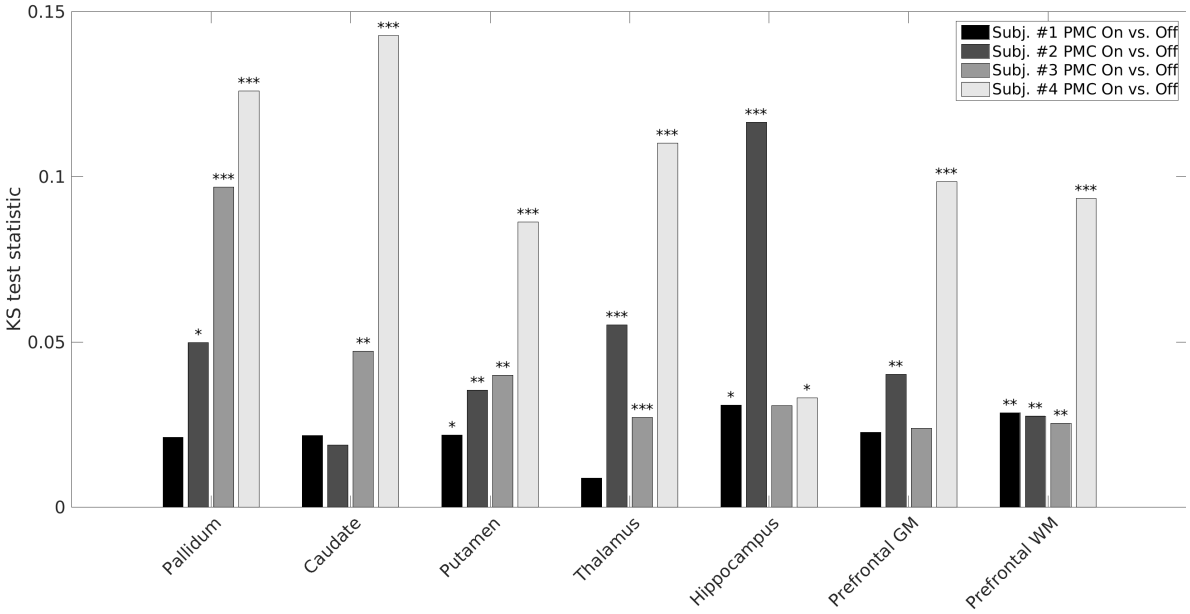


Figure 3.9: Individual KS test results comparing regional QSM distributions from motion-corrected vs. uncorrected data. Statistical significance denoted as * $P_{Bonferroni} < 0.01$, ** $P_{Bonferroni} < 1 \times 10^{-6}$, and *** $P_{Bonferroni} < 1 \times 10^{-12}$.
gray matter (GM); Kolmogorov-Smirnov (KS); Prospective Motion Correction (PMC); Quantitative Susceptibility Mapping (QSM); white matter (WM).

To compare motion-corrected and uncorrected data for each subject separately, Wilcoxon signed-rank tests were performed for regional mean susceptibilities and KS-tests for whole-brain distributions (see Tab. 3.3). For subject #4 the greatest average motion was observed, which resulted in significantly different regional mean susceptibilities (P=0.031; signed-rank=1) and the largest KS-test statistic when comparing motion-corrected and uncorrected data.

Furthermore, motion-corrected and uncorrected regional susceptibility distributions were compared with KS-tests (see Fig. 3.9). Again, subject #4 (greatest observed motion) showed the largest KS-test statistic in six out of seven cases (all at threshold level $P_{Bonferroni} < 1 \times 10^{-12}$). Subject #1 (smallest observed motion) returned the lowest KS-test statistic in three out of seven cases. The subject-wise, average KS-test statistic across all ROIs was the smallest for subject #1 (0.022), which was approximately two times lower than for subject #2 and #3 (0.049 and 0.042, respectively), and more than four times lower than for subject #4 (0.099).

### 3.3.3 QSM at 330 µm isotropic voxel resolution

Motion-corrected QSM at 330 µm isotropic resolution was acquired for a single subject. The subject was scanned in two sessions (on different days; scan time per session approximately 1.5h) to achieve sufficient SNR. During the first session the subject moved 1.20±0.66 mm/0.42±0.22° and during the second session 4.93±1.26 mm/1.73±0.44°. This

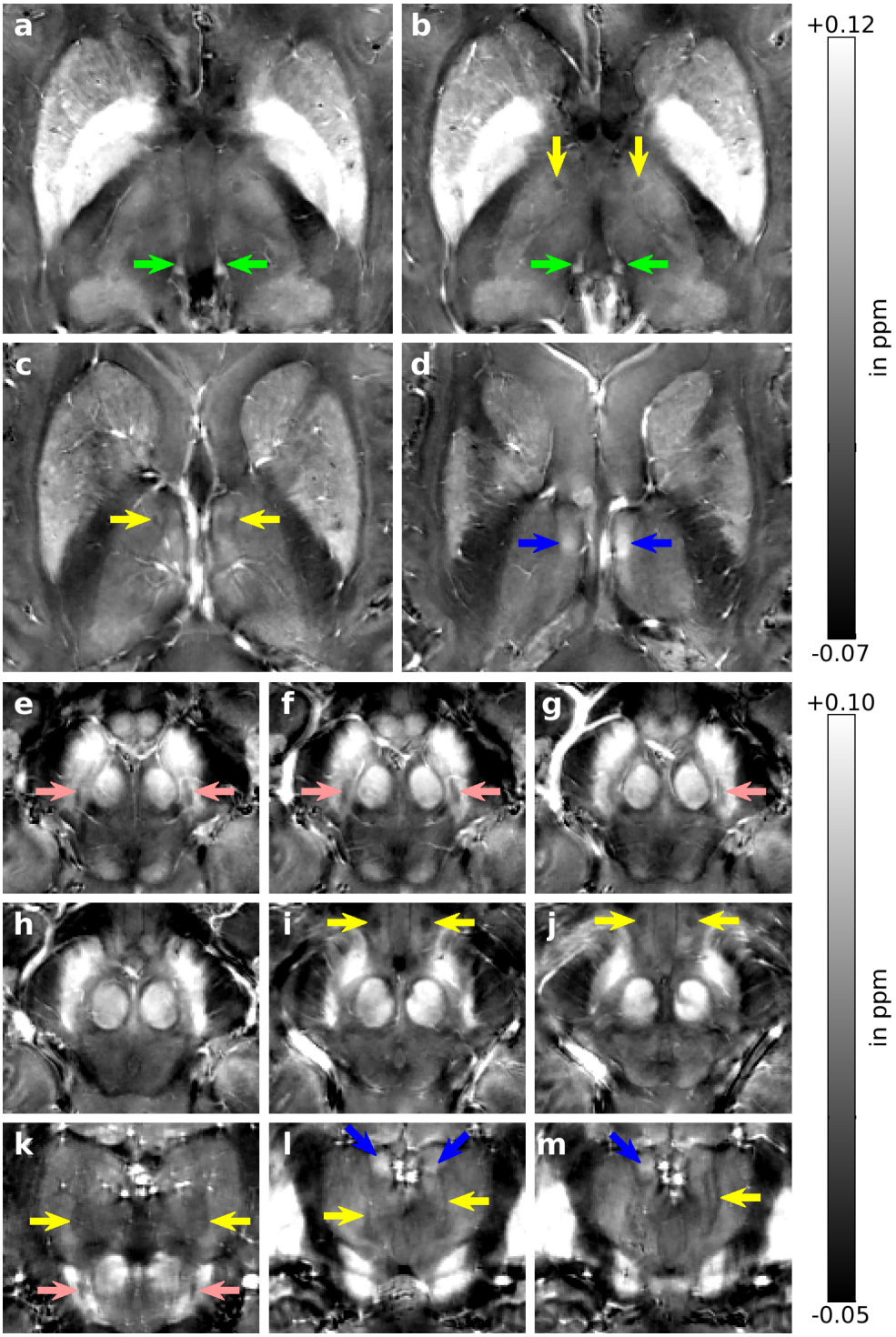


Figure 3.10: Magnified views of motion-corrected QSM at 330 µm isotropic voxel size: (a-d) axial views of corpus striatum/thalamus, (e-j) axial views of midbrain regions, and (k-m) coronal views of basal ganglia/thalamus (coronal). Arrows highlight the habenula (green), mammillothalamic tracts (yellow), anterior thalamic nuclei (blue), and substantia nigra nigrosome 1 (pink).
Quantitative Susceptibility Mapping (QSM).

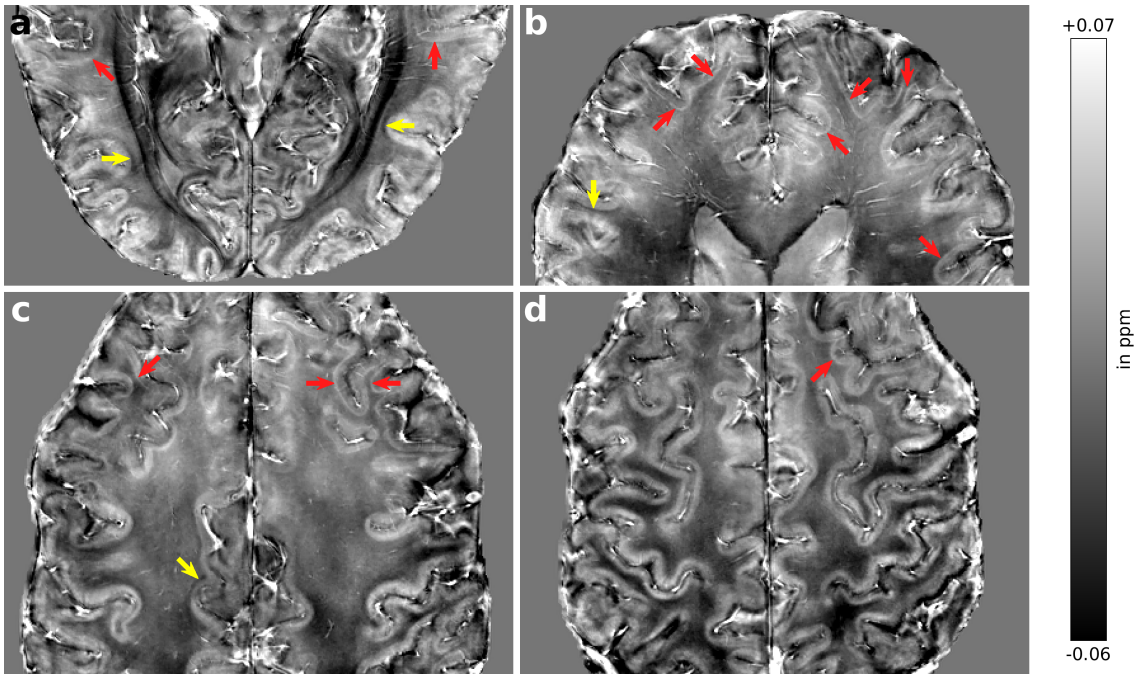


Figure 3.11: Magnified axial views of motion-corrected QSM at 330 µm isotropic voxel size across the cortex. Arrows highlight hypointense (yellow) and hyperintense (red) regions between gray matter and adjacent white matter.
Quantitative Susceptibility Mapping (QSM).

demonstrates the unpredictable nature of subject motion even when scanning the same subject twice as the average motion amplitude was approximately four times greater during the second session.

PMC enabled the reconstruction of highly detailed susceptibility maps featuring accurately depicted small brain nuclei and this structures commonly not visible due lower imaging resolutions or blurred by uncorrected subject motion.

Fig. 3.10 shows magnified axial and coronal views of the corpus striatum/diencephalic regions. Thalamic substructures such as the habenula (green arrows, Fig. 3.10a and Fig. 3.10b), anterior thalamic nucleus (blue arrows, Fig. 3.10d, Fig. 3.10l, and Fig. 3.10m) and mammillothalamic tracts (yellow arrows, Fig. 3.10) are clearly depicted. Bilateral pockets of low paramagnetism — commonly labeled as substantia nigra nigrosome 1 [59] — could be readily identified in the caudal substantia nigra (pink arrows, Fig. 3.10e-g and Fig. 3.10k). Furthermore, motion-corrected QSM depicted clearly the substantia nigra ventral surface, the subthalamic nucleus, mammillary bodies, and substructures of the red nucleus.

The cortical ribbon is a relatively thin brain structure and its depiction benefited from the combination of high imaging resolution and PMC as illustrated in magnified axial views in Fig. 3.11. Across the cortical ribbon QSM patterns can be observed as well as hypointense structures between gray and white matter (yellow arrows in Fig. 3.11). Furthermore, diffused hyperintense patterns most prominent in adjacent white mattern, co-localized with the U-fiber

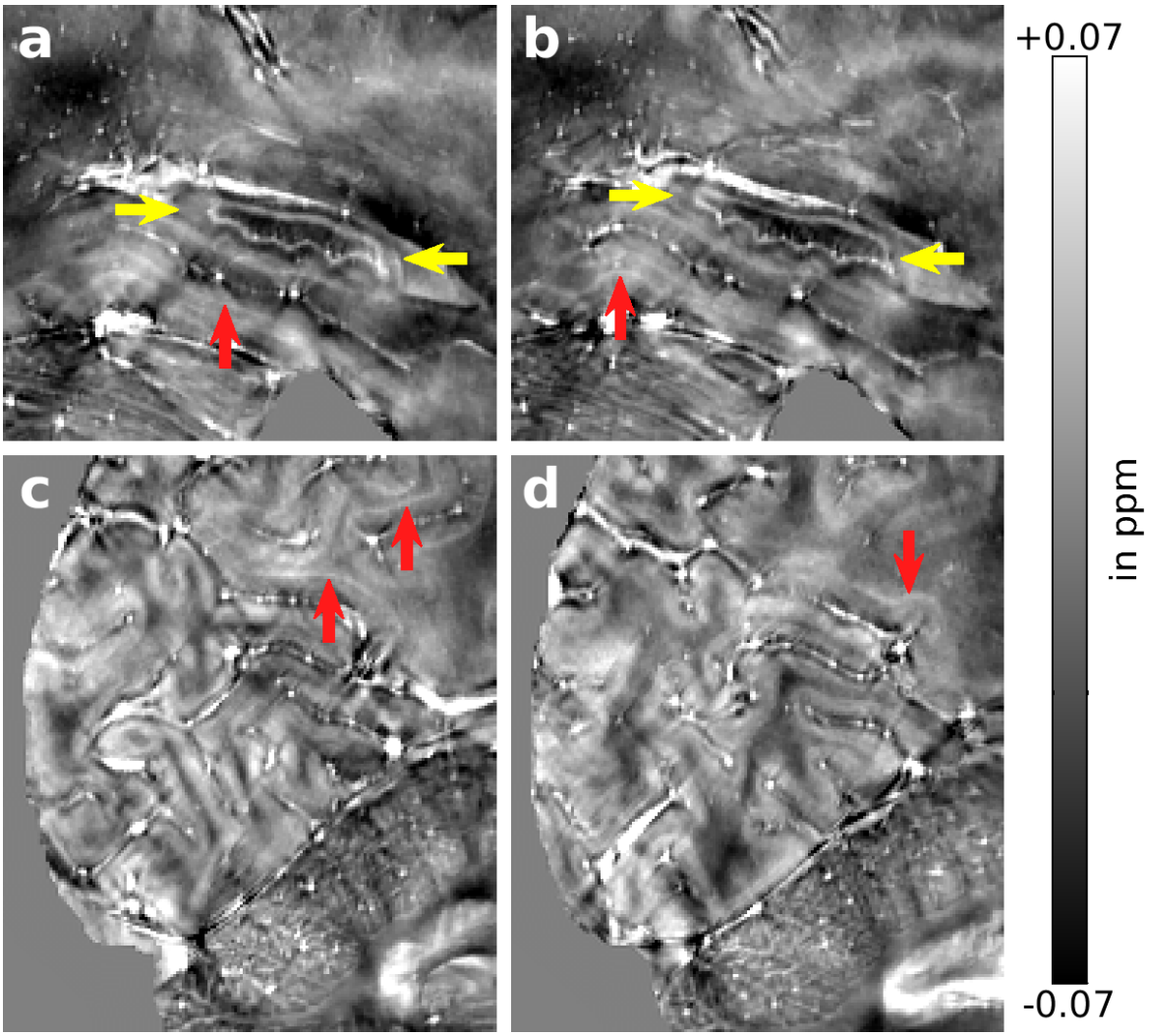


Figure 3.12: Magnified sagittal views of (a, b) the temporal lobe and (c, d) occipital lobe plus cerebellum for motion-corrected QSM at 330 µm isotropic voxel size. Red arrows highlight hyperintense regions between gray matter and adjacent white matter. Yellow arrows show hippocampus.
Quantitative Susceptibility Mapping (QSM).

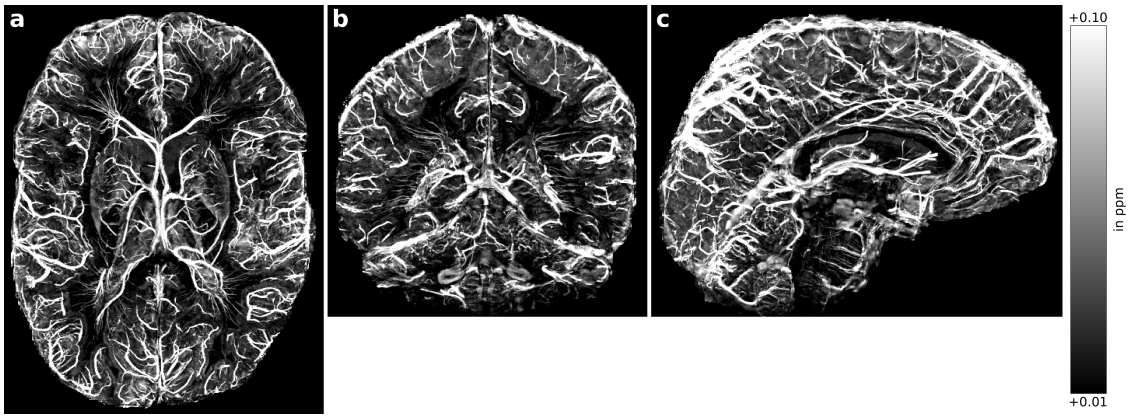


Figure 3.13: (a) Axial, (b) coronal, and (c) sagittal views of motion-corrected, QSM-based venogram at 330 µm isotropic voxel size. Hyperintense veins are enhanced by maximum intensity projection over 45 slices.
Quantitative Susceptibility Mapping (QSM).

layer, can been seen (red arrows in Fig. 3.11). These hyperintense patterns are also visible in sagittal views of occipital and temporal lobes in Fig. 3.12. Also, Fig. 3.12 shows the hippocampus and its digitations (marked with yellow arrows). With PMC, detailed mapping of the venous vasculature was achieved, including clear depiction of the microvasculature in the striatum, thalamus, and brain stem (see Fig. 3.13).

## 3.4 Discussion

In this study PMC was combined for the first time with QSM reconstruction to investigate the potential of high resolution susceptibility maps and venograms at UHF. Qualitatively and quantitatively, PMC reduced artifacts induced by small and large motion. Hence, QSM reconstructed were improved by PMC and enabled in vivo mapping of the human brain macroscopic susceptibilities with up to 330 µm isotropic resolution.

Even when instructed not to move, the subjects in this study — all healthy, young volunteers who routinely participate in MRI-research — moved on average less than 2 mm and 1°. The observed motion was caused mostly by slow head drifts and breathing, thus, unintentional. Nevertheless, motion-induced qualitative and quantitative changes were observed and scaled to some extent with the tracked motion amplitude (see discussion below). Furthermore, subject motion could increase due to anxiety or discomfort in less experienced, but for QSM highly relevant, cohorts (i.e. older subjects or patients with neurodegenerative diseases). Thus, using PMC for QSM of MR-naive subjects could have an even greater potential.

Intra-subject and inter-subject comparisons showed uncorrected motion degraded visually QSM and venograms. While artifacts induced by small-scale motion are less obvious on QSM, these artifacts caused the virtual loss of small-scale structures such as the venous vasculature (see Fig 3.7 and Fig 3.8). With increasing motion amplitude, QSM is degraded considerably (see

subject #4 in Fig 3.7) and venograms are rendered unusable (see subject #4 in Fig 3.8). PMC could reduce motion artifacts clearly, although, minor residuals can occur (further discussed below).

These qualitative observations are in line with the quantitative analyses for intra-subject as well as for inter-subject comparisons. Histogram analysis presented evidence that large amplitude motion causes significant errors in regional susceptibility extractions (see Fig. 3.6 for intra-subject and Fig. 3.9 for inter-subject analysis). For whole-brain and regional susceptibility distributions, an appraent correlation between motion amplitude and KS-test statistic was observed. Changes in deep gray matter susceptibility distributions did not appear to be greater than changes in the cortical distributions. For the intra-subject comparison of data corrupted by intentional versus data corrupted by unintentional motion, PMC reduced systematically KS-test statistics (see Fig. 3.6). Hence, in this single subject analysis motion correction enabled more reproducible susceptibility distributions independent of the motion regime. Furthermore, with increasing spatial resolutions susceptibility distributions become arguably more prone to motion and, therefore, the benefit of PMC should enhance further.

In this study, QSM was reconstructed from prospectively motion-corrected GRE data with 330 µm resolution. Previously, retrospective motion correction was used to acquire GRE data with 350 µm isotropic voxel size, but not susceptibility maps were reconstructed [127]. Another study reconstructed QSM with 400 µm isotropic voxel size, but the GRE data was acquired without motion correction. The potential of PMC and QSM have been successfully combined to decrease the voxel size 1.2-fold (350 µm & no QSM) and 1.8-fold (400 µm & no motion correction), respectively.

The high spatial resolution enabled to depict small brain structures such as the venous vasculature, substantia nigra nigrosome 1, anterior thalamic nucleus, habenula, and digitations of the hippocampus (see Fig. 3.10, Fig. 3.12, and Fig. 3.13). Imaging these small structures is highly relevant. For example, reliable mapping of the nigrosome 1 could enable early detection of neurodegenerative processes or could aid in monitoring therapeutic progress in movement disorders such as Parkisons's disease [59, 142, 143] Furthermore, at such high resolution studying magnetostatic variations across cortex as well as between cortex and subcortical white matter are possible (see Fig. 3.11 and Fig. 3.12). Ultra-high resolution QSM enables mapping of the venous (micro-)vasculature, enabling potentially improved microbleed detection and the study of small vessel diseases. Another use case of motion-corrected venogram could be to mask out draining vessels in high-resolution functional MRI acquired with GRE-based echo planar imaging.

While PMC prevents artifacts caused by head movement by updating the position of the imaging volume, PMC does not account for:

1.) relative motion of the head with respect to receiver profiles,

2.) changes in orientation of the brain with respect to the magnetic field.

Changes in receiver profiles due to motion can be addressed retrospectively [144]. Furthermore, fluctuation in the magnetic field can be corrected by real-time field-control [145] and navigator

scans [146]. PMC cannot correct these magnetic fluctuations and, therefore, the presented results could be biased by potential residual field perturbations. These residuals depend on how the performed head motion changed the alignment of anatomy to static magnetic field, i.e. for large through-plane rotation correcting field fluctuations is expected to be more relevant than for small-scale translation. To acquire and reconstruct QSM free of any erroneous field perturbation motion and field correction should be combined in the future.

PMC inherently does not provide an uncorrected dataset and, therefore, no direct comparison of PMC on and PMC off is possible. Common practice is to repeat (back-to-back) scans with and without PMC to approximate the uncorrected data [12]. However, subject motion is not entirely reproducible. Furthermore, statistical estimates do not weight the motion corresponding to the position in k-space: Movement during acquisition of low frequencies in k-space might have greater impact on image quality than subject motion during encoding of the k-space periphery. Recently, weighted motion estimates have been presented [147, 148] and should be investigated in future PMC–QSM studies. With such metric qualitative ratings, i.e. small versus large motion, might become obsolete.

Simulating motion in QSM could be an alternative approach to overcome the mentioned limitations. The (synthetic) uncorrected, corrected, and ground-truth data could be analyzed for a variety of motion trajectories, which was not possible with the here studied small cohort. However, implementation of such realistic simulation model is challenging.

In conclusion, subject motion impairs QSM reconstructions by reducing the effective resolution and inducing erroneous field perturbations. With PMC this impairment was prevented, reproducibility of regional susceptibility extractions was improved, and detailed depiction of subcortical structures, cortex as well as vasculature was possible with up to 330 µm isotropic voxel size. Therefore, investigating subtle changes in susceptibility and vasculature due to aging or pathologies should be possible with motion-corrected, high resolution QSM in future clinical studies.

# 4 High resolution, motion-corrected ToF angiography

This chapter is based on the previously published paper:

- H. Mattern, A. Sciarra, F. Godenschweger, D. Stucht, F. Lüsebrink, G. Rose, and O. Speck, "Prospective motion correction enables highest resolution time-of-flight angiography at 7T," *Magnetic resonance in medicine*, vol. 80, no. 1, pp. 248–258, 2018

Preliminary results of this study have been presented on conferences:

- H. Mattern, A. Sciarra, F. Godenschweger, D. Stucht, F. Lüsebrink, and O. Speck, "Beyond the biological resolution limit: Prospectively motion corrected Time of Flight angiography at 7T," in *Proc. Intl. Soc. Mag. Reson. Med*, 2017
- H. Mattern, A. Sciarra, F. Godenschweger, D. Stucht, F. Lüsebrink, and O. Speck, "Prospective motion correction for ultra-high resolution Time of Flight angiography at 7T under SAR constraints," in *Proc. Intl. Soc. Mag. Reson. Med*, 2016
- H. Mattern, A. Sciarra, D. Stucht, F. Godenschweger, and O. Speck, "Beyond high resolution: Prospectively motion corrected Time of Flight angiography with 150 µm isotropic resolution at 7T under SAR constraints," in *28rd Annual International Conference of Society of Magnetic Resonance Angiography*, 2016
- H. Mattern, F. Godenschweger, A. Sciarra, D. Stucht, and O. Speck, "Ultra-high resolution Time of Flight angiography at 7T with prospective motion correction under SAR constraints," in *DS-ISMRM2015 - Konferenzband* (DS-ISMRM2015, ed.), 2015

## 4.1 Objective

As outline in the previous section 2.3.2, UHF MRI provides unique potential for high resolution ToF angiography due to intrinsically higher SNR and prolonged $T_1$ relaxation times. With increased resolution, non-invasive ToF angiography could become an alternative to invasive DSA, the current gold standard. However, two challenges prevent utilizing the full potential of high resolution ToF angiography: SAR constrains at UHF and subject motion. SAR constraints prevent the direct application of venous and MT suppression pulses to improve vessel enhancement. Increasing resolution renders MRI more susceptible to subject motion-induced artifacts. Even cooperative, healthy subjects move unintentionally due to breathing and slow head drifts. This inevitable motion is one the order of the imaging voxel size and motion-induced blurring reduces the effective image resolution, creating a so-called biological resolution limit [12]. To overcome these challenges sparse Saturation (sSAT) and PMC were implemented for ToF angiography at 7T. Several SAR management strategies have been reported [102–105] and the approach presented by *Schmitter et al.* [102] was adapted and implemented in this study. Previous studies encourage the application of PMC for high

resolution ToF angiography: At 1.5T, PMC significantly improved the vessel depiction in presence of deliberate head motion [107] and, at 7T, a single subject study without additional saturation enhancement showed the potential of PMC for studying the perforating vasculature in presence of unintentional motion [12]. However, comprehensive study of the biological resolution limit in high resolution ToF angiography remains open. To that end, sSAT and PMC were implemented for high resolution ToF angiography at 7T. Data of eleven cooperative, healthy subject were acquired and motion correction was evaluated qualitatively and quantitatively. To show the potential of PMC to overcome the biological resolution limit, angiograms with up to 150 µm isotropic voxel size have been acquired, resulting in the highest resolution human in vivo ToF angiography to date.

## 4.2 Methods

Table 4.1: Sequence parameters for different acquisitions

| Parameters | Sequence | | |
|---|---|---|---|
| Resolution | 250×250×250 µm$^3$ | 300×300×300 µm$^3$ | 150×150×150 µm$^3$ |
| FOV x,y,z | 196×147×78 mm$^3$ | 216×189×58.5 mm$^3$ | 196×147×46.8 mm$^3$ |
| Slabs | 4 | 4 | 4 |
| Slab encoding matrix | 784×588×96 | 720×630×60 | 1296×972×96 |
| Slab oversampling | 16.7% | 20.0% | 8.3% |
| Slab overlap | -25% | -25% | -25% |
| TR/TE | 50 ms/6.63 ms | 50 ms/6.63 ms | 35 ms/6.63 ms |
| Flip angle | 25 degrees | 25 degrees | 23 degrees |
| Bandwidth | 78 Hz/Px | 78 Hz/Px | 102 Hz/Px |
| Venous saturation | every 10th TR | every 7th TR | every 7th TR |
| GRAPPA factor | 3 | 3 | none |
| Partial Fourier | 6/8 (phase & slice) | 6/8 (phase & slice) | 6/8 (phase & slice) |
| Scan duration | 0:48:05 h | 0:33:08 h | 2:14:21 h |

Field of View (FOV); echo time (TE); repetition time (TR).

### 4.2.1 PMC for ToF angiography

To address the challenge of motion-induced image degradation PMC was applied as described in section 2.4. In short, the MPT system tracked a marker which was rigidly attached to the subject's upper jaw via an individually made mouthpiece. This tracking information was used to correct subject motion prospectively by updating the imaging volume's position and orientation prior to every excitation according to the observed movement.

### 4.2.2 Sparse Saturation

As introduced in section 2.3.2 different approaches can be utilized to meet the increased SAR constraints at UHF [102–105]. A variation the approach presented by Schmitter el al. was implemented here to enable improve venous and background saturation [102].

The vendor-implemented VERSE algorithm was utilized to reduce the peak voltage of the 90° venous saturation pulse by approximately 65% (see section A.1 for further details on VERSE). To that end, the gradient amplitude of the side lobes was set to 250% of the center amplitude and the gradient center length was set to be 40% of the whole gradient length. Furthermore, the venous saturation was applied sparsely (every seventh or tenth TR; see Tab. 4.1). By applying the MT pulses only during the acquisition of the central 10% of the k-space SAR consumption was further reduced. As shown in [102], 10% of the k-space yields the best trade-off between improved background suppression and increased SAR values. All sSAT parameters were constant throughout this study.

### 4.2.3 In vivo measurements

After giving written consent, twelve healthy and complaint subjects participated in this study (approved by local ethics committee). ToF angiography was acquired with a 7 T whole body MRI (Siemens Healthineers, Erlangen, Germany) equipped with a 32-channel head coil (Nova Medical, Wilmington, Massachusetts, USA) at three different resolutions: 300 µm, 250 µm, and 150 µm isotropic voxel size. In Tab. 4.1 all sequence parameters are summarized. TONE pulses with 80% ramp were used for excitation [50]. If sSAT was used, a 40 mm thick venous saturation slab was placed 7 mm above the imaging volume. Partial Fourier was used in all sequences and reconstructed by zero-filling. If required, image acceleration was realized with GRAPPA using 32 auto-calibration lines [154]. To increase reproducibility of subject positioning and minimize motion, pillows were placed in between the head and coil.

#### Protocol for 250 µm isotropic resolution ToF angiography

For a single, healthy subject (male, 34 years), the product sequence (without PMC and without sSAT) was compared to the here implemented sequence (with PMC and with sSAT). Axial MIPs of the acquired data at 250 µm isotropic resolution were assessed qualitatively.

#### Protocol for 300 µm isotropic resolution ToF angiography

ToF angiography at 300 µm isotropic resolution was acquired for eleven, healthy subjects (30.83 ±4.71 years, 4 females) with and without PMC. All subjects were instructed to hold still to investigate the potential of motion correction for high resolution ToF angiography in presence of unintentional motion. Motion-corrected and uncorrected scans were acquired with sSAT. Axial MIPs of all scans were evaluated qualitatively by one experienced MR physicist, stating if image quality with PMC improved, was similar, or degraded compared to the uncorrected

scan of the same subject. Quantitative the axial MIPs were evaluated using the Average Edge Strength (AES) [155]. For each MIP the AES was computed as:

$$\mathrm{AES} = \frac{\sqrt{\sum E(I)[G_x(I)^2 + G_y(I)^2]}}{\sum E(I)}$$

with $\sum E(I)$ as the sum of edges detected in the MIP and $G_{x/y}$ as the gradient image of the MIP along the x- and y-direction, respectively. For each subject, AES was computed for PMC off and PMC on and their relative change reported.

Translational and rotational motion is reported per subject as 3D mean ± standard deviation for PMC on and PMC off. To test if subjects movement differed significantly and to test if motion correction improved significantly the AES paired t-tests were performed (significance level 5%). Data analysis was done with MATLAB 2015b (The MathWorks, Natick, Massachusetts, USA).

### Protocol for 150 µm isotropic resolution ToF angiography

In order to acquire the highest resolution human in vivo brain ToF dataset to date, the subject from the 250 µm session was scanned again at 150 µm isotropic resolution. The high resolution and, therefore, increased number of phase encoding steps resulted in an extended acquisition time. To decrease the scan time, MT pulses were omitted and the number of slices per slab was not increased compared to the 250 µm protocol. As a result, TR was reduced by 15 ms and a lower coverage was achieved. Nevertheless, acquiring one fully sampled volume required more than 2h of scanning. Hence, only a single motion-corrected scan was acquired.

To investigate the effect of imaging resolution on vessel depiction the fully sampled 150 µm dataset was compared to 1.) acquired and 2.) synthesized data with 250 µm resolution. For the first comparison, the following data were compared:

1.) the fully sampled 150 µm dataset
2.) a retrospectively 3-fold undersampled version of the 150 µm dataset
3.) the previously acquired, 3-fold undersampled 250 µm dataset of the same subject
4.) and 150 µm zero-filled version of the 250 µm dataset

An in-house reconstruction pipeline was implemented to perform retrospective undersampling as follows: read in channel-wise raw data (total raw data size >100 GB), store 32 auto-calibration-signal lines per slice, perform 3-fold undersampling in first phase encoding direction, estimate missing k-space by GRAPPA (based on [154], see section A.2 for further details on GRAPPA), do zero-filling to account for partial Fourier acquisition, do channel-wise inverse fast Fourier transform, adaptively combine channels (based on [156]), and merge partially overlapping slabs into final ToF volume.

The 250 µm and 150 µm volumes were acquired in different scan session. Even though the subject was re-positioned carefully, residual misalignment of both datasets was corrected by registering the 250 µm volume to the 150 µm volume using ANTs 2.1 (affine registration with

'antsRegistrationSyN.sh') [136]. Furthermore, the 150 µm data was registered to the 250 µm dataset with the same routine to check for potential bias in the analysis due to interpolation artifacts.

Since interpolation by zero-filling was reported to improve vessel contrast and continuity [157] the 250 µm data was interpolated to 150 µm voxel size. Zero-filling was performed by transforming the images back to k-space, append zeros to the k-space periphery (increase k-space matrix size), and transform the data back to image space.

For the second comparison, first a 250 µm dataset was synthesized from the 150 µm data and then both datasets were compared with each other. Analogous to zero-filling, the 250 µm data was synthesized by transforming the 150 µm data into k-space. Subsequently, the respective high frequency components were set to zero and the data transformed back into image domain, providing images with 150 µm voxel spacing, but containing only measured information for 250 µm resolution.

For both comparisons sagittial MIPs over 60 mm (400 slices) were generated for all datasets For the comparison of measured data additionally axial MIPs over the entire volume and coronal MIPs over 30 mm (200 slices) were created. Vessel-to-background ratios were computed by dividing the mean vessel signal intensity by the mean surrounding background signal intensity and were estimated for the anterior cerebral arteries (ACA), lenticulostriate arteries (LSA), and residual venous blood. All ROIs were manually drawn in the sagitall MIPs. Only vessels visible in the 150 µm and 250 µm data were segmented.

A prospectively motion-corrected MPRAGE [158] was acquired as an anatomical reference for the 150 µm ToF data with the following parameters: 0.45 mm isotropic resolution; 225 x 225 x 187.2 $mm^3$ FOV, TR/TI/TE 2820/1050/2.8 ms, 5° flip angle, bandwidth 170 Hz/Px, 3-fold GRAPPA undersampling with 24 auto-calibration signal lines, 6/8 slice partial Fourier, and an acquisition time of 12:11 min. The bias field corrected MPRAGE (with SPM12 [140]) was registerd to the 150 µm ToF data using FSL FLIRT [159]. 3D volume rendering of the 150 µm data superimposed over the anatomical reference was done with MeVisLab 2.8.2 (MeVis Medical Solutions AG, Bremen, Germany). To extract the arteries from the ToF angiogram in 3D a vesselness filter (Hessian computation with 4 sigmas in the interval of 1 to 5 voxels) was applied.

## 4.3 Results

### 4.3.1 Results for 250 µm isotropic resolution ToF angiography

To evaluate qualitatively PMC and sSAT single subject scans with 250 µm isotropic voxel size were performed. Even when instructed to hold still the healthy subject moved considerably: 7.05 ± 3.03 mm; 1.95 ± 0.85° during PMC & sSAT off; 3.52 ± 1.44 mm; 3.72 ± 0.62° during PMC & sSAT on. Axial MIPs (see Figure 4.1) show that when activated PMC & sSAT improve background tissue and vein suppression, vessel sharpness, vessel continuity, and depiction of

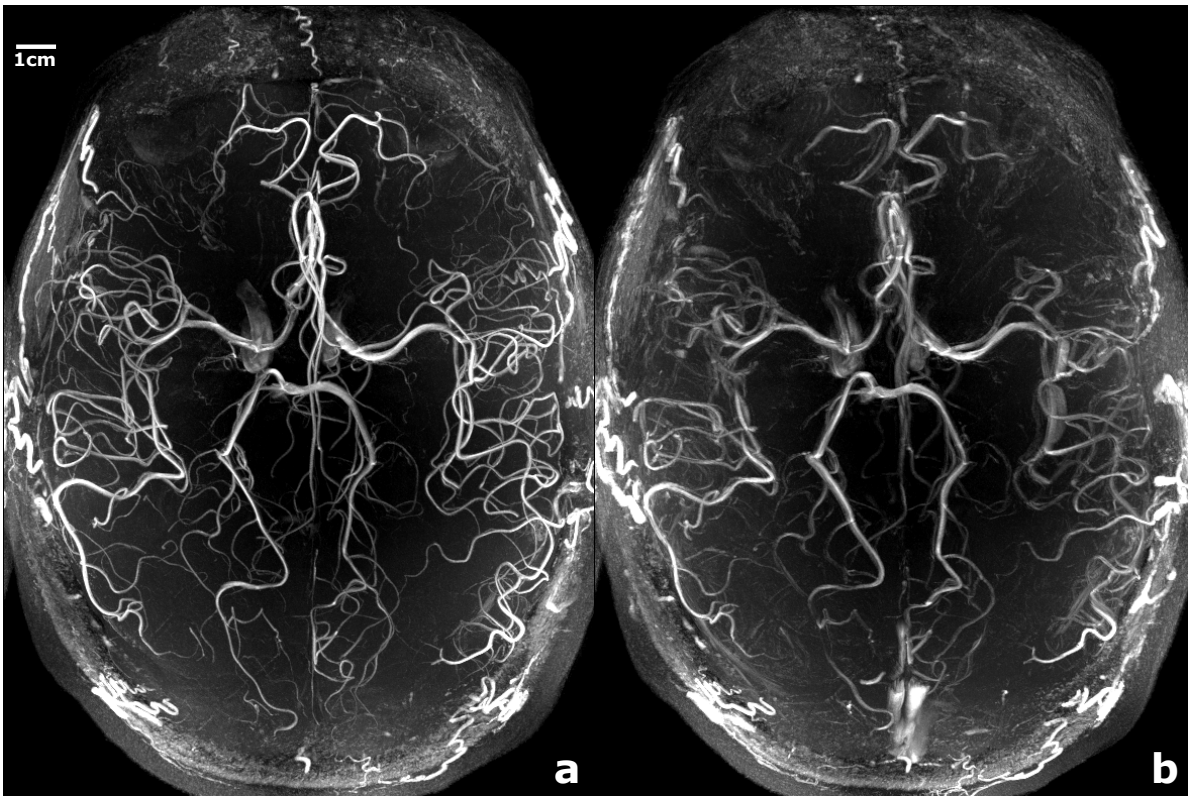


Figure 4.1: MIPs of ToF angiography with 250 µm isotropic voxel size (a) with PMC as well as sSAT and (b) without PMC and no sSAT (MIPs have identical windowing). PMC improved the vessel depiction and sharpness of the MIPs. Venous contamination, such as the superior sagittal sinus, was saturated by sSAT.
Maximum Intensity Projection (MIP); Prospective Motion Correction (PMC); sparse Saturation (sSAT); Time-of-Flight (ToF).

small vessels. Thus, considerably improved artery depiction was achieved with PMC & sSAT in this single subject experiment.

### 4.3.2 Results for 300 µm isotropic resolution ToF angiography

Eleven healthy subjects, which were instructed to hold still, were scanned with and without PMC to study the effect of unintentional motion (sSAT was always applied). For all scans, motion statistics along with the reader rating and AES results are shown in Table 4.2. For individual subjects, motion during corrected and uncorrected scans differs considerably, e.g. subject #3 moved almost one order of magnitude more during the PMC on scan compared to the PMC off one. Computing the mean subject motion for all corrected as well as all uncorrected scans showed no significant difference (p-values of 0.199 for translation and 0.643 for rotation) For all subjects zoomed MIPs with and without PMC are shown in 4.2. If uncorrected, the observed, unintentional subject motion caused blurring of the vessels depicted in MIPs. This could be prevented by PMC, resulting in visually sharper and brighter vessels

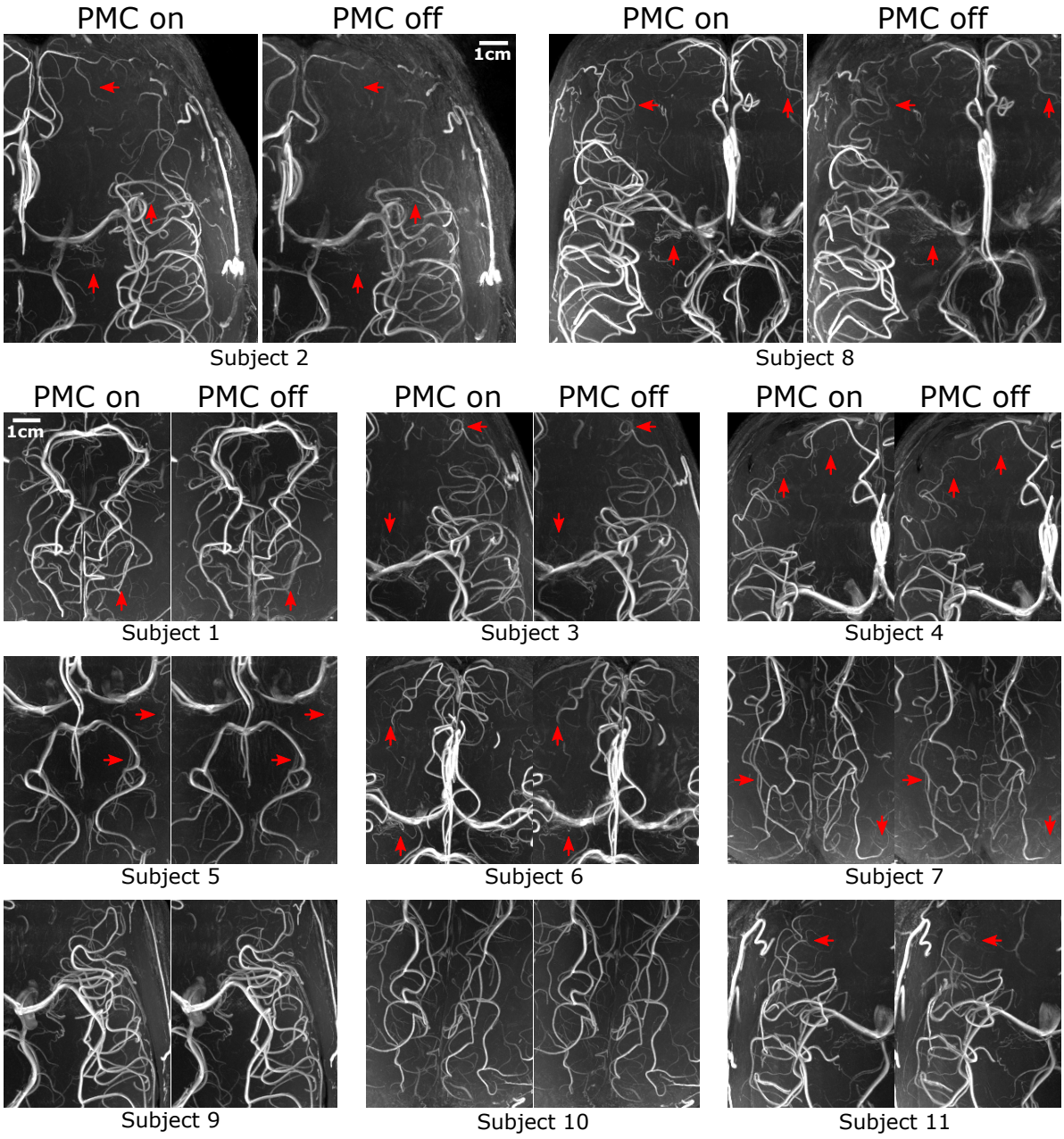


Figure 4.2: Comparison of regional MIPs for eleven subjects with and without PMC in the presence of small-scale, unintentional movements (MIPs have identical windowing). With PMC the vessel depiction qualitatively improves in nine out of eleven cases. Arrows indicate exemplary regions with improved vessel depiction. For subject #9 and #10 the image quality is similar with and without PMC , thus, no arrows are present.
Maximum Intensity Projection (MIP); Prospective Motion Correction (PMC).

Table 4.2: Subject-wise motion quantification and image quality assessment: Mean and standard deviation of the 3D translational and rotational movement is given as well as the AES and reader quality rating with and without PMC.

| Subject | Translational motion [mm] | | Rotational motion [°] | | Change in | Reader quality |
|---|---|---|---|---|---|---|
| | PMC on | PMC off | PMC on | PMC off | AES [%] | rating |
| 1 | 0.96 ± 0.59 | 4.63 ± 1.23 | 0.43 ± 0.1 | 1.79 ± 0.38 | 23.1 | improved |
| 2 | 2.47 ± 1.30 | 2.25 ± 0.90 | 0.77 ± 0.38 | 2.50 ± 0.41 | 47.2 | improved |
| 3 | 12.70 ± 6.25 | 1.63 ± 0.59 | 5.27 ± 1.93 | 0.67 ± 0.20 | 2.2 | improved |
| 4 | 1.40 ± 0.52 | 0.70 ± 0.40 | 0.45 ± 0.15 | 0.47 ± 0.04 | -2.6 | improved |
| 5 | 3.44 ± 0.81 | 1.20 ± 0.56 | 1.66 ± 0.53 | 2.20 ± 0.21 | 53.9 | improved |
| 6 | 1.36 ± 0.82 | 2.47 ± 2.04 | 0.73 ± 0.40 | 1.53 ± 0.68 | 25.0 | improved |
| 7 | 1.73 ± 0.45 | 2.44 ± 0.50 | 0.65 ± 0.15 | 0.53 ± 0.17 | 28.2 | improved |
| 8 | 1.72 ± 0.82 | 0.21 ± 0.42 | 0.65 ± 0.40 | 3.31 ± 0.16 | 47.4 | improved |
| 9 | 3.82 ± 1.65 | 0.66 ± 0.40 | 0.75 ± 0.34 | 1.28 ± 0.12 | -4.5 | similar |
| 10 | 2.32 ± 0.81 | 0.54 ± 0.29 | 0.60 ± 0.15 | 0.59 ± 0.05 | -5.1 | similar |
| 11 | 3.27 ± 1.73 | 1.68 ± 0.45 | 0.95 ± 0.51 | 0.95 ± 0.12 | 4.8 | improved |

Average Edge Strength (AES); Prospective Motion Correction (PMC).

as well as enabling depiction of smaller and more distal vessels. Subjective reader rating followed this observation. In nine out of eleven cases vessel depiction improved with motion correction, while for subject #9 and #10 image quality was similar for PMC on and off. PMC never degraded the vessel depiction in MIPs. Quantitative analysis of the edge strength were concordant with qualitative observations: In eight out of eleven cases motion correction increased the AES, on average AES increased by 18.6 % if PMC was enabled, and paired t-test showed significant differences between AES for PMC on and off ($p = 0.016$).

### 4.3.3 Results for 150 µm isotropic resolution ToF angiography

Table 4.3: Vessel-to-background ratios for the ACA, the LSA, and residual venous blood at different resolutions.

| Volume | Vessel-to-background ratio | | |
|---|---|---|---|
| | ACA | LSA | Veins |
| Fully sampled (150 µm)$^3$ | 4.18 | 2.04 | 1.61 |
| (150 µm)$^3$ with retrospective 3-fold undersampling | 3.59 | 1.66 | 1.48 |
| (250 µm)$^3$ with 3-fold undersampling and zero-filled to (150 µm)$^3$ | 3.46 | 1.69 | 1.45 |
| (250 µm)$^3$ with 3-fold undersampling | 3.46 | 1.65 | 1.45 |
| (250 µm)$^3$ synthesized from (150 µm)$^3$ by setting corresponding high frequency components to zero in k-space | 4.78 | 2.29 | 1.71 |

anterior cerebral arteries (ACA); lenticulostriate arteries (LSA).

To investigate the potential of PMC for high resolution angiography, the subject from the 250 µm scan was measured again with 150 µm isotropic resolution. Due to the very long acquisition time only one motion-corrected volume was acquired, during which the subject moved 2.69

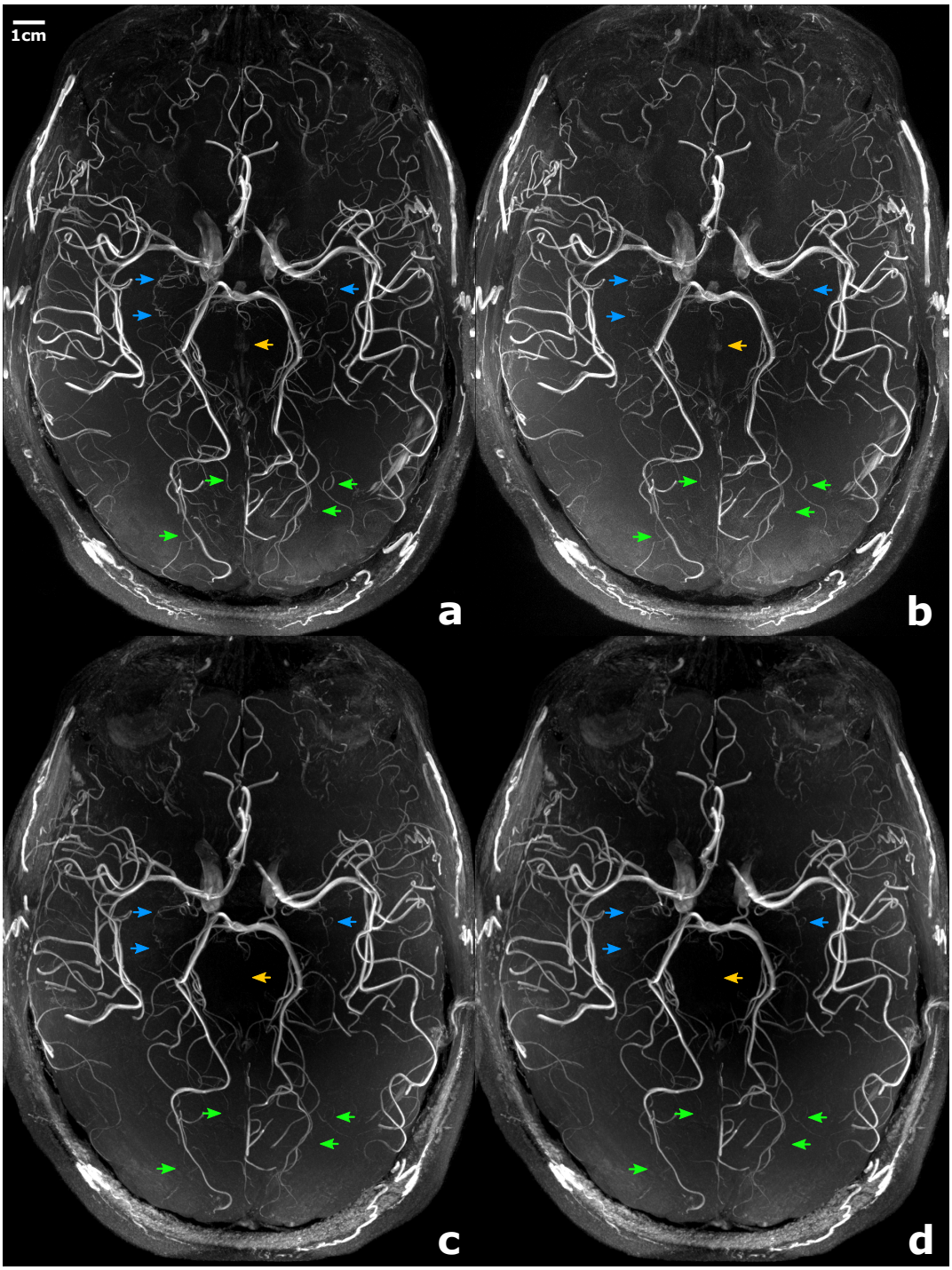


Figure 4.3: Axial MIPs for (a) fully sampled 150 µm , (b) 150 µm with retrospective 3-fold undersampling, (c) 250 µm zero-filled to 150 µm , and (d) 250 µm isotropic voxel size (all reconstructed from motion-corrected scans of the same subject; MIPs have identical windowing). The 250 µm data sets were coregistered to the 150 µm scan prior to the MIP to ensure the same coverage and orientation. Arrows indicate the lenticulostriate arteries (blue), arteries extending towards the occipital lobe (green), and residual venous signal (yellow).
Maximum Intensity Projection (MIP).

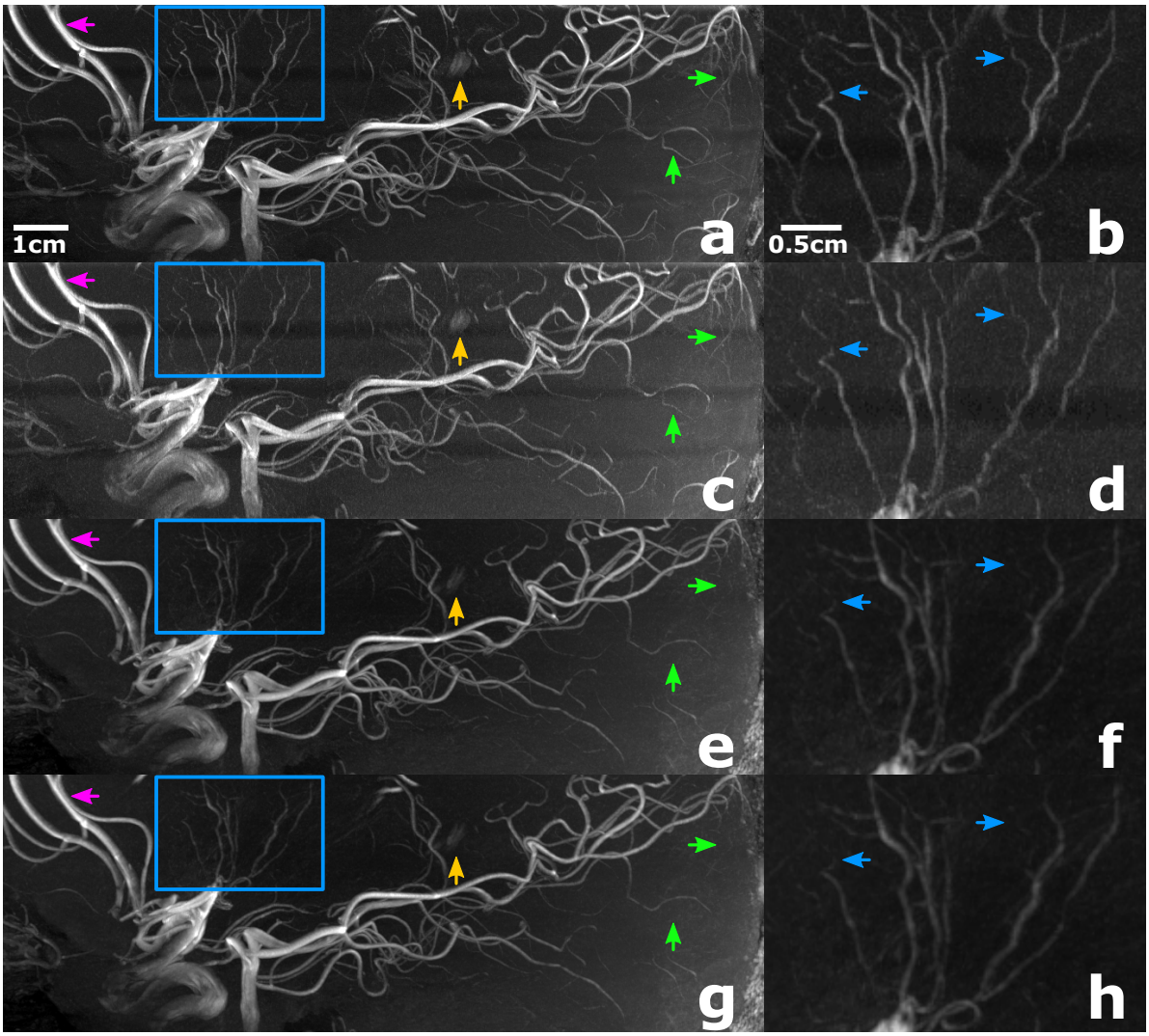


Figure 4.4: Sagittal MIPs (a, c, e, g) and zoomed MIPs of the blue regions (b, d, f, h) for (a, b) fully sampled 150 µm , (c, d) 150 µm with retrospective 3-fold undersampling, (e, f) 250 µm zero-filed to 150 µm , and (g, h) 250 µm isotropic voxel size (all reconstructed from motion-corrected scans of the same subject; MIPs have identical windowing). Arrows indicate the anterior cerebral arteries (pink), the lenticulostriate arteries (blue), arteries extending towards the occipital lobe (green), and residual venous signal (yellow). The 250 µm data sets were coregistered to the 150 µm scan prior to the MIP to ensure the same coverage and orientation.
Maximum Intensity Projection (MIP).

± 1.14 mm and 2.25 ± 0.44°, respectively. Besides the acquired 150 µm (fully sampled) and 250 µm (3-fold undersampled) data sets, the following two data sets were reconstructed retrospectively: 150 µm with 3-fold undersampling and 150 µm reconstruction from 250 µm data set using zero-filled interpolation. All data sets were coregistered to the fully sampled 150 µm data.

Comparison of all data sets yielded superior vessel-to-background ratios (see Tab. 4.1) and vessel depiction (see Fig. 4.3 and Fig. 4.4) for the fully sampled 150 µm data. However, increased vessel-to-background ratios increased also venous contamination in the fully sampled 150 µm data and decreased slab oversampling (to reduce acquisition time) caused residual slab boundary artifacts in both 150 µm volumes. Undersampling increased image noise independent of the resolution. Therefore, with undersampling vessel-to-background ratios decreased by approximately 16% in the ACA, 19% in the LSA, and 9% for residual venous blood compared to the fully sampled data. Even tough, 3-fold undersampling for 150 µm and 250 µm would require approximately the same scan time, the 150 µm provided more than 4-fold decrease in voxel size, 40% less slice coverage, and therefore increased inflow effect due to thinner slabs. This enabled depiction of more LSAs and longer tracking of arteries extending to the occipital lobe in the undersamped 150 µm volume compared to the 250 µm data (see Fig. 4.3 and Fig. 4.4). Thus, to improve small vessel depiction the acquired voxel size, slabs thickness, and acquisition acceleration should be reduced. Applying zero-filling to interpolate the 250 µm data to 150 µm did not increase vessel-to-background ratios, improve vessel continuity, or recover previously not visible vessels.

Due to the extended scan time, 150 µm and 250 µm data had to be acquired in different sessions. To minimize potential bias due to different orientation of anatomy to imaging volume and due to blurring caused by image registration the subject was carefully repositioned in the second session. Image registration estimated the residual difference in head orientation as 4.87° in pitch, 6.12° in roll, and 0.70° in yaw. No bias due to interpolation was found as registration of the fully sampled 150 µm to the zero-filled 250 µm data showed again superior depiction for the higher resolution data as seen before (see Fig. C.1).

To further investigate the effect of imaging resolution on vessel depiction a 250 µm data set was synthesized from the 150 µm data by replacing the measured high frequency components to zero in k-space. Both volumes show similar vessel depiction (see Fig. 4.5 and Fig. C.2). While the vessel sharpness improved visually when using all high frequency components in the 150 µm data, the vessel-to-background ratios (see Tab. 4.3) benefited from the removal of noisy high frequency components in the synthesized 250 µm data (increase of 14% for ACA, 12% for LSA, and 6% for residual venous blood).

Fig. 4.6 further shows the potential of the fully sampled 150 µm data to depict small vessels. The coronal MIP as well as the segmented arteries rendered over a coregistered MPRAGE scan clearly show pontine branches of the basal artery and the LSA. Note that segmentation enables simultaneous 3D rendering of vasculature along with the surrounding anatomical structures, however fails to depict the smallest arteries due to limitations in current

segmentation algorithms.

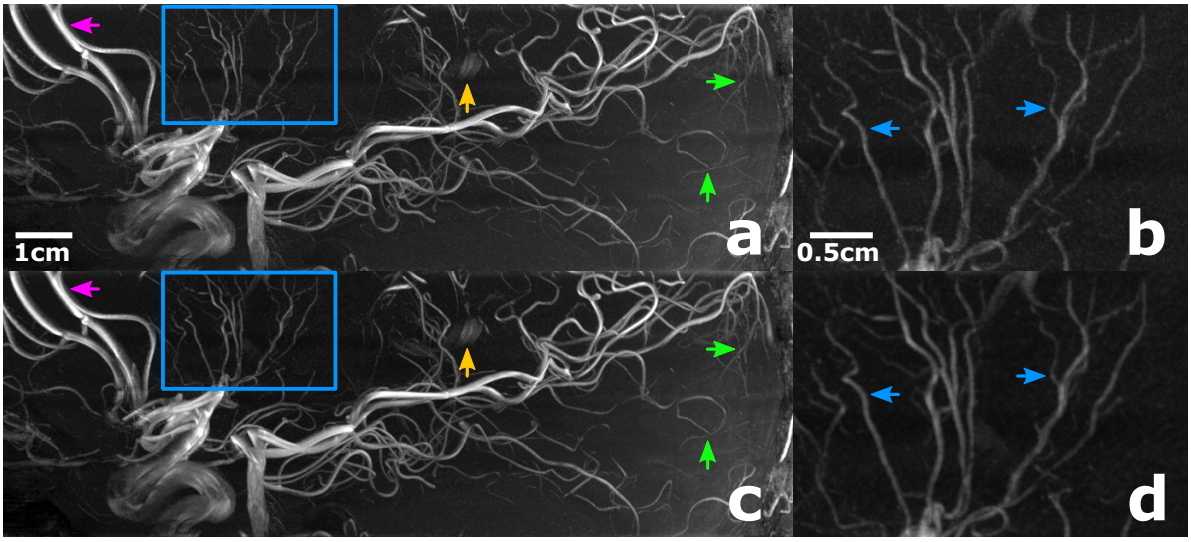


Figure 4.5: Sagittal MIPs (a, c) and zoomed MIPs of the blue regions (b, d) for (a, b) fully sampled 150 µm , and (c, d) 250 µm synthesized from the 150 µm by setting the corresponding high frequency components to zero in k-space (all MIPs have identical windowing). Arrows indicate the anterior cerebral arteries (pink), the lenticulostriate arteries (blue), arteries extending towards the occipital lobe (green), and residual venous signal (yellow).
Maximum Intensity Projection (MIP).

## 4.4 Discussion

In this study PMC and sSAT were combined for the first time to systematically investigate the potential ToF angiography beyond the biological resolution limit. With the implemented sSAT (similar to previously reported approaches [102–105]) venous and background suppression improved while staying within SAR constraints at 7T. PMC improved vessel depiction in 10 out of 12 cases (considering all acquired resolutions) and significantly increased the edge strength of MIPs. Vessel depiction was never compromised with PMC. Furthermore, PMC enabled acquiring the highest resolution human brain in vivo ToF angiography to date.

A single subject was scanned at 250 µm with the original product (sSAT off & PMC off) and modified sequence (sSAT on & PMC on). Even though the subject was instructed not to move during the 50 min scan, motion one order of magnitude larger than the image resolution was recorded. If not corrected, motion-induced image blurring decreased depiction of small vessel (see Fig. 4.1). PMC prevented this loss of detail and, therefore, increased the effective resolution. sSAT improved venous and background suppression (see Fig. 4.1). Saturation of venous blood was applied every 500 ms (every 10th TR), causing effective suppression because the $T_1$ relaxation of venous blood at 7T is approximately 2450 ms [106]. Qualitatively, background suppression and, therefore, vessel-to-background ratios improved with sSAT and

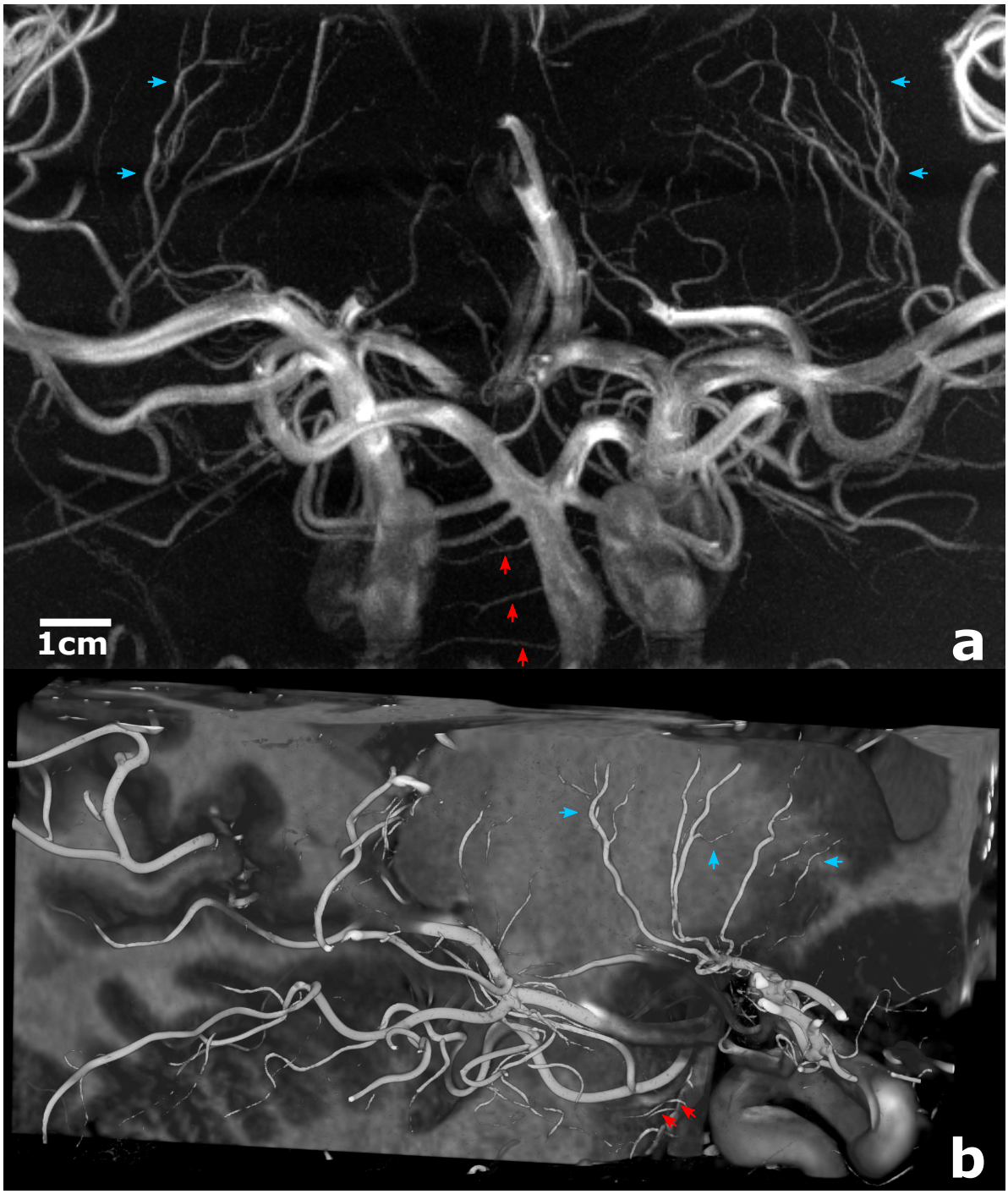


Figure 4.6: Zoomed visualization of the 150 µm isotropic voxel size scan using (a) MIP and (b) 3D volume rendering. The 3D volume rendering features also MPRAGE data to show the anatomical region close to the vessels. The pathways of small vessels like the lenticulostriate arteries into deep gray matter (see blue arrows) and pontine branches of the basal artery to the brain stem (see red arrows) are depicted in detail.
Maximum Intensity Projection (MIP).

PMC. Sparsely applied MT pulses, sharper vessel depiction with PMC, or a combination of both could have caused this improvement. Further investigating the interaction between both, potentially complementary, techniques remains a task to future studies, because this study focuses primarily on the potential of high resolution, motion-corrected ToF angiography. Hence, all following motion-corrected and uncorrected scans were acquired with sSAT.

The eleven subjects scanned with 300 µm isotropic resolution moved unintentionally in the order of a few millimeters/degrees (see Tab. 4.2). Even though large arteries were depicted with and without motion correction, more small and distal arteries were visible with PMC enabled in more than 80 % of the subjects (see Fig. 4.2). Furthermore, the edge strength of MIPs increased significantly with PMC.

Previously, *Kopeinigg et al.* used PMC at 1.5T for ToF angiography and showed that depiction of Circle of Willis arteries in presence of intentional motion improved considerably with motion correction [107]. In contrast, in this study the effect of unintentional motion on imaging small arteries was investigated using approximately 18-times higher resolution (0.502 $mm^3$ vs 0.027 $mm^3$ ). However, *Kopeinigg et al.* reported best vessel depiction if PMC was enabled and the subject instructed to hold still. Thus, unintentional subject motion can degrade ToF angiography at lower resolution as well. Furthermore, in both studies PMC never degraded image quality. Hence, motion correction holds great potential for ToF angiography independent of resolution and motion amplitude.

The potential of the presented sequence enabled the acquisition of the highest resolution human brain in vivo ToF angiography to date. Compared to the previously published data by *Stucht et al.* [12] voxel volume was reduced by 62.5% (0.008 $mm^3$ to 0.003 $mm^3$ ) and the coverage increased by 67.1% (28 mm to 46.8 mm). Even though both data sets were acquired with PMC, only the here presented data used sSAT to suppress veins and saturate static tissue further.

From the fully sampled 150 µm dataset an undersampled version was reconstructed. MIPs for both dataset were compared to the MIPs of the previously acquired 250 µm data of the same subject with and without zero-filling (see Fig. 4.3 and Fig. 4.4). Vessel depiction was superior for the fully sampled 150 µm data. Independent of the resolution, vessel-to-background ratios decreased if undersampling was applied (see Tab. 4.3). Even though identical undersampling factors resulted in similar scan times and vessel-to-background ratios, the undersampled 150 µm data enabled depiction of smaller vessels compared to the 250 µm data. On the one hand the higher imaging resolution, thus reduced partial volume effect, improved the vessel depiction. On the other hand, thinner slabs, motivated by long scan duration, increased the inflow effect. Zero-filling the acquired 250 µm data retrospectively did not improve delineation of small vessels, in contrast to previously reported results [157].

To further investigate the effect of the acquired image resolution on small vessel depiction the high frequency components of the fully sampled 150 µm k-space were zero-filled to synthesize a 250 µm dataset with 150 µm voxel spacing. Therefore, potential bias due to the inflow effect (originating from different slab thicknesses) was avoided. Visual difference between the

fully sampled 150 µm and synthesized 250 µm data are subtle and small vessel delineation is equivalent (see Fig. 4.5 and Fig. C.2). Even though fully sampled data provided visually sharper vessels, the synthesized data showed reduced image noise resulting in increased vessel-to-background ratios (see Tab. 4.3). Acquiring fully sampled data with thin slabs resulted in intrinsically high vessel signals. Retrospective zero-filling of high frequency components did not impair vessel depiction, because the vessel signal remained the dominant signal source within the reconstructed voxel. Eventually, without PMC inevitable subject motion during more than two hours of scanning would have decreased the effective resolution and such detailed vessel depiction would not have been achieved. In summary, small vessel depiction depended in this study on inflow effect, imaging acceleration, imaging resolution, and PMC. While inflow effect and imaging acceleration define the achieved vessel-to-background ratio, imaging resolution and PMC influence the vessel sharpness.

Fig. 4.6 outlines the potential of imaging the perforating vasculature non-invasively at 150 µm isotropic resolution. The applied vesselness filter does not fully detect the smallest vessels compared to the coronal MIP, but provides a 3D rendering of the microvasculature. Improved vessel detection would benefit 3D rendering but also could enable vessel morphology, potentially advancing our understanding of the neurovascular structure—function relationship [160].

Studying the microvasculature of the striatum and hippocampus could enhance the knowledge about neurodegenerative diseases, stroke, and aging, but faces two challenges [9, 10, 92, 94, 97, 161, 162]. First, patients with these pathologies tend to move. Second, high (effective) resolutions are required to detect the microvasculature [6, 7]. Thus, motion correction could overcome these challenges. Another promising application for motion-corrected angiography is functional magnetic resonance angiography [100, 163, 164]. PMC could prevent blurring of the stimuli-induced arterial response and provide reliable activation patterns.

The prolonged scan times limit the more routinely application of the presented approach. With 1D undersampling sufficient vessel-to-background ratios were achieved. Therefore, multi-dimensional image acceleration should be considered, such as 2D GRAPPA, Compressed Sensing (CS) [165], CAIPIRINHA [166], or multiband–multislice imaging [167]. CS seems to be one of the most promising approaches and first implementations for ToF angiography (at clinically used resolutions) have been published [168–171]. Preliminary results of retrospectively applying CS to the here presented high resolution ToF data have been presented at the ISMRM conference [172].

Excessive motion can lead to residual motion artifacts due to gradient and static magnetic field inhomogeneities, relative changes in coil sensitivity profiles, or imperfections in the motion correction system (cross-calibration errors, latency, pseudo motion). In this study, only unintentional, small-scale motion was observed. Therefore, potential bias due to residual artifacts can be considered as neglectable. With less experienced subjects or patients, thus potentially larger motion amplitude, these artifacts could impair image quality, but can be corrected retrospectively [173].

Even though inevitable, small-scale motion was successfully corrected to increase the effective

resolution, non-rigid motion remains uncorrected. The presented PMC system assumes rigid body motion. Hence, pulsation of the vasculature and ventricular system cannot be corrected. CSF pulsations can displace the thalamus up to 100 µm [174]. Therefore, non-rigid motion potentially represent as physiological resolution limit which cannot be overcome with PMC —unlike the biological resolution limit.

In this study, sSAT was realized by applying MT pulses only for the acquisition of the k-space center (10% of k-space) and by applying venous saturation sparsely (every seventh or tenth TR). Additionally, VERSE was applied to the saturation pulse. Overall, effective venous saturation was achieved. However, residual venous contamination was observed in some subjects, potentially originating from subject-specific difference in venous flow velocity. Furthermore, increased vessel-to-background ratios can cause residual venous signal as seen for the fully sampled 150 µm dataset compared to the three undersampled datasets of the same subject (see Tab. 4.3, Fig. 4.3, and Fig. 4.4).

Saturation could be improved further by applying VERSE to the excitation pulse. The available SAR could be used to shorten the TR, apply sSAT more frequent, or increase the excitation flip angle [102, 104]. However, VERSE distorts the excitation profile [102], thus should be applied conservatively for high resolution to prevent image impairment. Shimming the $B_1$ transmit field can improve background, venous, and fat suppression further [175].

With PMC ToF angiography matches the spatial resolution of the gold standard technique DSA. In clinical routine, DSA uses commonly detectors with 1024 $\times$1024 matrix size and $170 - 220$ mm FOV [36, 38, 176], equivalent to e.g. 0.21 $\times$0.21 mm pixel size [36] (note that magnification factors can change the nominal resolution). Thus, the proposed motion-corrected ToF angiography presents a potential alternative to DSA without requiring ionizing radiation, contrast agents, or catheterization. Furthermore, DSA provides only projections of the imaged object while ToF angiography acquires 3D information. The lack of temporal resolution in ToF angiography compared to DSA could be compensated by combining motion-corrected ToF with 4D flow MRA [41, 42] to study the vasculature non-invasively at high spatial and temporal resolutions.

In conclusion, PMC and sSAT were successfully combined to image non-invasively the vasculature beyond the biological resolution limit with improved venous and background suppression at 7 T. As a result the highest resolution human brain in vivo ToF angiography to date was acquired.

# 5 Summary

*"Work it harder, make it better; Do it faster, makes us stronger; More than ever, hour after; Our work is never over"*

— Daft Punk

In the following, the presented studies are summarized and discussed. Subsequently, potentials and challenges are evaluated and future research as well as applications are outlined. Finally, conclusions are drawn.

## 5.1 Discussion

During the course of this thesis, eight papers (two as first author, one as joint fist author) have been published in international journals (MRI, impact factor: 2.564 (2017); MRM, impact factor: 4.082 (2017); Nature Scientific Data, impact factor 5.305 (2017); NeuroImage, impact factor: 5.426 (2017); and Brain, impact factor: 11.814 (2018)). Furthermore, 33 abstracts (14 as first author) and one co-authored conference paper have been accepted by national and international conferences. Three abstracts (all first-authored) have been awarded: Best poster award at the 7th Berlin UHF meeting, summa cum laude merit at the 25th ISMRM, and magma cum laude merit at the 27th ISMRM.

This thesis focuses on the results of combining PMC with QSM and ToF angiography. To that end, two studies were performed and published to evaluate the potential of high resolution, motion-corrected, GRE-based MRI at UHF. To achieve this the following tasks have been performed by the author of this thesis: Sequence programming, PMC integration, study design, data acquisition, image reconstruction, and data analysis.

The first study investigated qualitatively and quantitatively the potential of PMC for QSM. Besides improved reconstruction quality, motion correction could improve reproducibility of susceptibility distributions. QSM holds great promise as a quantitative biomarker, thus, reproducibility is of great concern. Furthermore, susceptibility maps and venograms with up to 330 µm have been acquired. This represents one of the highest resolution QSM dataset to date. At such resolution, PMC prevented motion-induced blurring due to unintentional motion, hence, prevented reduced effective resolution. Furthermore, motion correction enabled reliable depiction of small-scale features such as perforating veins and substantia nigra nigrosome 1.

In the second study, PMC and sSAT were applied to acquire high resolution ToF angiography at UHF with improved vessel depiction and background suppression. Qualitative and quantitative analysis showed motion correction improved arterial vessel delineation and enabled reliable depiction of the perforating vasculature such as the lenticulostriate arteries (LSA). With PMC, the highest resolution, in vivo brain ToF dataset to date was acquired. At 150 µm

isotropic resolution, non-invasive ToF could become a potential alternative invasive DSA.

Both studies showed qualitatively and quantitatively that subject motion can reduce data fidelity. In particular, the depiction of the arterial and venous vasculature was susceptible to motion-induced blurring, but also susceptibility distribution were biased by subject motion.

Except for one experiment in this thesis, all measurements were designed to study the effect of unintentional motion on high resolution MRI. This is in stark contrast to many motion correction studies [107, 112, 120]. At resolutions used in clinical routine, motion correction is commonly applied to prevent rescans due to image degradation induced by large-scale motion. At the high resolutions acquired in this thesis, unintentional, physiological motion is on the order of the voxel size. Therefore, PMC is applied to prevent loss of small-scale image features due to small-scale motion.

### 5.1.1 Imaging beyond the biological resolution limit

In order to depict smaller anatomical features the imaging voxel size is reduced. This renders the image acquisition more susceptible to motion artifacts. At high resolutions, even biological motion such as breathing can induce image blurring which obstructs the detection of small-scale image features. This is the so-called the biological resolution limit [12]. As a result, the effectively acquired resolution is lower than the nominal selected one.

The analysis of 0.33 × 0.33 × 1.25 mm QSM and isotropic 300 µm ToF data showed that healthy and compliant subjects move unintentionally causing image blurring, hence, reduced the effective resolution. PMC prevented this loss in image detail, thus, enabled imaging beyond the biological resolution limit at up to 150 µm isotropic resolution. Arguably without motion correction the effective resolution of such ultra-high resolution scans would have been decreased. Uncorrected data at isotropic resolutions of 330 µm for QSM and and 150 µm for ToF angiography were not acquired because of the long scan times (1.5 to 2h per scan), preventing acquisition of motion-corrected and uncorrected data within the same scan session.

The presented PMC approach assumes rigid body motion, ergo, nonrigid motion cannot be corrected. Pulsation of cerebrospinal fluid were reported to cause shifts in the thalamus of up 100 µm [174]. These nonrigid pulsation could have caused residual blurring in the presented data, eventually creating a *physiological resolution limit*. Systematic analysis of this potential new resolution limit remains a task for future studies.

Furthermore, violations of the rigid body motion assumption can arise from hardware imperfections such as gradient non-linearity, $B_0$ field inhomogeneities, and relative changes in the alignment of anatomy with respect to the receiver sensitivity profiles [3]. The resulting geometric distortions scale with the motion amplitude and can be corrected by iterative solutions [144, 173]. Although these effects could have induced residuals in the presented results their effect is estimated to be small because of small motion trajectories observed.

### 5.1.2 Accelerating high resolution GRE-based imaging

The presented, fully sampled 150 µm ToF data provided sufficient high SNR to apply undersampling techniques to reduce the acquisition time. Great potential of CS for ToF angiography has been shown [168–171], however residual undersampling artifacts commonly blur small-scale image features such as the perforating vasculature. Hence, the effective resolution decreases. To address this challenge one could optimize the undersampling sampling pattern. Modeling the energy in k-space as a probability density and creating pseudo-random based on the density function could improve image quality. A new approach to design pseudo-random sampling patterns from any given density function has been implemented and preliminary results for retrospectively undersampling the here presented ToF data have been presented at the ISMRM by us [172]. Extending the PMC-sSAT-ToF sequence by CS and performing a prospective study to analyze image quality is warrant to prove high resolution microvascular imaging is possible in a timely manner.

For the 330 µm QSM two session with each two averages were necessary to reach sufficient SNR. Thus, equidistant undersampling (i.e. GRAPPA) or pseudo-random undersampling (i.e. CS), which reduce the SNR, are not directly applicable. *Budde et al.* presented a potential solution to reduce scan time for imaging scenarios were a single full k-space acquisition does not provided sufficient SNR and multiple averages are required [177]. Instead of sampling the full k-space multiple time, thus acquiring multiple full averages, k-space segments are acquired more often in the center than in the outer regions of k-space. This average weighting increased SNR by 20% ± 5% compared to conventional full average acquisition for in vivo GRE scans with $0.13\times0.13\times0.8$ mm$^3$ resolution. Since QSM is a post-processing technique based on GRE, implementation of average weighted QSM should be feasible in the future. Furthermore, this concept would be applicable to ToF angiography as well, if even higher resolution require multiple averages to reach sufficient SNR.

In conclusion, time-efficient, high resolution ToF angiography and QSM should be feasible in the future. The main challenge for these GRE-based scans will be to capture the energy distribution in k-space with as few encoding steps as possible while preserving small-scale image features. Hence, optimal sampling strategies for high resolution imaging are required.

### 5.1.3 Improving QSM & ToF acquisition

Besides imaging acceleration, data acquisition with QSM and ToF angiography could be improved further. PMC can not correct motion-induced changes in the magnetic field [178]. For QSM combining PMC with real-time field control could improve susceptibility estimates further [145, 179].

In this thesis ToF angiography and QSM were acquired with dedicated sequences. Both contrasts are GRE-based, hence, could be combined. To that end, multi-echo GRE sequences can be utilized in which angiograms are generated from the first echo and susceptibility maps are derived from the phase evolution across the echoes or venograms are computed with SWI [180–

183]. Even though, this multi-echo approach could enable additionally $T_2^*$ mapping, there are drawbacks compared to acquiring ToF and QSM data individually. Venous saturation cannot be applied, ergo, veins can contaminate angiograms. Furthermore, for QSM acquiring large 3D volumes with the Ernst angle yields optimal SNR, while for ToF angiography multiple thin 3D slabs with spatially varying, high amplitude TONE pulse are beneficial to homogeneously increase arterial signal across the brain. These contradicting imaging concepts render the combination of ToF and QSM non-trivial, especially if small anatomical features are of interest.

QSM and ToF acquisition can be extend to capture temporal information. This has been applied successfully to QSM and ToF angiography to probe brain function [85, 87, 88, 100]. Furthermore, arterial flow can be resolved in the temporal domain by dynamically acquiring ToF data [184], using phase-contrast approaches [185], or spin labeling [186–189]. Although the temporal information can be invaluable in diagnostics and neuroscience, the additional temporal encoding prolongs data acquisition considerably. To enable feasible scan times trade offs between spatial and temporal resolution have to be made. Arguably, the here presented high (spatial) resolution protocols cannot be extend further due to scan time limitations without considerable improved imaging acceleration. Nevertheless, PMC could improve the spatial consistency of temporal phases to enhance spatial and temporal resolution of these prolonged 4D scans.

### 5.1.4 Mapping and quantification of the perforating vasculature

Although vascular imaging in the brain is one of the biggest potentials of UHF MRI [35], a resolution gap between vascular imaging with invasive microscopy and in vivo MRI exists [190]. PMC showed great potential to close this resolution gap, although for routine application accelerating data acquisition of the presented high resolution protocols is required. By combining motion-corrected, high resolution MRI with post-processing such as vessel segmentation, vascular network registration, and feature extraction [86, 160, 191–195], non-invasive vascular mapping at a new spatial scale could be possible. So far, imaging resolution in vasculare mapping [195–197] was insufficient to detect reliably the perforating vasculature [196]. Commonly venous and arterial vasculature are analyzed in separate studies rather than jointly, even though, diseases such as vascular dementia impact arteries [161] and veins [78]. To address these challenges, we performed successfully an initial study at 7T to detect the arterial and venous perforators in deep gray matter [198]. Due to its preliminary nature, the study used an imaging resolution of 0.3×0.3×1.0 mm and no PMC was applied. Although the resolution used is more than a two-fold increase compared to the highest resolution vessel atlas published to date [197], vessel detection should be further enhanced by increasing the nominal and effective resolution through higher resolution, motion-corrected MRI. By closing the resolution gap, new non-invasive application to quantitatively assess and map the vasculature could be established to study the vascular component of pathologies such as multiple sclerosis [9] and neurodegenerative diseases [78, 161, 162, 199].

### 5.1.5 Building an open access, high resolution MRI repository

There is a tremendous interest in open access, high resolution data. Our previously, openly published 250 µm MPRAGE data [13, 14] has been downloaded more than 60,000 times. The here presented highest resolution QSM and ToF data were acquired of the same subject. This unique, highest resolution data set of a single subject enables studying the anatomy and vasculature at previously unperceived resolutions(see conference abstracts [200, 201]) and the here presented QSM and ToF images will be made publically available soon.

## 5.2 Conclusion

In conclusion, successful implementation and evaluation of PMC for GRE-based high resolution MRI at 7T has been shown. PMC enabled image at previously unperceived effective resolutions with down to 150 µm isotropic voxel size. Through imaging acceleration, motion-corrected, high resolution protocols could be applied routinely, potentially closing the resolution gap between microscopy and MRI. Eventually, these high effective resolutions could enhance our knowledge of the human brain's anatomy and vasculature in healthy or diseased, young or old subjects.

# 6 List of own publications

During the course of this thesis the following publications were published:

## Journal publications

1. F. Gretsch*, **H. Mattern***, D. Gallichan, O. Speck;
   *Fat navigators and Moiré phase tracking comparison for motion estimation and retrospective correction*
   Magnetic Resonance in Medicine, 2019
   DOI: 10.1002/mrm.27908
   ***joint first author**
2. M.J. Betts, E. Kirilina, M. Otaduy, D. Ivanov, J. Acosta-Cabronero, M. Callaghan, C. Lambert, A. Cardenas-Blanco, K. Pine, L. Passamonti, C Loane, M.C. Keuken, P. Trujillo, F. Lüsebrink, **H. Mattern**, K. Liu, N. Priovoulos, K. Fließbach, M.J. Dahl, A. Maaß, C.F. Madelung, D. Meder, A.J. Ehrenberg, O. Speck, N. Weiskopf, R. Dolan, B. Inglis, D. Tosun, M. Morawski, F.A. Zucca, H.R. Siebner, M. Mather, K. Uludag, H. Heinsen, B.A. Poser, R. Howard, L. Zecca, J.B. Rowe, L.T. Grinberg, H.I.L. Jacobs, E. Düzel, D. Hämmerer;
   *Locus coeruleus imaging as a biomarker for noradrenergic dysfunction in neurodegenerative diseases*
   Brain, 2019
   DOI: 10.10.1093/brain/awz193
3. **H. Mattern**, A. Sciarra, F. Lüsebrink, J. Acosta-Cabronero, O. Speck;
   *Prospective motion correction improves high resolution quantitative susceptibility mapping at 7T*
   Magnetic Resonance in Medicine, 2018
   DOI: 10.1002/mrm.27509
4. J. Acosta-Cabronero, C. Milovic, **H. Mattern**, C. Tejos, O. Speck, MF. Callaghan
   *A robust multi-scale approach to quantitative susceptibility mapping*
   NeuroImage, 2018
   DOI: 10.1016/j.neuroimage.2018.07.065
5. C. Milovic, J. Acosta-Cabronero, J.M. Pinto, **H. Mattern**, M. Andia, S. Uribe, C. Tejos
   *A new discrete dipole kernel for quantitative susceptibility mapping*
   Magnetic resonance imaging, 2018
   DOI: 10.1016/j.mri.2018.04.004

6. **H. Mattern**, A. Sciarra, F. Godenschweger, D. Stucht, F. Lüsebrink, G. Rose, O. Speck; *Prospective motion correction enables highest resolution time-of-flight angiography at 7T* Magnetic Resonance in Medicine, 2017 DOI: 10.1002/mrm.27033
7. F. Lüsebrink, A. Sciarra, **H. Mattern**, R. Yakupov, O. Speck; *T1-weighted in vivo human whole brain MRI dataset with an ultrahigh isotropic resolution of 250 μm* Scientific Data, 2017 DOI: 10.1038/sdata.2017.32
8. U. Yarach, M.H. In, I. Chatnuntawech, B. Bilgic, F. Godenschweger, **H. Mattern**, A. Sciarra, O. Speck; *A Model-based Iterative Reconstruction for Single-shot EPI at 7T* Magnetic Resonance in Medicine, 2017 DOI: 10.1002/mrm.26633

## Conference papers

1. N. Thoma, R. Odenbach, **H. Mattern**, M. Friebe; *Remotely controllable phantom rotation system for ultra-high field MRI to improve Cross Calibration* Current Directions in Biomedical Engineering, 2019 **accepted**

## Conference abstracts

1. F. Luesebrink, **H. Mattern**, S. Oeltze-Jafra, O. Speck; *Beyond high resolution: Denoising during image reconstruction to improve image quality*; 36th Annual Scientific Meeting of European Society for Magnetic Resonance in Medicine and Biology. ESMRMB, October 2019, Rotterdam; DOI: TBA
2. F. Luesebrink, **H. Mattern**, S. Oeltze-Jafra, O. Speck; *Image reconstruction pipeline*; 36th Annual Scientific Meeting of European Society for Magnetic Resonance in Medicine and Biology. ESMRMB, October 2019, Rotterdam; DOI: TBA
3. N. Thoma, R. Odenbach, **H. Mattern**,M. Friebe; *Remotely controllable phantom rotation system for ultra-high field MRI to improve Cross-Calibration*; 53rd Annual Conference of the German Society for Biomedical Engineering, September 2019, Frankfurt am Main, Germany
4. F. Lüsebrink, **H. Mattern**, S. Oeltze-Jafra, O. Speck; *Denoising during image reconstruction to improve image quality of high resolution MR data*; 3rd Brain in Depth Symposium, April 2019, Leipzig, Germany
5. **H. Mattern**, A. Acosta-Cabronero, O. Speck; *High resolution imaging of the arterial*

*and venous vasculature in deep gray matter*; 27th Annual Meeting of International Society of Magnetic Resonance in Medicine. ISMRM, May 2019, Montreal, Canda

6. F. Gretsch, **H. Mattern**, D. Gallichan, O. Speck; *Direct comparison of fat navigators and Moiré phase tracking for retrospective brain motion correction at 7T*; 27th Annual Meeting of International Society of Magnetic Resonance in Medicine. ISMRM, May 2019, Montreal, Canda
7. A. Cardenas-Blanco, Y. Chen, J.P. Valdes-Herrera, R. Yakupov, **H. Mattern**, A. Sciarra, D. Berron, A. Maass, O. Speck, E Duezel; *Hippocampal subfield segmentation and partial volume effects - reliability assessment*; 27th Annual Meeting of International Society of Magnetic Resonance in Medicine. ISMRM, May 2019, Montreal, Canda
8. **H. Mattern**, O. Speck; *Optimizing Cartesian compressed sensing for ultra-high resolution Time of Flight angiography*; Joint Annual Meeting ISMRM-ESMRMB 2018, June 2018, Paris, France
9. A. Sciarra, **H. Mattern**, O. Speck; *Machine learning algorithms for detection of motion artifacts: a general approach*; Joint Annual Meeting ISMRM-ESMRMB 2018, June 2018, Paris, France
10. **H. Mattern**, R. Odenbach, P. Parsanejad, M. Friebe; *3D-printed MRI marker for personalized interventional applications through T1 and T2 relaxation time matching*; Computer Assisted Radiology and Surgery Congress and Exhibition. CARS, June 2018, Berlin, Germany; DOI:/10.1007/s11548-018-1766-y
11. F. Lüsebrink, **H. Mattern**, O. Speck; *Beyond high resolution: A glimpse into the future*; 2nd Brain in Depth Symposium, May 2018, Magdeburg, Germany
12. F. Lüsebrink, **H. Mattern**, A. Sciarra, R. Yakupov, O. Speck; *Ultrahoch aufgelöster T1-gewichteter in vivo MRT Datensatz des gesamten menschlichen Gehirns*; 20th Annual Meeting German Chapter of International Society of Magnetic Resonance in Medicine, November 2017, Göttingen; ISSN: 1863-6365
13. **H. Mattern**, A. Sciarra, O. Speck; *Non-iterative, retrospective background suppression in time of flight angiography*; 34th Annual Scientific Meeting of European Society for Magnetic Resonance in Medicine and Biology. ESMRMB, October 2017, Barcelona; DOI: 10.1007/s10334-017-0632-1
14. **H. Mattern**, A. Sciarra, O. Speck; *Wavelet entropy: quantifying small-scale head motion artifacts*; 34th Annual Scientific Meeting of European Society for Magnetic Resonance in Medicine and Biology. ESMRMB, October 2017, Barcelona; DOI: 10.1007/s10334-017-0632-1
15. **H. Mattern**, F. Lüsebrink, O. Speck; *Ultrahochaufgelöste MRT des Gehirns mittels prospektiver Bewegungskorrektur*; 52. Jahrestagung der Deutschen Gesellschaft für Neuroradiologie e.V. Neurorad, October 2017, Cologne
16. **H. Mattern**, F. Lüsebrink, A. Sciarra, O. Speck; *More than meets the eye: Quantitative evaluation of prospective motion correction at 7T*; 25th Annual Meeting of International Society of Magnetic Resonance in Medicine. ISMRM, April 2017, Honolulu, USA

17. **H. Mattern**, A. Sciarra, F. Godenschweger, D. Stucht, F. Lüsebrink, O. Speck; *Beyond the biological resolution limit: Prospectively motion corrected Time of Flight angiography at 7T*; 25th Annual Meeting of International Society of Magnetic Resonance in Medicine. ISMRM, April 2017, Honolulu
18. A. Sciarra, **H. Mattern**, R. Yakupov, D. Stucht, P. Schulze, F. Godenschweger, O. Speck; *Quantitative Evaluation of Prospective Motion Correction for Structural Imaging at 7T*; 25th Annual Meeting of International Society of Magnetic Resonance in Medicine. ISMRM, April 2017, Honolulu
19. A. Cardenas-Blanco, D. Berron, Y. Chen, **H. Mattern**, R. Yakupov, A. Sciarra, O. Speck, E. Düzel; *Impact of Prospective Motion Correction in 7T FMRI Studies*; 25th Annual Meeting of International Society of Magnetic Resonance in Medicine. ISMRM, April 2017, Honolulu
20. C. Rua, M.H. In, R. Yakupov, **H. Mattern**, M. Costagli, M. Symms, A. Del Guerra, M. Tosetti, O. Speck; *Study of the PSF Distortion Correction for Ultra-High Field BOLD FMRI*; 25th Annual Meeting of International Society of Magnetic Resonance in Medicine. ISMRM, April 2017, Honolulu
21. F. Lüsebrink, **H. Mattern**, A. Sciarra, O. Speck; *Quantitative and Qualitative Evaluation of Bias Field Correction Methods*; 25th Annual Meeting of International Society of Magnetic Resonance in Medicine. ISMRM, April 2017, Honolulu
22. U. Yarach, **H. Mattern**, O. Speck; *Iterative SENSE with Integrated EPI Nyquist Ghost and Distortion Corrections*; 25th Annual Meeting of International Society of Magnetic Resonance in Medicine. ISMRM, April 2017, Honolulu
23. **H. Mattern**, J. Acosta-Cabronero, A. Sciarra, O. Speck; *Prospectively motion-corrected QSM at 7 Tesla*; 33rd Annual Scientific Meeting of European Society for Magnetic Resonance in Medicine and Biology. ESMRMB, September 2016, Vienna; DOI: 10.1007/s10334-016-0570-3
24. **H. Mattern**, A. Sciarra, F. Godenschweger, D. Stucht, F. Lüsebrink, O. Speck; *Beyond high resolution: Prospectively motion corrected Time of Flight angiography with 150 µm isotropic resolution at 7T under SAR constraints*; 28th Annual International Conference of Society of Magnetic Resonance Angiography. SMRA, September 2016, Chicago
25. **H. Mattern**, J. Acosta-Cabronero, A. Sciarra, O. Speck; *Prospective motion correction for high-resolution QSM*; 4th International Workshop on Quantitative Susceptibility Mapping. September 2016, Graz
26. A. Sciarra, **H. Mattern**, D. Stucht, R. Yakupov, P. Schulze, F. Godenschweger, O. Speck; *Prospective Motion Correction Applications at 7T*; ITN Network HiMR Final Meeting. June 2016, Magdeburg
27. C. Rua, M. Costagli, L. Biagi, M. Symms, M. Cosottini, S. Wastling, G. Barker, M.H. In, R. Yakupov, **H. Mattern**, O. Speck, A. del Guerra, M. Tosetti; *Strategies for high-resolution fMRI at 7 Tesla*; ITN Network HiMR Final Meeting. June 2016, Magdeburg
28. **H. Mattern**, J. Acosta-Cabronero, A. Sciarra, O. Speck; *Prospectively motion corrected*

*QSM-based venograms at 7 Tesla*; 7th Annual Scientific Symposium Ultrahigh Field Magnetic Resonance. June, 2016 Berlin

29. **H. Mattern**, A. Sciarra, F. Godenschweger, D. Stucht, F. Lüsebrink, O. Speck; *Prospective motion correction for ultra-high resolution Time of Flight angiography at 7T under SAR constraints*; 24th Annual Meeting of International Society of Magnetic Resonance in Medicine. ISMRM, May 2016, Singapore
30. F. Lüsebrink, A. Sciarra, **H. Mattern**, R. Yakupov, O. Speck; *Beyond High Resolution MPRAGE: In Vivo T1-Weighted Imaging at 7T with 250 µm Isotropic Resolution Using Prospective Motion Correction*; 24th Annual Meeting of International Society of Magnetic Resonance in Medicine. ISMRM, May 2016, Singapore
31. U. Yarach, **H. Mattern**, A. Sciarra, O. Speck; *Combination of Individual Coil QSM at High Field Strength (7T)*; 24th Annual Meeting of International Society of Magnetic Resonance in Medicine. ISMRM, May 2016, Singapore
32. U. Yarach, D. Stucht, **H. Mattern**, F. Godenschweger, O. Speck; *Gradient Nonlinearity and B0-Induced Distortion Corrections of Prospective Motion Correction Data at 7T MRI*; 24th Annual Meeting of International Society of Magnetic Resonance in Medicine. ISMRM, May 2016, Singapore
33. **H. Mattern**, F. Godenschweger, A. Sciarra, D. Stucht, O. Speck; *Ultra-high resolution Time of Flight angiography at 7T with prospective motion correction under SAR constraints*; 18th Annual Meeting German Chapter of International Society of Magnetic Resonance in Medicine. DS-ISMRM, November 2015, Münster; ISSN: 1863-6365

# A Extended background

## A.1 VERSE

Variable-Rate Selective Excitation (VERSE) is a pulse refabrication technique introduced by *Conolly et al.*. It takes a previously designed RF-pulse as input and computes a new pulse form and corresponding time-varying gradient waveform. The new pulse produces the same flip angle as the input pulse and is therefore called a *facsimile pulse*. Based on their publication [101], a summary of using VERSE to reduce SAR of RF-pulses will be given.

### A.1.1 Principles of VERSE

VERSE is based on the Larmor relation (see Eq. 2.2): The precession frequency of a spin ensemble is determined by the applied magnetic field. Assuming a piece-wise constant RF-pulse, the excitation can be decomposed into $N$ rectangular sub-pulses, each with the duration $\Delta t$. During each sub-pulse $j = 1..N$, a magnetization vector precesses with an angle $\theta = \omega\Delta t$, thus, the angle is the product of frequency and duration. For the entire excitation, the net rotation of all sub-pulses is critical rather than the rate of rotation. Hence, the same flip angle could be achieved by exciting the spins twice as long with half of the applied field. This is true for the entire pulse, but also for each sub-pulse. By altering each sub-pulse individually rather than all of them uniformly, one can change the RF-pulse while maintaining the same excitation profile.

This concept can be express mathematically. The piece-wise constant, complex RF pulse is represented by $B_1(j) = B_I(j) + iB_Q(j)$ and its corresponding uniform gradient by $G$. Assuming negligible relaxation, the Bloch equations for excitation yield a magnetization vector at time $T = N\Delta t$:

$$M(z,T) = \prod_{i=N}^{1} \exp\left(\begin{bmatrix} 0 & G_z & -B_Q(j) \\ -G_z & 0 & B_I(j) \\ B_Q(j) & -B_I(j) & 0 \end{bmatrix} \gamma\Delta t\right) M(z,0) \tag{A.1}$$

Thus, the magnetization vector is the ordered product of all rotation matrices multiplied by the initial magnetization distribution. Introducing an excitation amplitude-reduction factor $\alpha(j)$, the duration of the $j$th subpulse is altered by $\Delta t/\alpha(j)$, while the excitation fields are multiplied by the same factor $\alpha(j)$:

$$\exp\left(\begin{bmatrix} 0 & \alpha(j)G_z & -\alpha(j)B_Q(j) \\ -\alpha(j)G_z & 0 & \alpha(j)B_I(j) \\ \alpha(j)B_Q(j) & -\alpha(j)B_I(j) & 0 \end{bmatrix} \frac{\gamma\Delta t}{\alpha(j)}\right) \tag{A.2}$$

Therefore, if a sub-pulse is shortened due to the amplitude-reduction factor, the excitation

fields are increased proportionally, and vice versa. Hence, each sub-pulse results in the same rotation as before, but a new degree of freedom is introduced in form of $\alpha(j)$ and the resulting time-varying gradient waveform $\alpha(j)G$.

The resulting set of pulse waveforms are defined as $b_1(j) = \alpha(j)B_1(j)$ and $g(j) = \alpha(j)G$. As they perform the same function as the original waveforms, they are called facsimile pulses. With $t(j) = \Delta t/\alpha(j)$, the facsimile conditions can be summarized as:

$$\begin{bmatrix} b_I(j) \\ b_Q(j) \\ g(j) \end{bmatrix} t(j) = \begin{bmatrix} B_I(j) \\ B_Q(j) \\ G \end{bmatrix} \Delta t \tag{A.3}$$

The VERSE principle can be used to address a variety of problems such as the reduction of SAR (see following section) and shortening of pulse duration [202].

### A.1.2 SAR reduction with VERSE

The energy deposited in the subject by the pulse is proportional to the integral of the squared RF-magnitude. Therefore, SAR for the VERSE RF-pulse $b_1$ is:

$$\mathrm{SAR} \propto \int_0^T |b_1(t)|^2 dt \tag{A.4}$$

For a piece-wise constant pulse, Eq. A.4 can be reformulated as:

$$\mathrm{SAR} \propto \sum_{j=1}^{N} |b_1(j)|^2 t(j) \tag{A.5}$$

Using the facsimile conditions in Eq. A.3, the SAR of the VERSE pulse can be computed from the original pulse $B_1$ and the VERSE reduction function $t(j)$ or gradient waveform $g(j)$:

$$\mathrm{SAR}(\mathbf{t}) \propto \sum_{j=1}^{N} \frac{|B_1(j)|^2}{t(j)} \tag{A.6}$$

$$\mathrm{SAR}(\mathbf{g}) \propto \sum_{j=1}^{N} |B_1(j)|^2 g(j) \tag{A.7}$$

with $\mathbf{t}$ and $\mathbf{g}$ as the vectors with elements $t(j)$ and $g(j)$.

This formulation has three advantages. First, the SAR equation can be expressed as a function of either $t(j)$ or $g(j)$. Second, if one VERSE function is known, the remaining waveforms can be derived from it. Thus, a single function is enough to fully describe the

problem. Third, one can use Eq. A.6 and Eq. A.7 as cost functions in a minimization problem:

$$\min_{\mathrm{g}} \mathrm{SAR}(\mathbf{g}) = \sum_{j=1}^{N} |B_1(j)|^2 g(j) \tag{A.8}$$

subject to

$$\sum_{j=1}^{N} t(j) = N\Delta t \tag{A.9}$$

$$g(j) < G_{max} \tag{A.10}$$

VERSE can solve this SAR minimization problem using *two-speed* facsimile pulses, although more elaborate implementations are possible. The user specifies the VERSE gradient waveform by selecting the gradient amplitude of the side lobes with respect to the center amplitude and by choosing the length of the gradient center with respect to the whole gradient duration. As a result, the center of the RF-waveform, where most RF-pulses are very peaked, is flattened, while the side lobes are amplified. This redistribution in pulse area enables decreased SAR while maintaining the same flip angle and slice profile (neglecting off-resonance effects).

## A.2 GRAPPA

MRI is an inherently slow imaging modality, which is one of the reason for its susceptibility to subject motion. To accelerate data acquisition in MRI, and therefore reduce the scan duration, parallel imaging has been introduced [203]. The fundamental idea is to uniformly undersample k-space, ergo, acquire only every $A$th phase encoding step. From Eq. 2.13, one can derive that the encoded FOV in image space is determined by the sampling density in k-space:

$$\mathrm{FOV} = 1/\Delta k \tag{A.11}$$

Thus, omitting every $A$th encoding step reduces the FOV by a factor $A$, but also reduces acquisition time by the same factor [204]. Therefore, $A$ is referred to as the *acceleration factor*. Excited tissue from outside the FOV (reduced by factor $A$) will cause aliasing in form of *wrap-around* artifacts. To recover the unwrapped image, one can use multiple receiver coils place around the imaged object. Several methods have been introduced to implement parallel imaging in MRI and are compared elsewhere [203]. In this thesis, GeneRalized Autocalibrating Partial Parallel Acquisition (GRAPPA) was used, a self-calibrated reconstruction technique which interpolates the not acquired data in k-space. The main idea is that the missing phase-encoding steps can be generated from linear combinations of the acquired, multi-coil data, rather than using magnetic field gradients [203]. This is possible because the sensitivity profile of each coil is spatially varying, i.e. excited spin ensembles close to the coil result in high signal in the coil, while with increasing distance to the coil the detected signal vanishes. Hence, coil sensitivity profiles inherently spatially encode the data they receive. By placing

multiple coils around the imaged volume, their sensitivity profiles allow to recover data from missing spatial encoding steps. Without loss of generality, undersampling in a single phase encoding direction $k_y$ is considered in the following. The introduced concepts can be extended to multi-directional undersampling.

GRAPPA reconstructs the data in coil $j$ at the not acquired line $S_j(k_y - m\Delta k_y)$ using a block-wise reconstruction [154]:

$$S_j(k_y - m\Delta k_y) = \sum_{l=1}^{L} \sum_{b=0}^{N_b-1} n(j,b,l,m) S_j(k_y - bA\Delta k_y) \tag{A.12}$$

with:

- $\Delta k_y = 2\pi/\text{FOV}$
- $j$ as the $j$th coil in the array of $L$ coils
- $l$ as index counting through all $L$ coils, thus, data from all coils is used to reconstruct data in an individual coil
- $A$ as the acceleration factor, thus, only every $A$th line is acquired
- $m$ as the order of the spatial harmonic to be reconstructed, $m = 1..A-1$
- $b$ as the current reconstruction block, $b = 1..N_n$ with $N_b$ as the number of blocks. A block is defined as a single acquired line and $A-1$ not acquired lines.
- $n(j,b,l,m)$ as the weights to interpolate the missing line using linear combinations of the acquired, undersampled data $S_j(k_y - bA\Delta k_y)$

Therefore, the left side of Eq. A.12 represents the missing data at the k-space position $(k_y - m\Delta k_y)$. This missing information $S_j(k_y - m\Delta k_y)$ is reconstructed using linear combinations $n(j,b,l,m)$ of the acquired data $S_j(k_y - bA\Delta k_y)$ (right side of Eq. A.12).

Reconstruction is performed for each coil individually and, therefore, $L$ uncombined k-spaces are provided. After applying the inverse Fourier transform, the coil-wise image volumes can be combined with techniques such as root sum-of-squares or adaptive combine [156].

GRAPPA is a self-calibrated technique, thus, it estimates the weights $n(j,b,l,m)$ from the so-called *auto-calibration-signals* and does not require prior knowledge of the receiver sensitivity profiles. These auto-calibration-signals are additional lines acquired around the k-space center. Hence, the k-space center is fully sampled and used to fit the weights required to interpolate the missing, undersampled data. The size of this calibration region is specified by the user and is a trade-off between scan time reduction and reconstruction quality. Note that the additional acquired auto-calibration-lines can be inserted in the final reconstructed k-space to improve the reconstruction further [154, 203].

The process of fitting the weights can be formulated for each coil $j$ and block $b$ as [154, 203]:

$$S_j^{ACS}(k_y - m\Delta k_y) \cong \sum_{l=1}^{L} n(j,b,l,m) S_j(k_y) \tag{A.13}$$

with $S_j^{ACS}(k_y - m\Delta k_y)$ as the additionally acquired auto-calibration-signal. Note that for

calibrating the weights of a single coil, all available coils are considered. The fitting process in Eq. A.13 is similar to the reconstruction in Eq. A.12. The main differences are the given data and unknowns. During the fitting process, the weights are calibrated based on the additionally available signals $S_j^{ACS}$ at the lines $(k_y - m\Delta k_y)$. In the reconstruction, these weights are then used to produce the missing lines as linear combinations of the acquired data.

## A.3 QSM processing

Following Eq. 2.23, the local field variations $\Delta B_z(\mathbf{k})$ can be computed as a voxel-wise multiplication of the dipole kernel $G(\mathbf{k})$ with the susceptibility distribution $\chi(\mathbf{k})$ in k-space. Equivalently, a convolution of the dipole kernel $G(\mathbf{r})$ with the tissue susceptibility $\chi(\mathbf{r})$ in image space yields $\Delta B_z(\mathbf{r})$. The susceptibility-induced field perturbations $\Delta B_z(\mathbf{r})$ cause phase changes $\Delta\phi(\mathbf{r})$ in the measured GRE data, as formulated in Eq. 2.24. The goal of QSM is to solve Eq. 2.24 and extract the underlying susceptibility distribution $\chi(\mathbf{r})$ for the induced phase changes $\Delta\phi(\mathbf{r})$ [64]. In the following, background field removal and dipole inversion techniques are explained.

### A.3.1 Background field removal in QSM

Reliable phase information is usually only available within a limited ROI [64]. In neuroscientific applications, QSM is commonly limited to the brain tissue. Due to the non-local nature of the dipole kernel, susceptibility sources from outside the ROI, i.e. air cavities and the skull, have a significant impact on the phase measured within the ROI. To remove susceptibility changes induced by sources from outside the ROI, the field perturbations $\Delta B_z(\mathbf{r})$ are decomposed into internal $B_{int}(\mathbf{r})$ and background $B_{bck}(\mathbf{r})$ contributions [64]:

$$\Delta B_z(\mathbf{r}) = B_{int}(\mathbf{r}) + B_{bck}(\mathbf{r}) \tag{A.14}$$

Within the ROI, $B_{bck}(\mathbf{r})$ is harmonic as its sources are located outside the ROI by definition [26, 64]. Harmonic functions satisfy Laplace's equation [64]:

$$\nabla^2 B_{bck}(\mathbf{r}) = 0 \tag{A.15}$$

with the three-dimensional Laplace operator $\nabla^2 = \frac{\partial^2}{\partial x^2} + \frac{\partial^2}{\partial y^2} + \frac{\partial^2}{\partial z^2}$.

$B_{int}(\mathbf{r})$ is not harmonic within the ROI and therefore it can be extracted from the field perturbations with [26, 64]:

$$\nabla^2 \Delta B_z(\mathbf{r}) = \nabla^2 (B_{int}(\mathbf{r}) + B_{bck}(\mathbf{r})) = \nabla^2 B_{int}(\mathbf{r}) \tag{A.16}$$

Note that these equations are only valid within the ROI. Motivated by Eq. A.16, several approaches have been introduced to remove the background field and are reviewed elsewhere [26]. In the following, the background removal techniques used in this thesis — SMV and HARPERELLA — are summarized.

### SMV

To solve Eq. A.16, the Spherical Mean Value (SMV) property of harmonic functions can be utilized [26, 32, 64]. The SMV is the mean value of a harmonic function $u(\mathbf{r})$ calculated over a sphere centered at $\mathbf{r}_0$ and it is equal to the value of the harmonic function at the center of the sphere $u(\mathbf{r}_0)$ [26, 64]:

$$\int u(\mathbf{r}) S(\mathbf{r} - \mathbf{r}_0)\, d^3\mathbf{r} = u(\mathbf{r}_0) \tag{A.17}$$

with $S(\mathbf{r})$ as a spatially restricted, normalized sphere ($\int S(\mathbf{r})\, d^3\mathbf{r} = 1$). Note that Eq. A.17 represents a convolution and can also be expressed as $u * S = u$ [26]. Hence, the SMV of the harmonic background field yields $B_{bck} * S = B_{bck}$. Applying the SMV to the field perturbations inside the ROI can be described [26, 64]:

$$\begin{aligned}
\Delta\hat{B}_z &= \Delta B_z - \Delta B_z * S && \text{(A.18)}\\
&= B_{int} + B_{bck} - (B_{int} * S + B_{bck} * S) && \text{(A.19)}\\
&= B_{int} + B_{bck} - B_{int} * S - B_{bck} && \text{(A.20)}\\
&= B_{int} - B_{int} * S && \text{(A.21)}
\end{aligned}$$

The interim field $\Delta\hat{B}_z$ depends only on the internal field component and the SMV kernel [64]. With $\delta$ as the Dirac impulse at the center of the sphere, one can rewrite Eq. A.21 as [64]:

$$\Delta\hat{B}_z = (\delta - S) * B_{int}. \tag{A.22}$$

Hence, the internal field can be estimated from the interim field by deconvolution ($*^{-1}$) [64]:

$$B_{int} = (\delta - S) *^{-1} \Delta\hat{B}_z \tag{A.23}$$

As a reminder, these equations are only valid within the ROI because the background field induced by sources from outside the ROI is assumed to be harmonic. The ROI — in which the Laplacian can be evaluated — can be defined by a Mask $M$ which is one for voxels within the ROI and zero otherwise. Due to the spatial extend of the sphere $S$, Eq. A.23 cannot be evaluated for all voxels segmented by the mask $M$ because the kernel would exceed the mask for voxels on the ROI boundary. Therefore, a second mask $\hat{M}$ is introduced which is an eroded version of $M$. The amount of erosion scales with the sphere radius. By including the mask $\hat{M}$, Eq. A.21 and A.22 can be combined as [26]:

$$\hat{M}(\hat{S} * \Delta B_z)(\mathbf{r}) = (\hat{S} * B_{int})(\mathbf{r}),\ \forall \mathbf{r} \in \hat{M} \tag{A.24}$$

with $\hat{S} = \delta - S$.

This background field filtering approach is commonly referred to as Sophisticated Harmonic Artifact Reduction for Phase (SHARP) [64]. By implementing SHARP in Fourier domain, con-

volutions in the spatial domain are transformed into point-wise multiplications and background field removal can be performed efficiently (following [32]):

1. Compute the Fourier transform of the phase data
2. Apply SMV filter to remove background field contributions
3. Perform the deconvolution step to estimate the internal field
4. Apply the inverse Fourier transform to get the internal field information in the image domain

Due to the limited spatial extent of the ROI, a key parameter for SHARP is the spatial extent of the filter kernel $S$ (sphere radius) itself. If large radii are used, field information at the boundary of the ROI is lost due to erosion ($S$ cannot be evaluated close to the boundary, as the sphere would exceed the ROI). If small radii are used, boundary-related artifacts in the internal field occur. For in-depth discussion the interested reader is referred to [26]. Variable-radius Sophisticated Harmonic Artifact Reduction for Phase (VSHARP) attempts to overcome this challenge by varying the kernel radius [205]. A large sphere radius is used in the ROI center and with increasing distance from the center the kernel radius decreases.

#### HARPERELLA

Although VSHARP addresses the challenge of mask erosion and insufficient background field removal by varying the filter kernel size, phase information cannot be evaluated in the boundary region of the mask. Thus, the effective ROI (descibed by $\hat{M}$) after applying SHARP is always smaller than the full brain mask $M$. To overcome this HARmonic (background) PhasE REmovaL using the LAplacian operator (HARPERELLA) can be used. Similar to Eq. A.24, the harmonic relation in Eq. A.16 can be restricted to a certain ROI by masking *both sides* of the equation [26]:

$$M\nabla^2\Delta B_z(\mathbf{r}) = M\nabla^2 B_{int}(\mathbf{r}),\ \forall \mathbf{r} \in M \tag{A.25}$$

Note that the mask $M$, and not its eroded version $\hat{M}$, is used. This enables to recover $\Delta B_z$ in the mask boundary $M - \hat{M}$ [25].

By applying masks on both sides of the equation the associated system becomes underdetermined, hence, having multiple solutions. To address this challenge, HARPERELLA enforces a minimum-norm on the Laplacian $L$ [26, 138]:

$$\begin{aligned} L_{min} &= \arg\min_{L} \|L\|_2^2 \\ \text{subject to } & M\nabla^2\Delta B_z = ML \end{aligned} \tag{A.26}$$

This equation can be solved by convolution with a filter, such as the SMV kernel $S$, and can

be written in a Lagrangian form [26, 138]:

$$L_{min} = \arg\min_{L} \|S * (M\nabla^2\Delta B_z + (1-M)L)\|_2^2 \tag{A.27}$$

Searching for the minimum norm requires an iterative solution, thus, HARPERELLA requires the user to define the number of iterations. Furthermore, HARPERELLA removes phase wraps and background field, ergo, background phase component, in a single procedure as it derives the Laplacian of the phase $\phi$ from sine and cosine functions as [23, 138]:

$$\nabla^2\phi = \cos\phi\nabla^2\sin\phi - \sin\phi\nabla^2\cos\phi \tag{A.28}$$

Therefore, with HARPERELLA no additional phase unwrapping is required in the QSM pipeline.

### A.3.2 Dipole inversion with MEDI & nMEDI

After removing the background field contributions, the underlying tissue susceptibility can be recovered from the local field by dipole inversion. As seen in Eq. 2.22, this field-to-susceptibility inversion is an ill-conditioned problem due to discontinuities in the dipole kernel (values equal or close to zero at the magic angle of 54.7° in the k-space) [21, 30]. Without addressing this challenge, direct inversion could cause severe noise amplification and streaking artifacts [30]. By measuring the object in multiple orientations with respect to $B_0$ the discontinuities can be recovered, but this is approach is not practical as it requires multiple GRE measurements and the subject to rotate the head into certain positions [29]. For single measurements, regularisation can be used to reduce artifacts in dipole inversion. In this thesis, regularized dipole inversion is performed by a technique called morphology-enabled dipole inversion (MEDI). MEDI takes advantage of the available magnitude data from the GRE scan by assuming that edges in the magnitude images correspond to edges in the susceptibility map [21]. This anatomical prior is enforced by $L_1$ regularization in the MEDI dipole inversion which can be formulated as a minimization problem [21, 30]:

$$\begin{aligned} \chi_{min} &= \arg\min_{\chi} \|M_D\nabla\chi\|_1 \\ &\text{subject to } \|W(B_{int} - F_G\,\chi)\|_2 = \epsilon \end{aligned} \tag{A.29}$$

with:

- $\chi_{min}$ as the solution obtained by the minimization problem
- $\nabla\chi$ as the three-dimensional gradient operator applied on the susceptibility distribution
- $M_D$ as the binary gradient weighting diagonal matrix: diagonal elements are zero if they correspond to non-negligible gradients in the magnitude images and one otherwise; edges are non-negligible if they are five times greater than the background noise standard deviation in the magnitude image;

- $F_G$ is a matrix encoding the convolution with the unit dipole: $F_G = \mathcal{F}^{-1}G(\mathbf{k})\mathcal{F}$ with $G(\mathbf{k})$ is the dipole kernel described by Green's function in k-space (see Eq. 2.22).
- $B_{int}$ is the local field map obtained by background field removal
- $W$ is a data weighting matrix to account for spatially, nonuniform phase noise; the data weighting $W$ and the expected noise level $\epsilon$ are derived from the magnitude images

The constrained convex optimization problem in Eq. A.29 can be reformulated in unconstrained Lagrangian form with the regularization parameter $\lambda$ [30]:

$$\chi_{min} = \arg\min_{\chi} \|M_D \nabla\chi\|_1 + \lambda\|W(B_{int} - F_G\,\chi)\|_2^2 \tag{A.30}$$

The parameter $\lambda$ should be chosen such that $\|W(B_{int} - F_G\,\chi)\|_2 = \epsilon$ [30].

Hence, from all candidate solutions fulfilling the data fidelity constraint, MEDI selects the solution with the sparsest discrepancy to the anatomical prior [139]. During the iterative dipole inversion, unreliable phase information is modeled as being contaminated by normally distributed random noise using the data weighting matrix $W$ [139]. MEDI was extended to non-linear, morphology-enabled, dipole inversion (nMEDI) to account for residual noise and erroneous phase unwrapping. These residual artifacts are addressed by expressing the data fidelity constraint using complex exponential functions of the field as well as susceptibility, and by applying model error reduction through iterative tuning (MERIT) to improve the data weighting process [139]:

$$\chi_{min} = \arg\min_{\chi} \|M_D \nabla\chi\|_1 + \lambda\|W_N(\exp(iG\,\chi) - \exp(iB_{int}))\|_2^2 \tag{A.31}$$

with:

- $i^2 = -1$ as the imaginary unit
- exp( ) as complex exponential functions; exponential functions are immune to erroneous phase wraps and are highly nonlinear, thus, account better for signal noise
- $W_N$ is the iteratively computed data weighting matrix using MERIT

At the end of a nMEDI iteration $N$, the weighting $W_N$ is dynamically reduced. To that end, MERIT estimates the voxel-wise residual $\rho = W_n|\exp(iG\,\chi) - W\exp(iB_{int})|$. Subsequently, the standard deviation $\sigma_N$ of $\rho$ over all voxels is computed. If the residual $\rho$ of a voxel $v$ is greater than $6\sigma_N$, the voxel is considered to be corrupted and the corresponding data weighting is updated as $W_{N+1,v} = W_{N,v}/(\rho_{n,v}/\sigma_n)^2$ [139].

## B Supporting information for QSM study

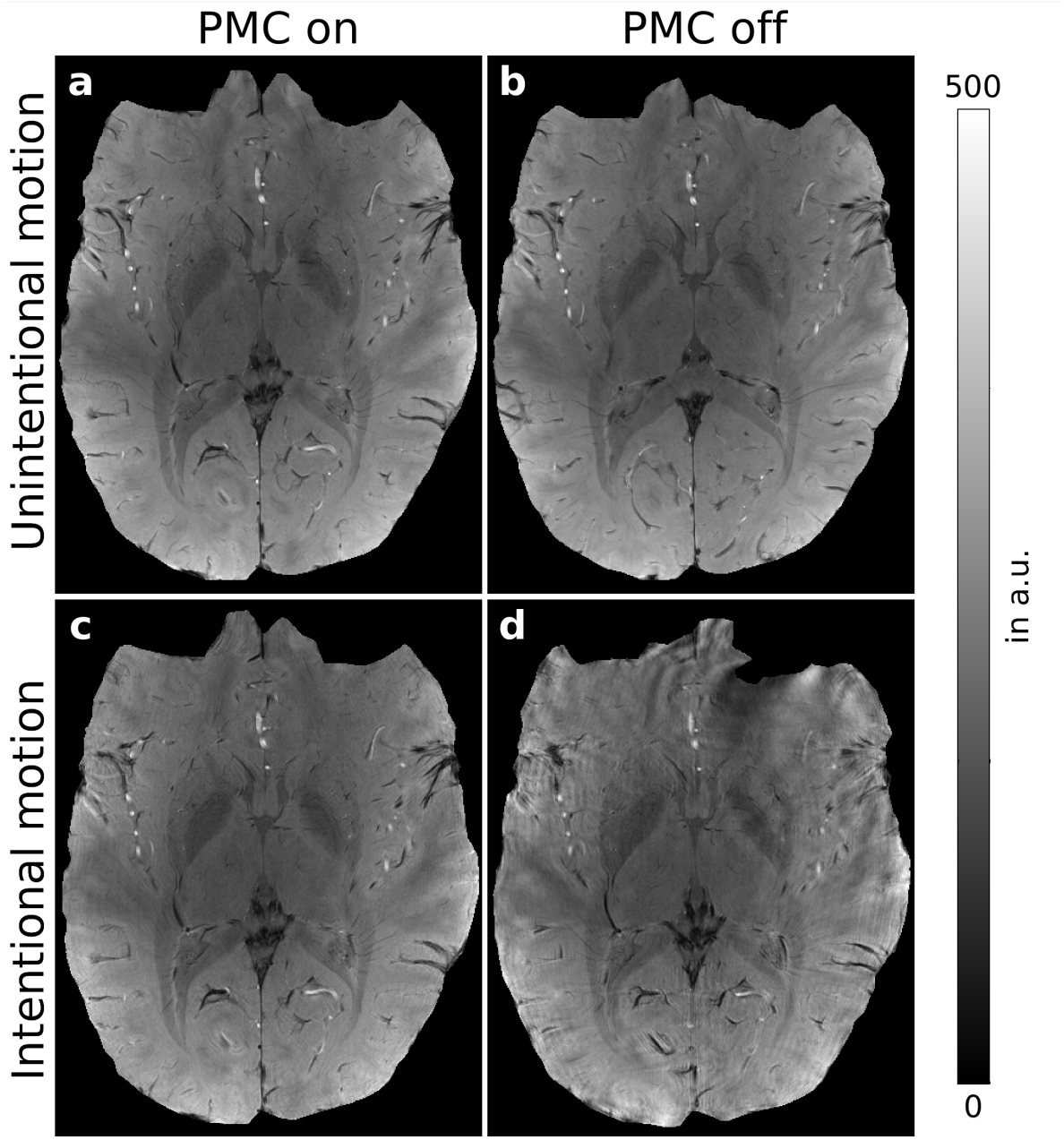


Figure B.1: Intra-subject comparison (subject #3) of (a, c) motion-corrected and (b, d) uncorrected magnitude images (after skull stripping) during (a, b) unintentional, small scale and (c, d) intentional, large-scale motion after brain extraction.

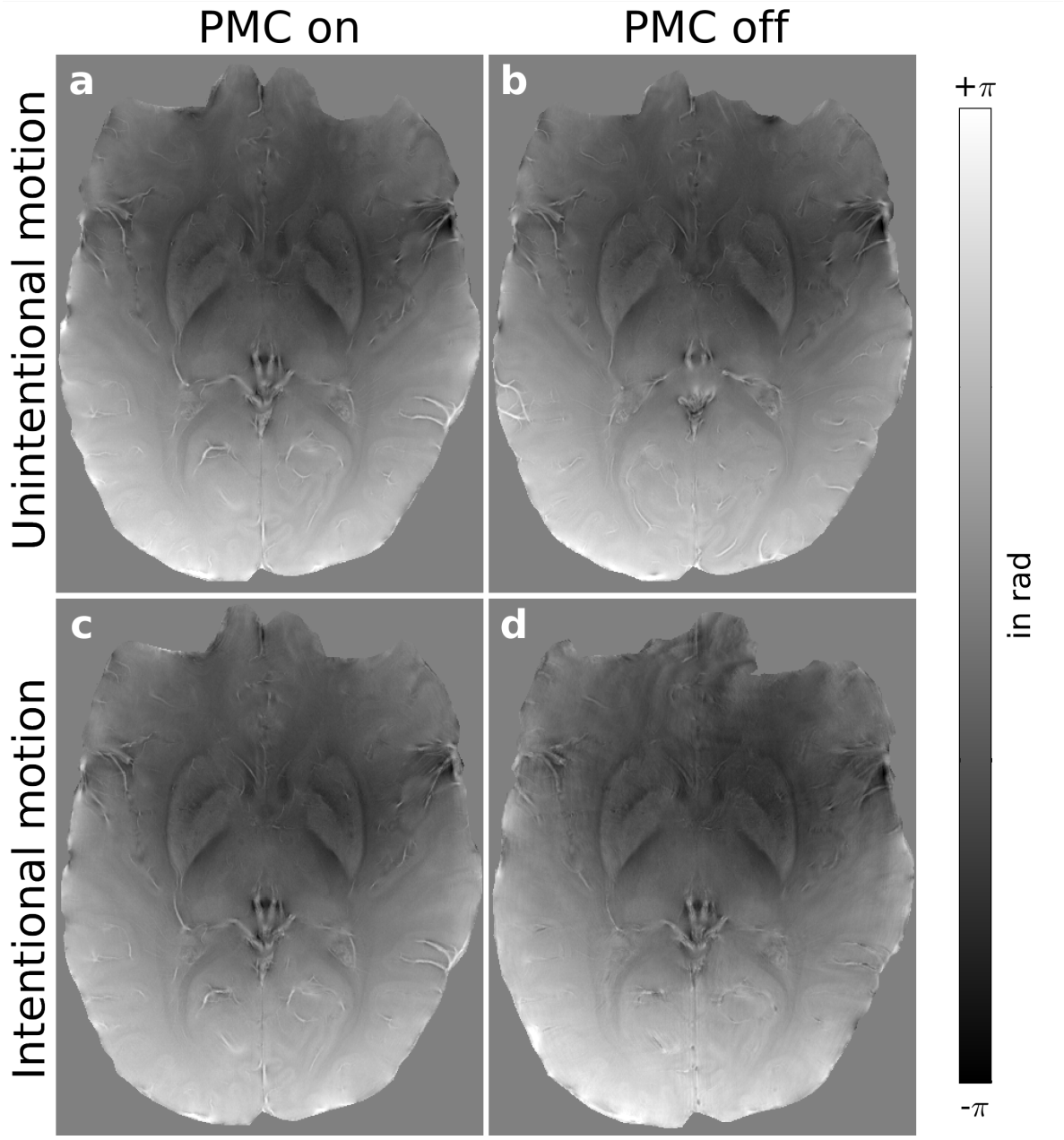


Figure B.2: Intra-subject comparison (subject #3) of (a, c) motion-corrected and (b, d) uncorrected field maps (unwrapped phase images) during (a, b) unintentional, small scale and (c, d) intentional, large-scale motion after brain extraction.

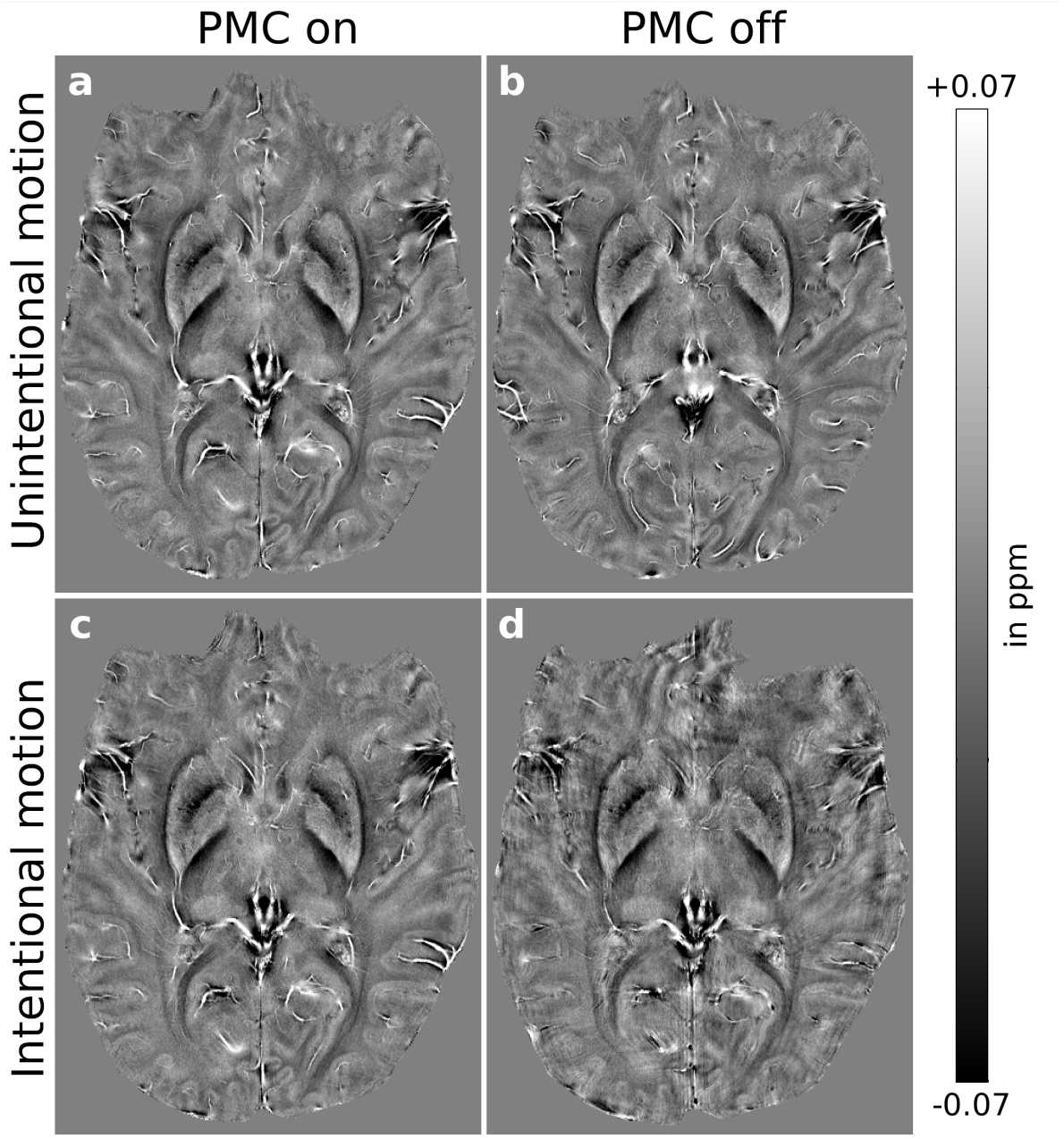


Figure B.3: Intra-subject comparison (subject #3) of (a, c) motion-corrected and (b, d) uncorrected local fields (SMV filtered) during (a, b) unintentional, small scale and (c, d) intentional, large-scale motion after brain extraction.
Spherical Mean Value (SMV)

# C Supporting information for ToF angiography study

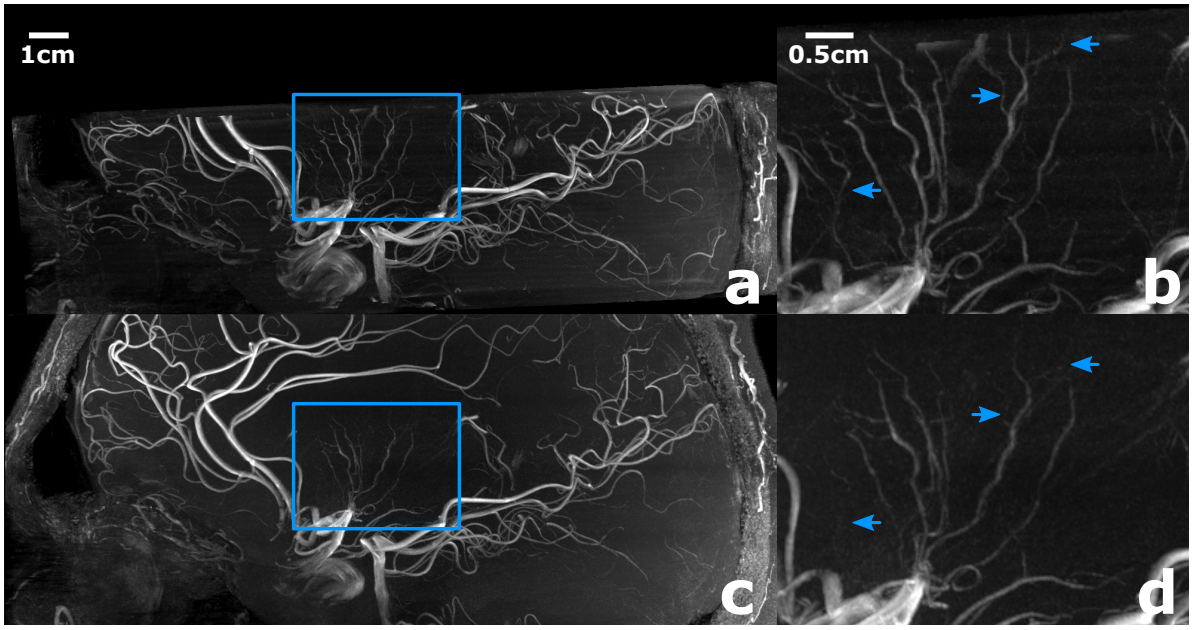


Figure C.1: Sagittal MIPs of (a) the 150 µm data set registered to (c) the 250 µm interpolated with zero-filling to 150 µm . (c, d) show zoomed ROIs corresponding to the blue boxes in (a) and (c). The slice coverage of the 150 µm data set was lower, thus, black regions in the MIPs are present. Nevertheless, the lenticulostriate arteries (blue arrows) were covered sufficiently in both scans and the slab angulation difference was mild, while the 150 µm depicted the lenticulostriate arteries with greater detail than the zero-filled data. Therefore, interpolation artifacts (from the registration process) and difference in slab orientation seem to have no decisive effect on the analysis done in this study.
Maximum Intensity Projection (MIP); Region of Interest (ROI).

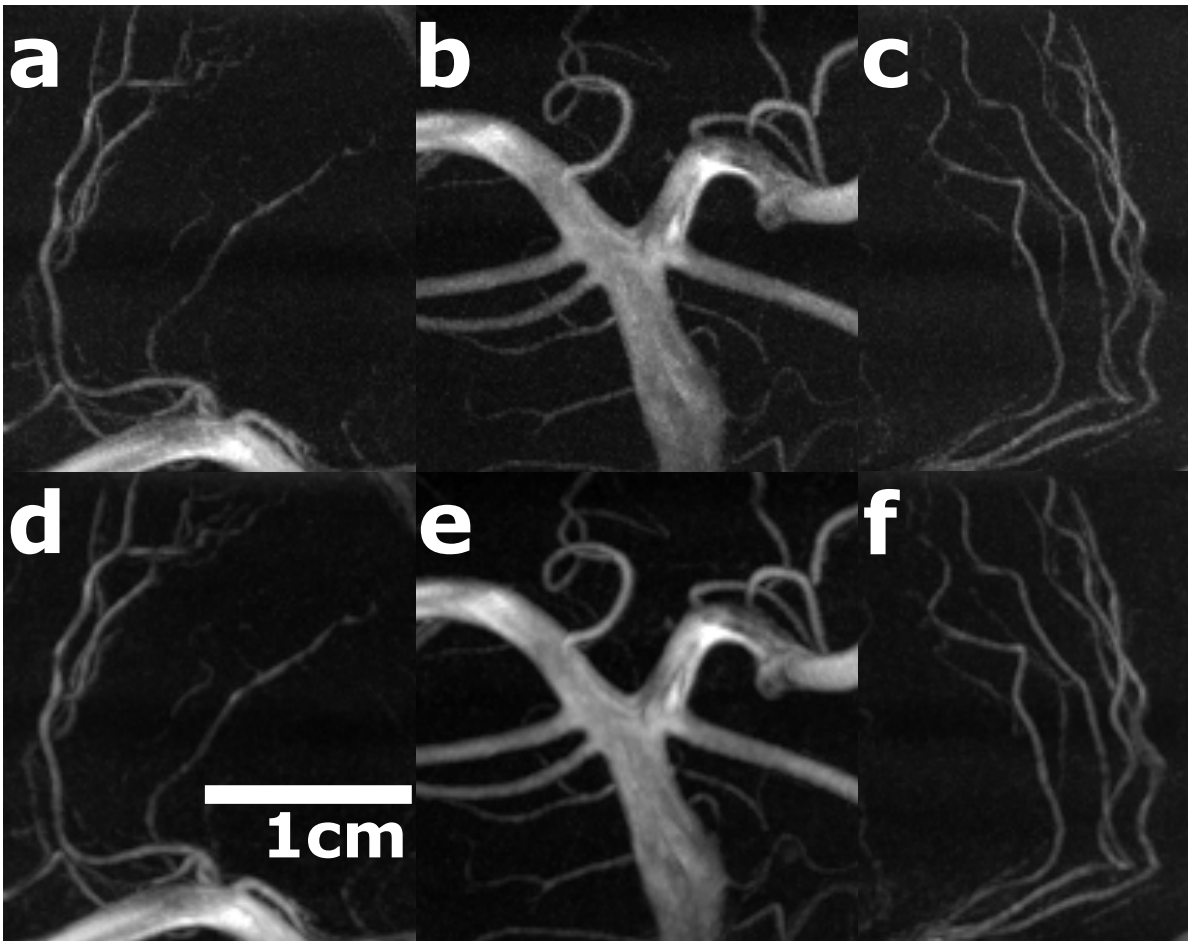


Figure C.2: Comparison of coronal, regional MIPs for (a, b, c) fully sampled 150 µm , and (d, e, f) 250 µm synthesized from the 150 µm by setting the corresponding high frequency components to zero in k-space. Depicted vessels are (a, d) right lenticulostriate arteries, (b, e) basal artery, and (c, f) left lenticulostriate arteries.
Maximum Intensity Projection (MIP).

# Bibliography


[1] V. R. Fuchs and H. C. Sox, "Physicians' Views Of The Relative Importance Of Thirty Medical Innovations," *Health Affairs*, vol. 20, no. 5, pp. 30–42, 2001.

[2] P. Balchandani and T. P. Naidich, "Ultra-High-Field MR Neuroimaging," *AJNR. American journal of neuroradiology*, vol. 36, no. 7, pp. 1204–1215, 2015.

[3] M. E. Ladd, P. Bachert, M. Meyerspeer, E. Moser, A. M. Nagel, D. G. Norris, S. Schmitter, O. Speck, S. Straub, and M. Zaiss, "Pros and cons of ultra-high-field MRI/MRS for human application," *Progress in Nuclear Magnetic Resonance Spectroscopy*, vol. 109, pp. 1–50, 2018.

[4] J. H. Duyn, "The future of ultra-high field MRI and fMRI for study of the human brain," *NeuroImage*, vol. 62, no. 2, pp. 1241–1248, 2012.

[5] W. van der Zwaag, A. Schafer, J. P. Marques, R. Turner, and R. Trampel, "Recent applications of UHF-MRI in the study of human brain function and structure: a review," *NMR in biomedicine*, vol. 29, no. 9, pp. 1274–1288, 2016.

[6] J. Hendrikse, J. J. Zwanenburg, F. Visser, T. Takahara, and P. Luijten, "Noninvasive depiction of the lenticulostriate arteries with time-of-flight MR angiography at 7.0 T," *Cerebrovascular diseases (Basel, Switzerland)*, vol. 26, no. 6, pp. 624–629, 2008.

[7] C.-K. Kang, C.-W. Park, J.-Y. Han, S.-H. Kim, C.-A. Park, K.-N. Kim, S.-M. Hong, Y.-B. Kim, K. H. Lee, and Z.-H. Cho, "Imaging and analysis of lenticulostriate arteries using 7.0-Tesla magnetic resonance angiography," *Magnetic resonance in medicine*, vol. 61, no. 1, pp. 136–144, 2009.

[8] A. Deistung, A. Schäfer, F. Schweser, U. Biedermann, R. Turner, and J. R. Reichenbach, "Toward in vivo histology: A comparison of quantitative susceptibility mapping (QSM) with magnitude-, phase-, and R2*-imaging at ultra-high magnetic field strength," *NeuroImage*, vol. 65, pp. 299–314, 2013.

[9] A. Minagar, W. Jy, J. J. Jimenez, and J. S. Alexander, "Multiple sclerosis as a vascular disease," *Neurological research*, vol. 28, no. 3, pp. 230–235, 2006.

[10] K. A. Jellinger and J. Attems, "Prevalence and impact of cerebrovascular pathology in Alzheimer's disease and parkinsonism," *Acta neurologica Scandinavica*, vol. 114, no. 1, pp. 38–46, 2006.

[11] M. Herbst, J. Maclaren, C. Lovell-Smith, R. Sostheim, K. Egger, A. Harloff, J. Korvink, J. Hennig, and M. Zaitsev, "Reproduction of motion artifacts for performance analysis of prospective motion correction in MRI," *Magnetic Resonance in Medicine*, vol. 71, no. 1, pp. 182–190, 2014.

[12] D. Stucht, K. A. Danishad, P. Schulze, F. Godenschweger, M. Zaitsev, and O. Speck, "Highest Resolution In Vivo Human Brain MRI Using Prospective Motion Correction," *PloS one*, vol. 10, no. 7, p. e0133921, 2015.

[13] F. Lüsebrink, A. Sciarra, H. Mattern, R. Yakupov, and O. Speck, "T1-weighted in vivo human whole brain MRI dataset with an ultrahigh isotropic resolution of 250 μm," *Scientific Data*, vol. 4, p. 170032, 2017.

[14] F. Lüsebrink, A. Sciarra, H. Mattern, R. Yakupov, and O. Speck, "Erratum: T1-weighted in vivo human whole brain MRI dataset with an ultrahigh isotropic resolution of 250 μm," *Scientific*

*Data*, vol. 4, p. 170062, 2017.

[15] M. A. Brown and R. C. Semelka, *MRI: Basic principles and applications.* Hoboken, N.J.: Wiley-Liss, 3rd ed. ed., 2003.

[16] M. A. Bernstein, K. F. King, and X. J. Zhou, *Handbook of MRI pulse sequences.* Amsterdam and Boston: Academic Press, 2004.

[17] E. M. Haacke, *Magnetic resonance imaging: Physical principles and sequence design.* New York: Wiley, ©1999.

[18] D. W. McRobbie, *MRI from picture to proton.* Cambridge: Cambridge University Press, second edition ed., 2007.

[19] M. H. Levitt, *Spin dynamics: Basics of nuclear magnetic resonance / Malcolm H. Levitt.* Hoboken, N.J.: Wiley and Chichester : John Wiley [distributor], 2nd ed. ed., 2008.

[20] J. H. Duyn and J. Schenck, "Contributions to magnetic susceptibility of brain tissue," *NMR in biomedicine*, vol. 30, no. 4, 2017.

[21] A. Deistung, F. Schweser, and J. R. Reichenbach, "Overview of quantitative susceptibility mapping," *NMR in biomedicine*, 2016.

[22] B. A. Hargreaves, "Rapid gradient-echo imaging," *Journal of magnetic resonance imaging : JMRI*, vol. 36, no. 6, pp. 1300–1313, 2012.

[23] E. M. Haacke, S. Liu, S. Buch, W. Zheng, D. Wu, and Y. Ye, "Quantitative susceptibility mapping: current status and future directions," *J Magn Reson Imaging*, vol. 33, no. 1, pp. 1–25, 2015.

[24] E. M. Haacke and J. R. Reichenbach, *Susceptibility Weighted Imaging in MRI.* Hoboken, NJ, USA: John Wiley & Sons, Inc, 2011.

[25] Y. Wang and T. Liu, "Quantitative susceptibility mapping (QSM): Decoding MRI data for a tissue magnetic biomarker," *Magnetic resonance in medicine*, vol. 73, no. 1, pp. 82–101, 2015.

[26] F. Schweser, S. D. Robinson, L. de Rochefort, W. Li, and K. Bredies, "An illustrated comparison of processing methods for phase MRI and QSM: Removal of background field contributions from sources outside the region of interest," *NMR in biomedicine*, vol. 30, no. 4, 2017.

[27] F. Schweser, A. Deistung, B. W. Lehr, and J. R. Reichenbach, "Differentiation between diamagnetic and paramagnetic cerebral lesions based on magnetic susceptibility mapping," *Medical physics*, vol. 37, no. 10, pp. 5165–5178, 2010.

[28] D. Zhou, T. Liu, P. Spincemaille, and Y. Wang, "Background field removal by solving the Laplacian boundary value problem," *NMR in biomedicine*, vol. 27, no. 3, pp. 312–319, 2014.

[29] T. Liu, P. Spincemaille, L. de Rochefort, B. Kressler, and Y. Wang, "Calculation of susceptibility through multiple orientation sampling (COSMOS): a method for conditioning the inverse problem from measured magnetic field map to susceptibility source image in MRI," *Magnetic resonance in medicine*, vol. 61, no. 1, pp. 196–204, 2009.

[30] T. Liu, J. Liu, L. de Rochefort, P. Spincemaille, I. Khalidov, J. R. Ledoux, and Y. Wang, "Morphology enabled dipole inversion (MEDI) from a single-angle acquisition: Comparison with COSMOS in human brain imaging," *Magnetic resonance in medicine*, vol. 66, no. 3, pp. 777–783, 2011.

[31] C. Langkammer, F. Schweser, K. Shmueli, C. Kames, X. Li, L. Guo, C. Milovic, J. Kim, H. Wei, K. Bredies, S. Buch, Y. Guo, Z. Liu, J. Meineke, A. Rauscher, J. P. Marques, and B. Bilgic, "Quantitative susceptibility mapping: Report from the 2016 reconstruction challenge," *Magnetic resonance in medicine*, 2017.

[32] W. Li, B. Wu, and C. Liu, "Quantitative susceptibility mapping of human brain reflects spatial variation in tissue composition," *NeuroImage*, vol. 55, no. 4, pp. 1645–1656, 2011.

[33] C. cocLiu, "Susceptibility tensor imaging," *Magnetic resonance in medicine*, vol. 63, no. 6, pp. 1471–1477, 2010.

[34] D. G. Nishimura, "Time-of-flight MR angiography," *Magnetic Resonance in Medicine*, vol. 14, no. 2, pp. 194–201, 1990.

[35] L. J. de Cocker, A. Lindenholz, J. J. Zwanenburg, A. van der Kolk, M. Zwartbol, P. Luijten, and J. Hendrikse, "Clinical Vascular Imaging in the Brain at 7 T," *NeuroImage*, 2016.

[36] C. Sadikin, M. M.-H. Teng, T.-Y. Chen, C.-B. Luo, F.-C. Chang, J.-F. Lirng, and Y.-C. Sun, "The Current Role of 1.5T Non-contrast 3D Time-of-flight Magnetic Resonance Angiography to Detect Intracranial Steno-occlusive Disease," *Journal of the Formosan Medical Association*, vol. 106, no. 9, pp. 691–699, 2007.

[37] B. Mine, M. Pezzullo, G. Roque, P. David, T. Metens, and B. Lubicz, "Detection and characterization of unruptured intracranial aneurysms: Comparison of 3T MRA and DSA," *Journal of neuroradiology. Journal de neuroradiologie*, vol. 42, no. 3, pp. 162–168, 2015.

[38] M.-H. Li, Y.-D. Li, B.-X. Gu, Y.-S. Cheng, W. Wang, H.-Q. Tan, and Y.-C. Chen, "Accurate diagnosis of small cerebral aneurysms </=5 mm in diameter with 3.0-T MR angiography," *Radiology*, vol. 271, no. 2, pp. 553–560, 2014.

[39] G. F. Gibbs, J. r. Huston, M. A. Bernstein, S. J. Riederer, and R. D. Brown, JR, "3.0-Tesla MR angiography of intracranial aneurysms: comparison of time-of-flight and contrast-enhanced techniques," *Journal of magnetic resonance imaging : JMRI*, vol. 21, no. 2, pp. 97–102, 2005.

[40] M. Azuma, T. Hirai, Y. Shigematsu, M. Kitajima, Y. Kai, S. Yano, H. Nakamura, K. Makino, Y. Iryo, and Y. Yamashita, "Evaluation of Intracranial Dural Arteriovenous Fistulas: Comparison of Unenhanced 3T 3D Time-of-flight MR Angiography with Digital Subtraction Angiography," *Magnetic resonance in medical sciences : MRMS : an official journal of Japan Society of Magnetic Resonance in Medicine*, vol. 14, no. 4, pp. 285–293, 2015.

[41] H. Uetani, M. Akter, T. Hirai, Y. Shigematsu, M. Kitajima, Y. Kai, S. Yano, H. Nakamura, K. Makino, M. Azuma, R. Murakami, and Y. Yamashita, "Can 3T MR Angiography Replace DSA for the Identification of Arteries Feeding Intracranial Meningiomas?," *American Journal of Neuroradiology*, vol. 34, no. 4, pp. 765–772, 2013.

[42] S. Yu, L. Yan, Y. Yao, S. Wang, M. Yang, B. Wang, Y. Zhuo, L. Ai, X. Miao, J. Zhao, and D. J. J. Wang, "Noncontrast dynamic MRA in intracranial arteriovenous malformation (AVM), comparison with time of flight (TOF) and digital subtraction angiography (DSA)," *Magnetic resonance imaging*, vol. 30, no. 6, pp. 869–877, 2012.

[43] J. O. Heidenreich, A. M. Schilling, F. Unterharnscheidt, R. Stendel, S. Hartlieb, F. K. Wacker, P. Schlattmann, K.-J. Wolf, and H. Bruhn, "Assessment of 3D-TOF-MRA at 3.0 Tesla in the characterization of the angioarchitecture of cerebral arteriovenous malformations: a preliminary study," *Acta radiologica (Stockholm, Sweden : 1987)*, vol. 48, no. 6, pp. 678–686, 2007.

[44] A. R. Weale and L. I. Jones, "Imaging in vascular disease," *Surgery (Oxford)*, vol. 30, no. 8, pp. 383–389, 2012.

[45] R. A. Willinsky, S. M. Taylor, K. TerBrugge, R. I. Farb, G. Tomlinson, and W. Montanera, "Neurologic complications of cerebral angiography: prospective analysis of 2,899 procedures and review of the literature," *Radiology*, vol. 227, no. 2, pp. 522–528, 2003.

[46] H. J. Cloft, G. J. Joseph, and J. E. Dion, "Risk of Cerebral Angiography in Patients With

Subarachnoid Hemorrhage, Cerebral Aneurysm, and Arteriovenous Malformation: A Meta-Analysis," *Stroke*, vol. 30, no. 2, pp. 317–320, 1999.

[47] J. C. Carr and T. J. Carroll, *Magnetic Resonance Angiography.* New York, NY: Springer New York, 2012.

[48] D. D. Blatter, D. L. Parker, and R. O. Robison, "Cerebral MR angiography with multiple overlapping thin slab acquisition. Part I. Quantitative analysis of vessel visibility," *Radiology*, vol. 179, no. 3, pp. 805–811, 1991.

[49] D. L. Parker, C. Yuan, and D. D. Blatter, "MR angiography by multiple thin slab 3D acquisition," *Magnetic Resonance in Medicine*, vol. 17, no. 2, pp. 434–451, 1991.

[50] D. Atkinson, M. Brant-Zawadzki, G. Gillan, D. Purdy, and G. Laub, "Improved MR angiography: magnetization transfer suppression with variable flip angle excitation and increased resolution," *Radiology*, vol. 190, no. 3, pp. 890–894, 1994.

[51] G. B. Pike, B. S. Hu, G. H. Glover, and D. R. Enzmann, "Magnetization transfer time-of-flight magnetic resonance angiography," *Magnetic Resonance in Medicine*, vol. 25, no. 2, pp. 372–379, 1992.

[52] D. L. Parker, H. R. Buswell, K. C. Goodrich, A. L. Alexander, N. Keck, and J. S. Tsuruda, "The application of magnetization transfer to MR angiography with reduced total power," *Magnetic Resonance in Medicine*, vol. 34, no. 2, pp. 283–286, 1995.

[53] S. J. Graham and R. M. Henkelman, "Understanding pulsed magnetization transfer," *Journal of Magnetic Resonance Imaging*, vol. 7, no. 5, pp. 903–912, 1997.

[54] M. E. Ladd, "High-field-strength magnetic resonance: potential and limits," *Topics in magnetic resonance imaging : TMRI*, vol. 18, no. 2, pp. 139–152, 2007.

[55] O. Speck, "Warum 7-Tesla-1-H-MRT im Gehirn?," *Journal für Neurologie, Neurochirurgie und Psychiatrie*, 2012.

[56] R. Pohmann, O. Speck, and K. Scheffler, "Signal-to-noise ratio and MR tissue parameters in human brain imaging at 3, 7, and 9.4 tesla using current receive coil arrays," *Magnetic resonance in medicine*, vol. 75, no. 2, pp. 801–809, 2016.

[57] A. Fracasso, S. J. van Veluw, F. Visser, P. R. Luijten, W. Spliet, J. J. M. Zwanenburg, S. O. Dumoulin, and N. Petridou, "Myelin contrast across lamina at 7T, ex-vivo and in-vivo dataset," *Data in brief*, vol. 8, pp. 990–1003, 2016.

[58] A. Fracasso, S. J. van Veluw, F. Visser, P. R. Luijten, W. Spliet, J. J. M. Zwanenburg, S. O. Dumoulin, and N. Petridou, "Lines of Baillarger in vivo and ex vivo: Myelin contrast across lamina at 7T MRI and histology," *NeuroImage*, vol. 133, pp. 163–175, 2016.

[59] S. Lehericy, E. Bardinet, C. Poupon, M. Vidailhet, and C. Francois, "7 Tesla magnetic resonance imaging: a closer look at substantia nigra anatomy in Parkinson's disease," *Movement disorders : official journal of the Movement Disorder Society*, vol. 29, no. 13, pp. 1574–1581, 2014.

[60] S. Kashyap, D. Ivanov, M. Havlicek, S. Sengupta, B. A. Poser, and K. Uludağ, "Resolving laminar activation in human V1 using ultra-high spatial resolution fMRI at 7T," *Scientific reports*, vol. 8, no. 1, p. 17063, 2018.

[61] E. Kuehn and M. I. Sereno, "Modelling the Human Cortex in Three Dimensions," *Trends in cognitive sciences*, vol. 22, no. 12, pp. 1073–1075, 2018.

[62] I. Marquardt, M. Schneider, O. F. Gulban, D. Ivanov, and K. Uludağ, "Cortical depth profiles of luminance contrast responses in human V1 and V2 using 7 T fMRI," *Human brain mapping*, vol. 39, no. 7, pp. 2812–2827, 2018.

[63] A. P. Fan, B. Bilgic, L. Gagnon, T. Witzel, H. Bhat, B. R. Rosen, and E. Adalsteinsson, "Quantitative oxygenation venography from MRI phase," *Magnetic Resonance in Medicine*, vol. 72, no. 1, pp. 149–159, 2014.

[64] F. Schweser, A. Deistung, B. W. Lehr, and J. R. Reichenbach, "Quantitative imaging of intrinsic magnetic tissue properties using MRI signal phase: an approach to in vivo brain iron metabolism?," *NeuroImage*, vol. 54, no. 4, pp. 2789–2807, 2011.

[65] C. Stuber, M. Morawski, A. Schafer, C. Labadie, M. Wahnert, C. Leuze, M. Streicher, N. Barapatre, K. Reimann, S. Geyer, D. Spemann, and R. Turner, "Myelin and iron concentration in the human brain: a quantitative study of MRI contrast," *NeuroImage*, vol. 93 Pt 1, pp. 95–106, 2014.

[66] A. Deistung, F. Schweser, B. Wiestler, M. Abello, M. Roethke, F. Sahm, W. Wick, A. M. Nagel, S. Heiland, H.-P. Schlemmer, M. Bendszus, J. R. Reichenbach, and A. Radbruch, "Quantitative susceptibility mapping differentiates between blood depositions and calcifications in patients with glioblastoma," *PloS one*, vol. 8, no. 3, p. e57924, 2013.

[67] S. Chang, J. Zhang, T. Liu, A. J. Tsiouris, J. Shou, T. Nguyen, D. Leifer, Y. Wang, and I. Kovanlikaya, "Quantitative Susceptibility Mapping of Intracerebral Hemorrhages at Various Stages," *Journal of magnetic resonance imaging : JMRI*, vol. 44, no. 2, pp. 420–425, 2016.

[68] J. Liu, S. Xia, R. Hanks, N. Wiseman, C. Peng, S. Zhou, E. M. Haacke, and Z. Kou, "Susceptibility Weighted Imaging and Mapping of Micro-Hemorrhages and Major Deep Veins after Traumatic Brain Injury," *Journal of neurotrauma*, vol. 33, no. 1, pp. 10–21, 2016.

[69] W. Li, B. Wu, A. Batrachenko, V. Bancroft-Wu, R. A. Morey, V. Shashi, C. Langkammer, M. D. de Bellis, S. Ropele, A. W. Song, and C. Liu, "Differential developmental trajectories of magnetic susceptibility in human brain gray and white matter over the lifespan," *Human brain mapping*, vol. 35, no. 6, pp. 2698–2713, 2014.

[70] N. Persson, J. Wu, Q. Zhang, T. Liu, J. Shen, R. Bao, M. Ni, T. Liu, Y. Wang, and P. Spincemaille, "Age and sex related differences in subcortical brain iron concentrations among healthy adults," *NeuroImage*, vol. 122, pp. 385–398, 2015.

[71] J. Acosta-Cabronero, M. J. Betts, A. Cardenas-Blanco, S. Yang, and P. J. Nestor, "In Vivo MRI Mapping of Brain Iron Deposition across the Adult Lifespan," *The Journal of neuroscience : the official journal of the Society for Neuroscience*, vol. 36, no. 2, pp. 364–374, 2016.

[72] M. J. Betts, J. Acosta-Cabronero, A. Cardenas-Blanco, P. J. Nestor, and E. Duzel, "High-resolution characterisation of the aging brain using simultaneous quantitative susceptibility mapping (QSM) and R* measurements at 7T," *NeuroImage*, 2016.

[73] M. Liu, S. Liu, K. Ghassaban, W. Zheng, D. Dicicco, Y. Miao, C. Habib, T. Jazmati, and E. M. Haacke, "Assessing global and regional iron content in deep gray matter as a function of age using susceptibility mapping," *Journal of magnetic resonance imaging : JMRI*, vol. 44, no. 1, pp. 59–71, 2016.

[74] Y. Zhang, H. Wei, M. J. Cronin, N. He, F. Yan, and C. Liu, "Longitudinal atlas for normative human brain development and aging over the lifespan using quantitative susceptibility mapping," *NeuroImage*, 2018.

[75] C. Langkammer, T. Liu, M. Khalil, C. Enzinger, M. Jehna, S. Fuchs, F. Fazekas, Y. Wang, and S. Ropele, "Quantitative susceptibility mapping in multiple sclerosis," *Radiology*, vol. 267, no. 2, pp. 551–559, 2013.

[76] C. Wisnieff, S. Ramanan, J. Olesik, S. Gauthier, Y. Wang, and D. Pitt, "Quantitative susceptibility mapping (QSM) of white matter multiple sclerosis lesions: Interpreting positive susceptibility and

the presence of iron," *Magnetic resonance in medicine*, vol. 74, no. 2, pp. 564–570, 2015.

[77] J. Acosta-Cabronero, G. B. Williams, A. Cardenas-Blanco, R. J. Arnold, V. Lupson, and P. J. Nestor, "In vivo quantitative susceptibility mapping (QSM) in Alzheimer's disease," *PloS one*, vol. 8, no. 11, p. e81093, 2013.

[78] Y. Moon, S.-H. Han, and W.-J. Moon, "Patterns of Brain Iron Accumulation in Vascular Dementia and Alzheimer's Dementia Using Quantitative Susceptibility Mapping Imaging," *Journal of Alzheimer's disease : JAD*, vol. 51, no. 3, pp. 737–745, 2016.

[79] N. He, H. Ling, B. Ding, J. Huang, Y. Zhang, Z. Zhang, C. Liu, K. Chen, and F. Yan, "Region-specific disturbed iron distribution in early idiopathic Parkinson's disease measured by quantitative susceptibility mapping," *Human brain mapping*, vol. 36, no. 11, pp. 4407–4420, 2015.

[80] X. Guan, M. Xuan, Q. Gu, P. Huang, C. Liu, N. Wang, X. Xu, W. Luo, and M. Zhang, "Regionally progressive accumulation of iron in Parkinson's disease as measured by quantitative susceptibility mapping," *NMR in biomedicine*, 2016.

[81] J. M. G. van Bergen, J. Hua, P. G. Unschuld, I. A. L. Lim, C. K. Jones, R. L. Margolis, C. A. Ross, P. C. M. van Zijl, and X. Li, "Quantitative Susceptibility Mapping Suggests Altered Brain Iron in Premanifest Huntington Disease," *AJNR. American journal of neuroradiology*, vol. 37, no. 5, pp. 789–796, 2016.

[82] A. D. Schweitzer, T. Liu, A. Gupta, K. Zheng, S. Seedial, A. Shtilbans, M. Shahbazi, D. Lange, Y. Wang, and A. J. Tsiouris, "Quantitative susceptibility mapping of the motor cortex in amyotrophic lateral sclerosis and primary lateral sclerosis," *AJR. American journal of roentgenology*, vol. 204, no. 5, pp. 1086–1092, 2015.

[83] M. Juhas, H. Sun, M. R. G. Brown, M. B. MacKay, K. F. Mann, W. H. Sommer, A. H. Wilman, S. M. Dursun, and A. J. Greenshaw, "Deep grey matter iron accumulation in alcohol use disorder," *NeuroImage*, vol. 148, pp. 115–122, 2017.

[84] U. Lobel, F. Schweser, M. Nickel, A. Deistung, R. Grosse, C. Hagel, J. Fiehler, A. Schulz, M. Hartig, J. R. Reichenbach, A. Kohlschutter, and J. Sedlacik, "Brain iron quantification by MRI in mitochondrial membrane protein-associated neurodegeneration under iron-chelating therapy," *Annals of clinical and translational neurology*, vol. 1, no. 12, pp. 1041–1046, 2014.

[85] D. Z. Balla, R. M. Sanchez-Panchuelo, S. J. Wharton, G. E. Hagberg, K. Scheffler, S. T. Francis, and R. Bowtell, "Functional quantitative susceptibility mapping (fQSM)," *NeuroImage*, vol. 100, pp. 112–124, 2014.

[86] P.-L. Bazin, V. Plessis, A. P. Fan, A. Villringer, and C. J. Gauthier, "Vessel segmentation from quantitative susceptibility maps for local oxygenation venography," in *2016 IEEE 13th International Symposium on Biomedical Imaging: From Nano to Macro*, (Piscataway, NJ), pp. 1135–1138, IEEE, 2016.

[87] J. Zhang, J. Cho, D. Zhou, T. D. Nguyen, P. Spincemaille, A. Gupta, and Y. Wang, "Quantitative susceptibility mapping-based cerebral metabolic rate of oxygen mapping with minimum local variance," *Magnetic resonance in medicine*, 2017.

[88] J. Zhang, T. Liu, A. Gupta, P. Spincemaille, T. D. Nguyen, and Y. Wang, "Quantitative mapping of cerebral metabolic rate of oxygen (CMRO2 ) using quantitative susceptibility mapping (QSM)," *Magnetic resonance in medicine*, vol. 74, no. 4, pp. 945–952, 2015.

[89] A. Karsa, S. Punwani, and K. Shmueli, "The effect of low resolution and coverage on the accuracy of susceptibility mapping," *Magnetic resonance in medicine*, 2018.

[90] M. Fukunaga, T.-Q. Li, P. van Gelderen, J. A. de Zwart, K. Shmueli, B. Yao, J. Lee, D. Maric,

M. A. Aronova, G. Zhang, R. D. Leapman, J. F. Schenck, H. Merkle, and J. H. Duyn, "Layer-specific variation of iron content in cerebral cortex as a source of MRI contrast," *Proceedings of the National Academy of Sciences of the United States of America*, vol. 107, no. 8, pp. 3834–3839, 2010.

[91] S. D. Robinson, K. Bredies, D. Khabipova, B. Dymerska, J. P. Marques, and F. Schweser, "An illustrated comparison of processing methods for MR phase imaging and QSM: Combining array coil signals and phase unwrapping," *NMR in biomedicine*, vol. 30, no. 4, 2017.

[92] J. T. Heverhagen, E. Bourekas, S. Sammet, M. V. Knopp, and P. Schmalbrock, "Time-of-flight magnetic resonance angiography at 7 Tesla," *Investigative radiology*, vol. 43, no. 8, pp. 568–573, 2008.

[93] C. von Morze, D. Xu, D. D. Purcell, C. P. Hess, P. Mukherjee, D. Saloner, D. A. C. Kelley, and D. B. Vigneron, "Intracranial time-of-flight MR angiography at 7T with comparison to 3T," *Journal of magnetic resonance imaging : JMRI*, vol. 26, no. 4, pp. 900–904, 2007.

[94] A. C. Stamm, C. L. Wright, M. V. Knopp, P. Schmalbrock, and J. T. Heverhagen, "Phase contrast and time-of-flight magnetic resonance angiography of the intracerebral arteries at 1.5, 3 and 7 T," *Magnetic resonance imaging*, vol. 31, no. 4, pp. 545–549, 2013.

[95] C.-K. Kang, C.-A. Park, C.-W. Park, Y.-B. Lee, Z.-H. Cho, and Y.-B. Kim, "Lenticulostriate arteries in chronic stroke patients visualised by 7 T magnetic resonance angiography," *International journal of stroke : official journal of the International Stroke Society*, vol. 5, no. 5, pp. 374–380, 2010.

[96] M. M. A. Conijn, J. Hendrikse, J. J. M. Zwanenburg, T. Takahara, M. I. Geerlings, W. P. T. M. Mali, and P. R. Luijten, "Perforating arteries originating from the posterior communicating artery: a 7.0-Tesla MRI study," *European radiology*, vol. 19, no. 12, pp. 2986–2992, 2009.

[97] M. Laurig, X. Liu, M. Wyss, A. Gietl, L. Jellestad, R. M. Nitsch, K. Prüssmann, C. Hock, and P. G. Unschuld, "Quantification of subcortical gray-matter vascularization using 7 Tesla time-of-flight angiography," *Brain and behavior*, vol. 3, no. 5, pp. 515–518, 2013.

[98] V. I. Madai, von Samson-Himmelstjerna, Federico C, M. Bauer, K. L. Stengl, M. A. Mutke, E. Tovar-Martinez, J. Wuerfel, M. Endres, T. Niendorf, and J. Sobesky, "Ultrahigh-field MRI in human ischemic stroke–a 7 tesla study," *PloS one*, vol. 7, no. 5, p. e37631, 2012.

[99] T. Matsushige, M. Kraemer, M. Schlamann, P. Berlit, M. Forsting, M. E. Ladd, U. Sure, and K. H. Wrede, "Ventricular Microaneurysms in Moyamoya Angiopathy Visualized with 7T MR Angiography," *AJNR. American journal of neuroradiology*, vol. 37, no. 9, pp. 1669–1672, 2016.

[100] C.-A. Park, C.-K. Kang, Y.-B. Kim, and Z.-H. Cho, "Advances in MR angiography with 7T MRI: From microvascular imaging to functional angiography," *NeuroImage*, 2017.

[101] S. Conolly, D. Nishimura, A. Macovski, and G. Glover, "Variable-rate selective excitation," *Journal of Magnetic Resonance (1969)*, vol. 78, no. 3, pp. 440–458, 1988.

[102] S. Schmitter, M. Bock, S. Johst, E. J. Auerbach, K. Uğurbil, and Van de Moortele, Pierre-François, "Contrast enhancement in TOF cerebral angiography at 7 T using saturation and MT pulses under SAR constraints: impact of VERSE and sparse pulses," *Magnetic resonance in medicine : official journal of the Society of Magnetic Resonance in Medicine / Society of Magnetic Resonance in Medicine*, vol. 68, no. 1, pp. 188–197, 2012.

[103] S. Johst, K. H. Wrede, M. E. Ladd, and S. Maderwald, "Time-of-flight magnetic resonance angiography at 7 T using venous saturation pulses with reduced flip angles," *Investigative radiology*, vol. 47, no. 8, pp. 445–450, 2012.

[104] K. H. Wrede, S. Johst, P. Dammann, N. Özkan, C. Mönninghoff, M. Kraemer, S. Maderwald, M. E. Ladd, U. Sure, L. Umutlu, and M. Schlamann, "Improved cerebral time-of-flight magnetic resonance angiography at 7 Tesla–feasibility study and preliminary results using optimized venous saturation pulses," *PloS one*, vol. 9, no. 9, p. e106697, 2014.

[105] C. Lin, M. A. Bernstein, G. F. Gibbs, and J. Huston, "Reduction of RF power for magnetization transfer with optimized application of RF pulses in k-space," *Magnetic resonance in medicine : official journal of the Society of Magnetic Resonance in Medicine / Society of Magnetic Resonance in Medicine*, vol. 50, no. 1, pp. 114–121, 2003.

[106] S. D. Rane and J. C. Gore, "Measurement of T1 of human arterial and venous blood at 7T," *Magnetic resonance imaging*, vol. 31, no. 3, pp. 477–479, 2013.

[107] D. Kopeinigg, M. Aksoy, C. Forman, M. Straka, D. Seaman, J. Rosenberg, D. Fleischmann, J. Hornegger, and R. Bammer, "Prospective optical motion correction for 3D time-of-flight angiography," *Magnetic resonance in medicine : official journal of the Society of Magnetic Resonance in Medicine / Society of Magnetic Resonance in Medicine*, vol. 69, no. 6, pp. 1623–1633, 2013.

[108] J. Maclaren, M. Herbst, O. Speck, and M. Zaitsev, "Prospective motion correction in brain imaging: a review," *Magnetic resonance in medicine*, vol. 69, no. 3, pp. 621–636, 2013.

[109] J. B. Andre, B. W. Bresnahan, M. Mossa-Basha, M. N. Hoff, C. P. Smith, Y. Anzai, and W. A. Cohen, "Toward Quantifying the Prevalence, Severity, and Cost Associated With Patient Motion During Clinical MR Examinations," *Journal of the American College of Radiology*, vol. 12, no. 7, pp. 689–695, 2015.

[110] M. Zaitsev, J. Maclaren, and M. Herbst, "Motion artifacts in MRI: A complex problem with many partial solutions," *Journal of magnetic resonance imaging : JMRI*, vol. 42, no. 4, pp. 887–901, 2015.

[111] F. Godenschweger, U. Kagebein, D. Stucht, U. Yarach, A. Sciarra, R. Yakupov, F. Lusebrink, P. Schulze, and O. Speck, "Motion correction in MRI of the brain," *Physics in medicine and biology*, vol. 61, no. 5, pp. R32–56, 2016.

[112] A. Loktyushin, H. Nickisch, R. Pohmann, and B. Schölkopf, "Blind retrospective motion correction of MR images," *Magnetic Resonance in Medicine*, vol. 70, no. 6, pp. 1608–1618, 2013.

[113] J. G. Pipe, "Motion correction with PROPELLER MRI: Application to head motion and free-breathing cardiac imaging," *Magnetic Resonance in Medicine*, vol. 42, no. 5, pp. 963–969, 1999.

[114] E. B. Welch, A. Manduca, R. C. Grimm, H. A. Ward, and C. R. Jack, "Spherical navigator echoes for full 3D rigid body motion measurement in MRI," *Magnetic resonance in medicine*, vol. 47, no. 1, pp. 32–41, 2002.

[115] S. Thesen, O. Heid, E. Mueller, and L. R. Schad, "Prospective acquisition correction for head motion with image-based tracking for real-time fMRI," *Magnetic Resonance in Medicine*, vol. 44, no. 3, pp. 457–465, 2000.

[116] N. White, C. Roddey, A. Shankaranarayanan, E. Han, D. Rettmann, J. Santos, J. Kuperman, and A. Dale, "PROMO: Real-time prospective motion correction in MRI using image-based tracking," *Magnetic resonance in medicine*, vol. 63, no. 1, pp. 91–105, 2010.

[117] M. B. Ooi, S. Krueger, W. J. Thomas, S. V. Swaminathan, and T. R. Brown, "Prospective real-time correction for arbitrary head motion using active markers," *Magnetic resonance in medicine*, vol. 62, no. 4, pp. 943–954, 2009.

[118] M. Haeberlin, L. Kasper, C. Barmet, D. O. Brunner, B. E. Dietrich, S. Gross, B. J. Wilm,

S. Kozerke, and K. P. Pruessmann, "Real-time motion correction using gradient tones and head-mounted NMR field probes," *Magnetic Resonance in Medicine*, vol. 74, no. 3, pp. 647–660, 2015.

[119] A. Aranovitch, M. Haeberlin, S. Gross, B. E. Dietrich, B. J. Wilm, D. O. Brunner, T. Schmid, R. Luechinger, and K. P. Pruessmann, "Prospective motion correction with NMR markers using only native sequence elements," *Magnetic resonance in medicine*, 2017.

[120] M. Zaitsev, C. Dold, G. Sakas, J. Hennig, and O. Speck, "Magnetic resonance imaging of freely moving objects: prospective real-time motion correction using an external optical motion tracking system," *NeuroImage*, vol. 31, no. 3, pp. 1038–1050, 2006.

[121] J. Maclaren, Armstrong, Brian S R, R. T. Barrows, K. A. Danishad, T. Ernst, C. L. Foster, K. Gumus, M. Herbst, I. Y. Kadashevich, T. P. Kusik, Q. Li, C. Lovell-Smith, T. Prieto, P. Schulze, O. Speck, D. Stucht, and M. Zaitsev, "Measurement and correction of microscopic head motion during magnetic resonance imaging of the brain," *PloS one*, vol. 7, no. 11, p. e48088, 2012.

[122] R. Frost, P. Wighton, F. I. Karahanoğlu, R. L. Robertson, P. E. Grant, B. Fischl, M. D. Tisdall, and A. van der Kouwe, "Markerless high-frequency prospective motion correction for neuroanatomical MRI," *Magnetic resonance in medicine*, 2019.

[123] B. Zahneisen, B. Keating, and T. Ernst, "Propagation of calibration errors in prospective motion correction using external tracking," *Magnetic resonance in medicine*, vol. 72, no. 2, pp. 381–388, 2014.

[124] T. P. Trouard, Y. Sabharwal, M. I. Altbach, and A. F. Gmitro, "Analysis and comparison of motion-correction techniques in diffusion-weighted imaging," *Journal of Magnetic Resonance Imaging*, vol. 6, no. 6, pp. 925–935, 1996.

[125] M. Eschelbach, A. Aghaeifar, J. Bause, J. Handwerker, J. Anders, E.-M. Engel, A. Thielscher, and K. Scheffler, "Comparison of prospective head motion correction with NMR field probes and an optical tracking system," *Magnetic resonance in medicine*, 2018.

[126] D. Gallichan, J. P. Marques, and R. Gruetter, "Retrospective correction of involuntary microscopic head movement using highly accelerated fat image navigators (3D FatNavs) at 7T," *Magnetic Resonance in Medicine*, vol. 75, no. 3, pp. 1030–1039, 2016.

[127] C. Federau and D. Gallichan, "Motion-Correction Enabled Ultra-High Resolution In-Vivo 7T-MRI of the Brain," *PloS one*, vol. 11, no. 5, p. e0154974, 2016.

[128] F. Gretsch, H. Mattern, D. Gallichan, and O. Speck, "Fat navigators and Moiré phase tracking comparison for motion estimation and retrospective correction," *Magnetic resonance in medicine*, 2019.

[129] H. Mattern, A. Sciarra, F. Lüsebrink, J. Acosta-Cabronero, and O. Speck, "Prospective motion correction improves high-resolution quantitative susceptibility mapping at 7T," *Magnetic Resonance in Medicine*, vol. 81, no. 3, pp. 1605–1619, 2019.

[130] H. Mattern, J. Acosta-Cabronero, A. Sciarra, and O. Speck, "Prospectively motioncorrected QSM at 7 Tesla," in *ESMRMB 2016, 33rd Annual Scientific Meeting, Vienna, AT, September 29 - October 1: Abstracts, Saturday*, 2016.

[131] H. Mattern, J. Acosta-Cabronero, A. Sciarra, and O. Speck, "Prospective motion correction for high-resolution QSM," in *4th International Workshop on Quantitative Susceptibility Mapping*, 2016.

[132] H. Mattern, J. Acosta-Cabronero, A. Sciarra, and O. Speck, "Prospectively motion corrected QSM-based venograms at 7 Tesla," in *7th Annual Scientific Symposium Ultrahigh Field Magnetic*

*Resonance*, 2016.

[133] J. Acosta-Cabronero, C. Milovic, H. Mattern, C. Tejos, O. Speck, and M. F. Callaghan, "A robust multi-scale approach to quantitative susceptibility mapping," *NeuroImage*, 2018.

[134] C. Milovic, J. Acosta-Cabronero, J. M. Pinto, H. Mattern, M. Andia, S. Uribe, and C. Tejos, "A new discrete dipole kernel for quantitative susceptibility mapping," *Magnetic resonance imaging*, 2018.

[135] C. Milovic, B. Bilgic, B. Zhao, J. Acosta-Cabronero, and C. Tejos, "Fast nonlinear susceptibility inversion with variational regularization," *Magnetic resonance in medicine*, 2018.

[136] B. Avants, C. Epstein, M. Grossman, and J. Gee, "Symmetric diffeomorphic image registration with cross-correlation: Evaluating automated labeling of elderly and neurodegenerative brain," *Medical Image Analysis*, vol. 12, no. 1, pp. 26–41, 2008.

[137] S. M. Smith, "Fast robust automated brain extraction," *Human brain mapping*, vol. 17, no. 3, pp. 143–155, 2002.

[138] W. Li, A. V. Avram, B. Wu, X. Xiao, and C. Liu, "Integrated Laplacian-based phase unwrapping and background phase removal for quantitative susceptibility mapping," *NMR in biomedicine*, vol. 27, no. 2, pp. 219–227, 2014.

[139] T. Liu, C. Wisnieff, M. Lou, W. Chen, P. Spincemaille, and Y. Wang, "Nonlinear formulation of the magnetic field to source relationship for robust quantitative susceptibility mapping," *Magnetic resonance in medicine*, vol. 69, no. 2, pp. 467–476, 2013.

[140] K. J. Friston, *Statistical parametric mapping: The analysis of functional brain images*. London: Academic, 2007.

[141] B. Patenaude, S. M. Smith, D. N. Kennedy, and M. Jenkinson, "A Bayesian model of shape and appearance for subcortical brain segmentation," *NeuroImage*, vol. 56, no. 3, pp. 907–922, 2011.

[142] D.-H. Kwon, J.-M. Kim, S.-H. Oh, H.-J. Jeong, S.-Y. Park, E.-S. Oh, J.-G. Chi, Y.-B. Kim, B. S. Jeon, and Z.-H. Cho, "Seven-Tesla magnetic resonance images of the substantia nigra in Parkinson disease," *Annals of neurology*, vol. 71, no. 2, pp. 267–277, 2012.

[143] J. Acosta-Cabronero, A. Cardenas-Blanco, M. J. Betts, M. Butryn, J. P. Valdes-Herrera, I. Galazky, and P. J. Nestor, "The whole-brain pattern of magnetic susceptibility perturbations in Parkinson's disease," *Brain : a journal of neurology*, vol. 140, no. 1, pp. 118–131, 2017.

[144] U. Yarach, C. Luengviriya, D. Stucht, F. Godenschweger, P. Schulze, and O. Speck, "Correction of B 0-induced geometric distortion variations in prospective motion correction for 7T MRI," *Magma (New York, N.Y.)*, 2016.

[145] P. S. Özbay, Y. Duerst, B. J. Wilm, K. P. Pruessmann, and D. Nanz, "Enhanced quantitative susceptibility mapping (QSM) using real-time field control," *Magnetic resonance in medicine*, 2017.

[146] J. Wen, A. H. Cross, and D. A. Yablonskiy, "On the role of physiological fluctuations in quantitative gradient echo MRI: Implications for GEPCI, QSM, and SWI," *Magnetic resonance in medicine*, vol. 73, no. 1, pp. 195–203, 2015.

[147] N. Todd, O. Josephs, M. F. Callaghan, A. Lutti, and N. Weiskopf, "Prospective motion correction of 3D echo-planar imaging data for functional MRI using optical tracking," *NeuroImage*, vol. 113, pp. 1–12, 2015.

[148] R. Castella, L. Arn, E. Dupuis, M. F. Callaghan, B. Draganski, and A. Lutti, "Controlling motion artefact levels in MR images by suspending data acquisition during periods of head motion," *Magnetic resonance in medicine*, 2018.

[149] H. Mattern, A. Sciarra, F. Godenschweger, D. Stucht, F. Lüsebrink, G. Rose, and O. Speck, "Prospective motion correction enables highest resolution time-of-flight angiography at 7T," *Magnetic resonance in medicine*, vol. 80, no. 1, pp. 248–258, 2018.

[150] H. Mattern, A. Sciarra, F. Godenschweger, D. Stucht, F. Lüsebrink, and O. Speck, "Beyond the biological resolution limit: Prospectively motion corrected Time of Flight angiography at 7T," in *Proc. Intl. Soc. Mag. Reson. Med*, 2017.

[151] H. Mattern, A. Sciarra, F. Godenschweger, D. Stucht, F. Lüsebrink, and O. Speck, "Prospective motion correction for ultra-high resolution Time of Flight angiography at 7T under SAR constraints," in *Proc. Intl. Soc. Mag. Reson. Med*, 2016.

[152] H. Mattern, A. Sciarra, D. Stucht, F. Godenschweger, and O. Speck, "Beyond high resolution: Prospectively motion corrected Time of Flight angiography with 150 µm isotropic resolution at 7T under SAR constraints," in *28rd Annual International Conference of Society of Magnetic Resonance Angiography*, 2016.

[153] H. Mattern, F. Godenschweger, A. Sciarra, D. Stucht, and O. Speck, "Ultra-high resolution Time of Flight angiography at 7T with prospective motion correction under SAR constraints," in *DS-ISMRM2015 - Konferenzband* (DS-ISMRM2015, ed.), 2015.

[154] M. A. Griswold, P. M. Jakob, R. M. Heidemann, M. Nittka, V. Jellus, J. Wang, B. Kiefer, and A. Haase, "Generalized autocalibrating partially parallel acquisitions (GRAPPA)," *Magnetic Resonance in Medicine*, vol. 47, no. 6, pp. 1202–1210, 2002.

[155] M. Aksoy, C. Forman, M. Straka, T. Çukur, J. Hornegger, and R. Bammer, "Hybrid prospective and retrospective head motion correction to mitigate cross-calibration errors," *Magnetic Resonance in Medicine*, vol. 67, no. 5, pp. 1237–1251, 2012.

[156] D. O. Walsh, A. F. Gmitro, and M. W. Marcellin, "Adaptive reconstruction of phased array MR imagery," *Magnetic Resonance in Medicine*, vol. 43, no. 5, pp. 682–690, 2000.

[157] Y. P. Du, D. L. Parker, W. L. Davis, and G. Cao, "Reduction of partial-volume artifacts with zero-filled interpolation in three-dimensional MR angiography," *Journal of Magnetic Resonance Imaging*, vol. 4, no. 5, pp. 733–741, 1994.

[158] J. P. Mugler and J. R. Brookeman, "Three-dimensional magnetization-prepared rapid gradient-echo imaging (3D MP RAGE)," *Magnetic Resonance in Medicine*, vol. 15, no. 1, pp. 152–157, 1990.

[159] M. Jenkinson, C. F. Beckmann, T. E. J. Behrens, M. W. Woolrich, and S. M. Smith, "FSL," *NeuroImage*, vol. 62, no. 2, pp. 782–790, 2012.

[160] S. N. Wright, P. Kochunov, F. Mut, M. Bergamino, K. M. Brown, J. C. Mazziotta, A. W. Toga, J. R. Cebral, and G. A. Ascoli, "Digital reconstruction and morphometric analysis of human brain arterial vasculature from magnetic resonance angiography," *NeuroImage*, vol. 82, pp. 170–181, 2013.

[161] S. W. Seo, C.-K. Kang, S. H. Kim, D. S. Yoon, W. Liao, S. Wörz, K. Rohr, Y.-B. Kim, D. L. Na, and Z.-H. Cho, "Measurements of lenticulostriate arteries using 7T MRI: new imaging markers for subcortical vascular dementia," *Journal of the neurological sciences*, vol. 322, no. 1-2, pp. 200–205, 2012.

[162] V. W. Fischer, A. Siddiqi, and Y. Yusufaly, "Altered angioarchitecture in selected areas of brains with Alzheimer's disease," *Acta Neuropathologica*, vol. 79, no. 6, pp. 672–679, 1990.

[163] Z.-H. Cho, C.-K. Kang, J.-Y. Han, S.-H. Kim, C.-A. Park, K.-N. Kim, S.-M. Hong, C.-W. Park, and Y.-B. Kim, "Functional MR angiography with 7.0 T Is direct observation of arterial response

during neural activity possible?," *NeuroImage*, vol. 42, no. 1, pp. 70–75, 2008.

[164] C.-A. Park, C.-K. Kang, Y.-B. Kim, and Z.-H. Cho, "Examining the resting-state vascular connectivity using fMRA in comparison with fMRI: a preliminary study," *Neuroreport*, vol. 26, no. 11, pp. 623–628, 2015.

[165] M. Lustig, D. Donoho, and J. M. Pauly, "Sparse MRI: The application of compressed sensing for rapid MR imaging," *Magnetic resonance in medicine*, vol. 58, no. 6, pp. 1182–1195, 2007.

[166] K. Setsompop, D. A. Feinberg, and J. R. Polimeni, "Rapid brain MRI acquisition techniques at ultra-high fields," *NMR in biomedicine*, vol. 29, no. 9, pp. 1198–1221, 2016.

[167] J. Schulz, R. Boyacioğlu, and D. G. Norris, "Multiband multislab 3D time-of-flight magnetic resonance angiography for reduced acquisition time and improved sensitivity," *Magnetic Resonance in Medicine*, vol. 75, no. 4, pp. 1662–1668, 2016.

[168] T. Yamamoto, T. Okada, Y. Fushimi, A. Yamamoto, K. Fujimoto, S. Okuchi, H. Fukutomi, J. C. Takahashi, T. Funaki, S. Miyamoto, A. F. Stalder, Y. Natsuaki, P. Speier, and K. Togashi, "Magnetic resonance angiography with compressed sensing: An evaluation of moyamoya disease," *PloS one*, vol. 13, no. 1, p. e0189493, 2018.

[169] M. Kayvanrad, A. Lin, R. Joshi, J. Chiu, and T. Peters, "Diagnostic quality assessment of compressed sensing accelerated magnetic resonance neuroimaging," *Journal of magnetic resonance imaging : JMRI*, vol. 44, no. 2, pp. 433–444, 2016.

[170] C.-A. Park, D. Kang, Y.-D. Son, H.-K. Kim, and C.-K. Kang, "Microvascular Imaging Using Compressed Sensing at 7T MRI: A Preliminary Study," *Applied Magnetic Resonance*, vol. 46, no. 11, pp. 1189–1197, 2015.

[171] J. Milles, M. J. Versluis, A. G. Webb, and J. H. Reiber, "Quantitative evaluation of Compressed Sensing in MRI: Application to 7T time-of-flight angiography," in *10th IEEE International Conference on Information Technology and Applications in Biomedicine (ITAB), 2010*, (Piscataway, NJ), pp. 1–4, IEEE, 2010.

[172] H. Mattern and O. Speck, "Optimizing Cartesian compressed sensing for ultra-high resolution Time of Flight angiography," in *Proc. Intl. Soc. Mag. Reson. Med*, 2018.

[173] U. Yarach, C. Luengviriya, A. Danishad, D. Stucht, F. Godenschweger, P. Schulze, and O. Speck, "Correction of gradient nonlinearity artifacts in prospective motion correction for 7T MRI," *Magnetic resonance in medicine : official journal of the Society of Magnetic Resonance in Medicine / Society of Magnetic Resonance in Medicine*, vol. 73, no. 4, pp. 1562–1569, 2015.

[174] M. Soellinger, A. K. Rutz, S. Kozerke, and P. Boesiger, "3D cine displacement-encoded MRI of pulsatile brain motion," *Magnetic resonance in medicine*, vol. 61, no. 1, pp. 153–162, 2009.

[175] S. Schmitter, X. Wu, G. Adriany, E. J. Auerbach, K. Uğurbil, and P.-F. Moortele, "Cerebral TOF angiography at 7T: Impact of B1 (+) shimming with a 16-channel transceiver array," *Magnetic resonance in medicine*, vol. 71, no. 3, pp. 966–977, 2014.

[176] L. Pierot, C. Portefaix, C. Rodriguez-Regent, S. Gallas, J.-F. Meder, and C. Oppenheim, "Role of MRA in the detection of intracranial aneurysm in the acute phase of subarachnoid hemorrhage," *Journal of neuroradiology. Journal de neuroradiologie*, vol. 40, no. 3, pp. 204–210, 2013.

[177] J. Budde, G. Shajan, K. Scheffler, and R. Pohmann, "Ultra-high resolution imaging of the human brain using acquisition-weighted imaging at 9.4T," *NeuroImage*, vol. 86, pp. 592–598, 2014.

[178] J. Liu, J. A. de Zwart, P. van Gelderen, J. Murphy-Boesch, and J. H. Duyn, "Effect of head motion on MRI B0 field distribution," *Magnetic resonance in medicine*, 2018.

[179] Y. Duerst, B. J. Wilm, M. Wyss, B. E. Dietrich, S. Gross, T. Schmid, D. O. Brunner, and K. P.

Pruessmann, "Utility of real-time field control in T2 *-Weighted head MRI at 7T," *Magnetic resonance in medicine*, vol. 76, no. 2, pp. 430–439, 2016.

[180] Y. Chen, S. Liu, S. Buch, J. Hu, Y. Kang, and E. M. Haacke, "An interleaved sequence for simultaneous magnetic resonance angiography (MRA), susceptibility weighted imaging (SWI) and quantitative susceptibility mapping (QSM)," *Magnetic resonance imaging*, vol. 47, pp. 1–6, 2017.

[181] D. Wu, S. Liu, S. Buch, Y. Ye, Y. Dai, and E. M. Haacke, "A fully flow-compensated multiecho susceptibility-weighted imaging sequence: The effects of acceleration and background field on flow compensation," *Magnetic resonance in medicine*, vol. 76, no. 2, pp. 478–489, 2016.

[182] K. T. Bae, S.-H. Park, C.-H. Moon, J.-H. Kim, D. Kaya, and T. Zhao, "Dual-echo arteriovenography imaging with 7T MRI," *Journal of Magnetic Resonance Imaging*, vol. 31, no. 1, pp. 255–261, 2010.

[183] Y. P. Du and Z. Jin, "Simultaneous acquisition of MR angiography and venography (MRAV)," *Magnetic resonance in medicine*, vol. 59, no. 5, pp. 954–958, 2008.

[184] A. J. Trotier, W. Lefrançois, E. J. Ribot, E. Thiaudiere, J.-M. Franconi, and S. Miraux, "Time-resolved TOF MR angiography in mice using a prospective 3D radial double golden angle approach," *Magnetic resonance in medicine : official journal of the Society of Magnetic Resonance in Medicine / Society of Magnetic Resonance in Medicine*, vol. 73, no. 3, pp. 984–994, 2015.

[185] C.-K. Kang, C.-A. Park, D. S. Lee, Y.-B. Lee, C.-W. Park, Y.-B. Kim, and Z.-H. Cho, "Velocity measurement of microvessels using phase-contrast magnetic resonance angiography at 7 tesla MRI," *Magnetic Resonance in Medicine*, vol. 75, no. 4, pp. 1640–1646, 2016.

[186] M. Obara, O. Togao, M. Yoneyama, T. Okuaki, S. Shibukawa, H. Honda, and M. van Cauteren, "Acceleration-selective arterial spin labeling for intracranial MR angiography with improved visualization of cortical arteries and suppression of cortical veins," *Magnetic resonance in medicine*, vol. 77, no. 5, pp. 1996–2004, 2017.

[187] M. Obara, O. Togao, G. M. Beck, S. Shibukawa, T. Okuaki, M. Yoneyama, M. Nakamura, H. Honda, and M. van Cauteren, "Non-contrast enhanced 4D intracranial MR angiography based on pseudo-continuous arterial spin labeling with the keyhole and view-sharing technique," *Magnetic resonance in medicine*, 2018.

[188] Y. Suzuki, N. Fujima, T. Ogino, J. A. Meakin, A. Suwa, H. Sugimori, M. van Cauteren, and M. J. P. van Osch, "Acceleration of ASL-based time-resolved MR angiography by acquisition of control and labeled images in the same shot (ACTRESS)," *Magnetic resonance in medicine*, 2017.

[189] Z. Zhou, F. Han, S. Yu, D. Yu, S. Rapacchi, H. K. Song, D. J. J. Wang, P. Hu, and L. Yan, "Accelerated noncontrast-enhanced 4-dimensional intracranial MR angiography using golden-angle stack-of-stars trajectory and compressed sensing with magnitude subtraction," *Magnetic resonance in medicine*, vol. 79, no. 2, pp. 867–878, 2018.

[190] W. K. El-Bouri and S. J. Payne, "Investigating the effects of a penetrating vessel occlusion with a multi-scale microvasculature model of the human cerebral cortex," *NeuroImage*, vol. 172, pp. 94–106, 2018.

[191] Y. Tian, F. Duan, K. Lu, M. Zhou, Z. Wu, Q. Wang, L. Sun, and L. Xie, "A flexible 3D cerebrovascular extraction from TOF-MRA images," *Neurocomputing*, vol. 121, pp. 392–400, 2013.

[192] L. Chen, M. Mossa-Basha, N. Balu, G. Canton, J. Sun, K. Pimentel, T. S. Hatsukami, J.-N. Hwang, and C. Yuan, "Development of a quantitative intracranial vascular features extraction tool on 3D MRA using semiautomated open-curve active contour vessel tracing," *Magnetic resonance in medicine*, 2017.

[193] C.-Y. Hsu, M. Ghaffari, A. Alaraj, M. Flannery, X. J. Zhou, and A. Linninger, "Gap-free segmentation of vascular networks with automatic image processing pipeline," *Computers in biology and medicine*, vol. 82, pp. 29–39, 2017.

[194] S. Almasi, A. Lauric, A. Malek, and E. L. Miller, "Cerebrovascular Network Registration via An Efficient Attributed Graph Matching Technique," *Medical Image Analysis*, 2018.

[195] P. G. D. Ward, N. J. Ferris, P. Raniga, D. L. Dowe, A. C. L. Ng, D. G. Barnes, and G. F. Egan, "Combining images and anatomical knowledge to improve automated vein segmentation in MRI," *NeuroImage*, vol. 165, pp. 294–305, 2018.

[196] M. Bernier, S. C. Cunnane, and K. Whittingstall, "The morphology of the human cerebrovascular system," *Human brain mapping*, 2018.

[197] J. Huck, Y. Wanner, A. P. Fan, A.-T. Schmidt, S. Grahl, U. Schneider, A. Villringer, C. J. Steele, C. L. Tardif, P.-L. Bazin, and C. J. Gauthier, "High resolution atlasing of the venous brain vasculature from 7T quantitative susceptibility," *bioRxiv*, 2018.

[198] H. Mattern, J. Acosta-Cabronero, and O. Speck, "High resolution imaging of the arterial and venous vasculature in deep gray matter," in *Proc. Intl. Soc. Mag. Reson. Med*, 2019.

[199] K. Kisler, A. R. Nelson, A. Montagne, and B. V. Zlokovic, "Cerebral blood flow regulation and neurovascular dysfunction in Alzheimer disease," *Nature reviews. Neuroscience*, vol. 18, no. 7, pp. 419–434, 2017.

[200] H. Mattern, F. Lüsebrink, and O. Speck, "Ultrahochaufgelöste MRT des Gehirns mittels prospektiver Bewegungskorrektur," in *Neurorad 2017*, 2017.

[201] F. Lüsebrink, H. Mattern, and O. Speck, "Beyond high resolution: A glimpse into the future," in *Brain in Depth Symposium 2018*, 2018.

[202] B. A. Hargreaves, C. H. Cunningham, D. G. Nishimura, and S. M. Conolly, "Variable-rate selective excitation for rapid MRI sequences," *Magnetic resonance in medicine : official journal of the Society of Magnetic Resonance in Medicine / Society of Magnetic Resonance in Medicine*, vol. 52, no. 3, pp. 590–597, 2004.

[203] M. Blaimer, F. Breuer, M. Mueller, R. M. Heidemann, M. A. Griswold, and P. M. Jakob, "SMASH, SENSE, PILS, GRAPPA: How to choose the optimal method," *Topics in magnetic resonance imaging : TMRI*, vol. 15, no. 4, pp. 223–236, 2004.

[204] A. Deshmane, V. Gulani, M. A. Griswold, and N. Seiberlich, "Parallel MR imaging," *Journal of magnetic resonance imaging : JMRI*, vol. 36, no. 1, pp. 55–72, 2012.

[205] B. Wu, W. Li, A. Guidon, and C. Liu, "Whole brain susceptibility mapping using compressed sensing," *Magnetic resonance in medicine*, vol. 67, no. 1, pp. 137–147, 2012.